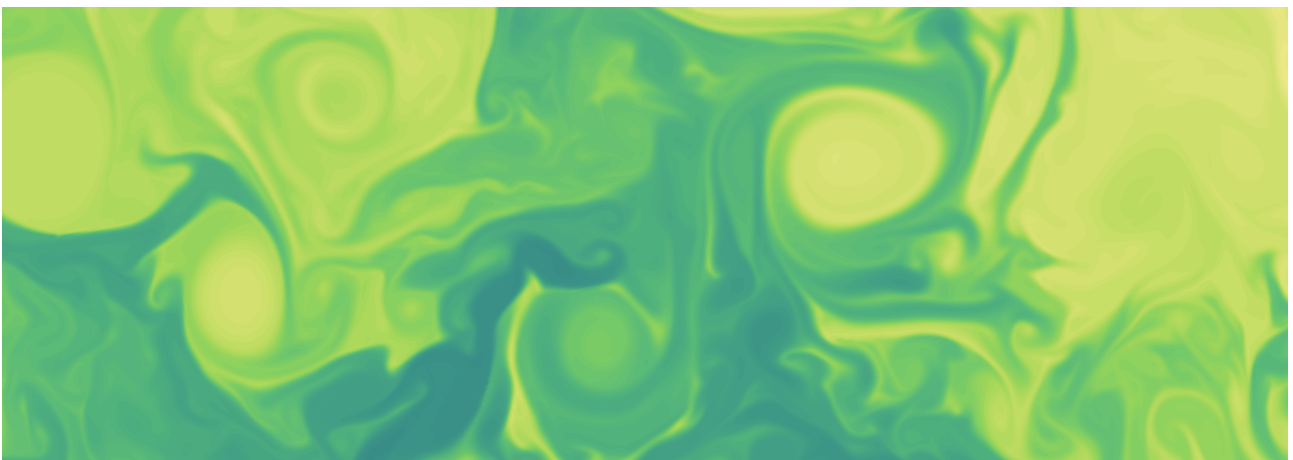# Characteristics of Mesoscale and Submesoscale Eddies in the Labrador Sea: Observations vs. Model

Master thesis

in the program **(M.Sc.) Climate Physics: Meteorology and Physical Oceanography**

Christian-Albrechts-University, Kiel

Faculty of Mathematics and Natural Sciences

GEOMAR Helmholtz Centre for Ocean Research Kiel

Arne Bendinger

Matriculation number: 1012126

Supervisor: Dr. Johannes Karstensen

Second assessor: Prof. Dr. Arne Biastoch

March 13, 2020

Contents

Abstract

Mesoscale eddies play an important role in lateral property fluxes. Observational studies often use sea level anomaly maps from satellite altimetry to estimate eddy statistics (incl. eddy kinetic energy). Recent findings suggest that altimetry derived eddy characteristics may suffer from the low spatial resolution of past and current satellite-tracks in high-latitude oceans associated with small Rossby radii. This study presents results of an eddy reconstruction that provides an alternative perspective on the eddy field based on a nonlinear, damping Gauss-Newton optimisation algorithm using ship-based current profiler observations from two research expeditions in the Labrador Sea in 2014 and 2018. The derived eddy characteristics are compared to the high-resolution submesoscale permitting NATL60 model (1/60°).

Overall, a total of 14 eddies with radii ranging from 7 to 35 km and azimuthal velocities ranging from 20 to 60 cm s^{-1} were detected, of which 3 eddies were identified as Irminger rings. Irminger rings are characterised by a warm, salty lens either surface trapped or overlaid by a cold, fresh cap of water. The modelled eddies are on average 25 % smaller in radius and 20 % higher in azimuthal velocity accompanied by increased nonlinearity. The inner ring velocity structure for observations and NATL60 suggests solid-body rotation for 1/2 to 2/3 of the radius. The eddy boundary and outer ring velocity structure follows a more Gaussian-like shape, best described by a $\exp(-r^2)$ dependency. Furthermore, the maximum azimuthal velocity may deviate from solid-body rotation by more than 30 % for the observations and 50 % for the model.

In order to verify the skill of eddy reconstruction, the NATL60 served as a reference data set for the skill assessment of the Gauss-Newton method. It is shown that the eddy characteristics are affected by the location of the ship track through the velocity field. In most cases, however, the derived properties are not expected to deviate by more than 10 %.

Spectral analysis of the horizontal velocity implies that the mesoscale regime is well represented in NATL60 compared with the observations. The representation of the submesoscale flow decreases in the model with increasing depth. In particular, observations and model spectra diverge in the pycnocline by roughly one order of magnitude at scales smaller than 50 km. Besides, the transition of power spectra slopes from k^{-2} to k^{-3} in ship-based measurements and model suggests a weak seasonal signal.

Zusammenfassung

Mesoskalige Wirbel spielen eine wichtige Rolle bei den lateralen Eigenschaftsflüssen. In Beobachtungsstudien werden häufig Meeresspiegelanomalienkarten aus der Satelliten-höhenmessung zur Abschätzung der Wirbelstatistik (inkl. der kinetischen Wirbelenergie) verwendet. Jüngste Erkenntnisse deuten darauf hin, dass die von der Altimetrie abgeleiteten Wirbelcharakteristika unter der geringen räumlichen Auflösung von vergangenen und aktuellen Satellitendaten in Ozeanen in hohen Breitengraden in Verbindung mit kleinen Rossby-Radien leiden könnten. Diese Studie stellt die Ergebnisse einer Wirbel-rekonstruktion vor, die eine alternative Perspektive auf das Wirbelfeld auf der Grundlage eines nichtlinearen Dämpfungsalgorithmus zur Gauß-Newton Optimierung bietet, wobei schiffsbasierte Beobachtungen von Strömungsprofilen aus zwei Forschungsexpeditionen in der Labradorsee in den Jahren 2014 und 2018 verwendet werden. Die abgeleiteten Wirbelcharakteristika werden mit dem hochauflösenden submesoskaligen NATL60 Modell (1/60°) verglichen.

Insgesamt wurden 14 Wirbel mit Radien von 7 bis 35 km und azimutalen Geschwindig-keiten im Bereich von 20 bis 60 cm s^{-1} erfasst, von denen 3 Wirbel als Irminger Ringe identifiziert wurden. Irminger Ringe zeichnen sich durch eine warme, salzhaltige Linse aus, die entweder an der Oberfläche eingeschlossen oder überlagert von einer kalten, frischen Wasserschicht sind. Die modellierten Wirbel sind im Durchschnitt 25 % kleiner im Radius und 20 % höher in der azimutalen Geschwindigkeit, begleitet von erhöhter Nichtlinearität. Die innere Ringgeschwindigkeitsstruktur für Beobachtungen und Model schlägt eine Festkörperrotation für 1/2 bis 2/3 des Radius vor. Die Wirbelgrenze und die Struktur der äußeren Ringgeschwindigkeit folgt einer eher Gauß-ähnlichen Form, die am besten durch eine $\exp(-r^2)$ Abhängigkeit beschrieben werden kann. Darüber hinaus kann die maximale azimutale Geschwindigkeit von Festkörperrotation um mehr als 30 % für die Beobachtungen und 50 % für das Modell abweichen. Um die Fähigkeit der Wirbelrekonstruktion zu verifizieren, diente das NATL60 als Referenzdatensatz für die Fehlerabschätzung der Gauß-Newton Methode. Es wird gezeigt, dass die Wirbelcharak-teristik durch die Lage des Schiffkurses durch das Geschwindigkeitsfeld beeinflusst wird. In den meisten Fällen wird jedoch erwartet, dass die abgeleiteten Eigenschaften sich nicht um mehr als 10 % unterscheiden.

Die Spektralanalyse der horizontalen Geschwindigkeit impliziert, dass das mesoskalige Regime im Vergleich mit den Beobachtungen gut in NATL60 vertreten ist. Die Repräsen-tierung der submesoskaligen Prozesse nimmt im Modell mit zunehmender Tiefe ab. Insbesondere in der Pycnocline divergieren die Beobachtungs- und Modellspektren um etwa eine Größenordnung bei Skalen kleiner als 50 km auseinander. Außerdem deutet der Übergang der Spektraldichtensteigungen von k^{-2} auf k^{-3} bei schiffsbasierten Messungen und Modell auf ein schwaches saisonales Signal hin.

1 Introduction

1.1 Oceanic coherent vortices

The large-scale ocean circulation is a result of nonlinear scale interactions and energy exchanged among all scales of motion. In particular, energy is transferred from planetary scales to microscales as illustrated by the oceanic energy cascade in **Figure 1**. External forces drive the large-scale ocean circulation. These forces are heat, freshwater, and momentum fluxes with large-scale wind forcing the most dominant energy source setting up density gradients which in turn drive geostrophic motion. Thus, wind forcing represents a reservoir of available potential energy which is directly transferred to kinetic energy. In order to achieve a climate equilibrium, energy from the large-scale forcing is redistributed across all spatial and temporal scales. This oceanic kinetic energy is largely dominated by the mesoscale eddy field on scales in the order of $\mathcal{O}(10\text{--}100\,\text{km})$ and accounts for over $90\,\%$ of the kinetic energy of the flow (Wyrtki et al., 1976; Chelton et al., 1998; Wunsch and Ferrari, 2004).

In a standard Eulerian statistical perspective the term eddy is understood as a fluctuation about an Eulerian temporal or spatial mean state. In oceanography, it is related to coherent mesoscale features. These coherent structures are associated with large-scale vortices that conserve the temporal and spatial features during their life cycle. In other words, coherent structures are large-scale, self-defined features that retain some element of coherence for relatively long periods such that they can be traced at great

Figure 1: Schematic adapted from McWilliams (2016) visualising the oceanic forward energy cascade from planetary-scale forcing to microscale dissipation and mixing. The submesoscale regime represents the margin between the rotational and balanced, and the non-rotational and unbalanced regime.

distances from their initialisation region (Yule, 1978; Chigier, 1979). Here, eddies are hence referred to as a coherent distribution of vorticity and are characterised by either clockwise (anticyclonic) or anticlockwise (cyclonic) rotation about vertical axes. They may be restricted to the near-surface or extend throughout the water column and feature swirl velocities considerably larger than the mean flow (Robinson, 1983).

In general, mesoscale variability can occur as linear Rossby waves or nonlinear eddies. Mesoscale variability as observed by satellite altimetry measurements used to be interpreted as linear Rossby waves (Chelton and Schlax, 1996). However, higher resolution sea level anomaly fields (Ducet et al., 2000; Le Traon et al., 2003) revealed that the major contribution to mesoscale variability is subject to nonlinear eddies (Chelton et al., 2007, 2011).

Nonlinearity, as defined by quasigeostrophy theory, refers to the ratio between relative vorticity advection and planetary vorticity advection that exceeds unity. Moreover, nonlinear eddies are characterised by rotational speeds that are larger than their translational speed and clearly distinguish them from linear waves. Characterised by their coherent feature, eddies have been shown to trap fluid in their interior from the initialisation location across ocean basin while contributing to the redistribution of heat, momentum, and mass (Early et al., 2011). It is suggested that the mesoscale eddy field has its origin in baroclinic instabilities of the mean currents, i.e. the large-scale potential energy is transferred to eddy kinetic energy through baroclinic instabilities induced by the vertical shear of the horizontal velocity field. The horizontal length scale of these eddies is in theory set by the baroclinic Rossby radius of deformation $L_D = (NH)/f_0$, where N is the Brunt-Väisälä frequency, H is the vertical length scale, and f_0 is the Coriolis parameter. It describes the horizontal length scale at which rotation effects are as important as buoyancy/stratification effects or at which relative vorticity and vortex stretching equally contribute to potential vorticity. Therefore, rotation-dominated flow is characterised by typical length scales that are larger than L_D ($L/L_D > 1$), whereas stratification-dominated flow is characterised by typical length scales that are smaller than L_D ($L/L_D < 1$) (Gill, 1982; Klocker et al., 2016). Even though there are zonal differences, the deformation radius mainly depends on the latitude and decreases with increasing latitude (Stammer, 1997). The first baroclinic Rossby radius is higher than $200\,\mathrm{km}$ in tropical to subtropical regions and well below $10\,\mathrm{km}$ in subpolar and polar oceans with slightly zonal variations due to local stratification (Chelton et al., 1998; Nurser and Bacon, 2014).

1.2 Mesoscale eddies in the Labrador Sea

The focus of this study is on the eddy field characterisation in the Labrador Sea. The Labrador Sea is one of the few places in the world that is characterised by regularly occurring dense water formation through open-ocean convection that can locally reach

depths of up to 2000 m (Lazier, 1973, 1980; Clarke and Gascard, 1983). Deep convection is confined to specific regions in which doming of isopycnal surfaces from the cyclonic gyre in addition to intense air-sea heat fluxes during winter months favour the buoyancy loss of near-surface waters. The buoyancy loss mainly occurs in so-called convective plumes which in turn form a deep mixed patch with up to 100 km diameter and homogenise the water column (Jones and Marshall, 1993; Lilly et al., 1999; Marshall and Schott, 1999; Pickart et al., 2002). In recent years, the role of eddies in the Labrador Sea has increased in attention and importance as their spatial and temporal occurrence and variability largely influences the location, extent and strength of winter deep convection as well as the restratification of the homogenised water column after wintertime convection (Gascard and Clarke, 1983; Jones and Marshall, 1997; Marshall and Schott, 1999; Chanut et al., 2008; Rieck et al., 2019).

Three types of eddies are known to exist in the Labrador Sea: Irminger Rings (IR), Convective Eddies (CE), and Boundary Current Eddies (BC). IR have their origin on
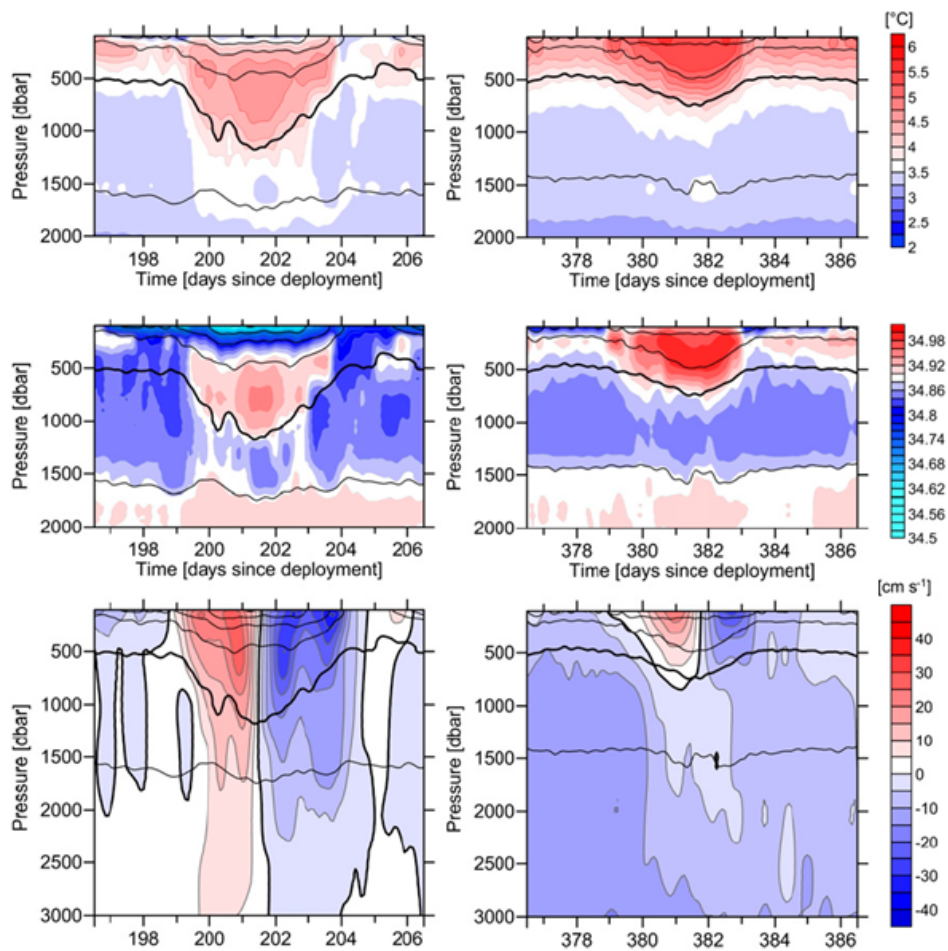

Figure 2: Mooring potential temperature (upper panels), salinity (middle panels), and cross velocity (lower panels) for two exemplary passing Irminger rings adapted from de Jong et al. (2014). Isopycnals (black lines) are drawn every 0.05 kg m^{-3}. The 27.7 kg m^{-3} isopycnal is indicated by the thick black line.

the West Greenland shelf off Cape Desolation (Brandt et al., 2004) and are thought to form either trough barotropic (Eden and Böning, 2002; Chanut et al., 2008) or baroclinic instabilities (Katsman et al., 2004) of the West Greenland Current (WGC) and Irminger Current density field. Besides, wind curl variability on seasonal scales was also considered to drive a barotropic response of the WGC (Greatbatch and Goulding, 1989).

Observation-based studies of IR (Lilly et al., 2003; de Jong et al., 2014) found numerous cases of anticyclonically rotating warm, salty lenses that are either surface trapped or overlaid by a fresh, cold cap of water with surface intensified currents. The reconstruction of the hydrography and velocity field is shown for both types in **Figure 2**. Lilly et al. (2003) detected 12 IR with radii and swirl velocities in the range 11–32 km and 30–77 cm s^{-1} respectively. Evidence for a secondary core of warm, salty water with intensified currents in more than 1000 m depth exists even though it is associated with a considerable degree of uncertainty due to the low spatial resolution of instrument spacing and badly resolved density field. de Jong et al. (2014) also observed 12 IR which feature potential temperatures of 4.7 to 6.6 °C and salinities of 34.94 to 35 psu subject to seasonal fluctuations. The radii are similar to those observed in Lilly et al. (2003) (11–35 cm s^{-1}) but the velocities are overall lower in magnitude (14–50 cm s^{-1}). In contrast to Lilly et al. (2003), the double core structure is not a common feature in de Jong et al. (2014). Both studies emphasise the importance of lateral transport of heat and freshwater fluxes from the boundary current to the central Labrador Sea in preconditioning the upper water column in the central Labrador Sea. Ultimately, the advection of highly stratified waters originating in the Irminger Current may determine both the strength and extent of wintertime convection (Eden and Böning, 2002; Chanut et al., 2008; Rieck et al., 2019).

In contrast to IR, CE do not originate from the boundary currents. Instead, they are formed by baroclinic instability of the large buoyancy gradients in the central Labrador Sea, i.e. along the rim currents of the large-scale convective patch. Thus, they are thought to be responsible for the lateral exchange of convected water and the quick restratification of the homogenised water column after wintertime convection (Gascard and Clarke, 1983; Jones and Marshall, 1997; Marshall and Schott, 1999; Rieck et al., 2019). A total of 13 CE were recorded by the mooring time series in Lilly et al. (2003). Similar to the IR, they feature an anticlockwise sense of rotation. Radii and swirl velocities were measured in the range 5–18 km and 9–32 cm s^{-1}. Even though length scale estimates are not available for all detected eddies, IR seem to be larger in size and have larger swirl velocities. Contrarily, CE are characterised by cold, fresh mid-depth cores with mid-depth intensified currents. A noticeable feature in Lilly et al. (2003) is the existence of CE with vertically-aligned cores which are speculated to consist of a
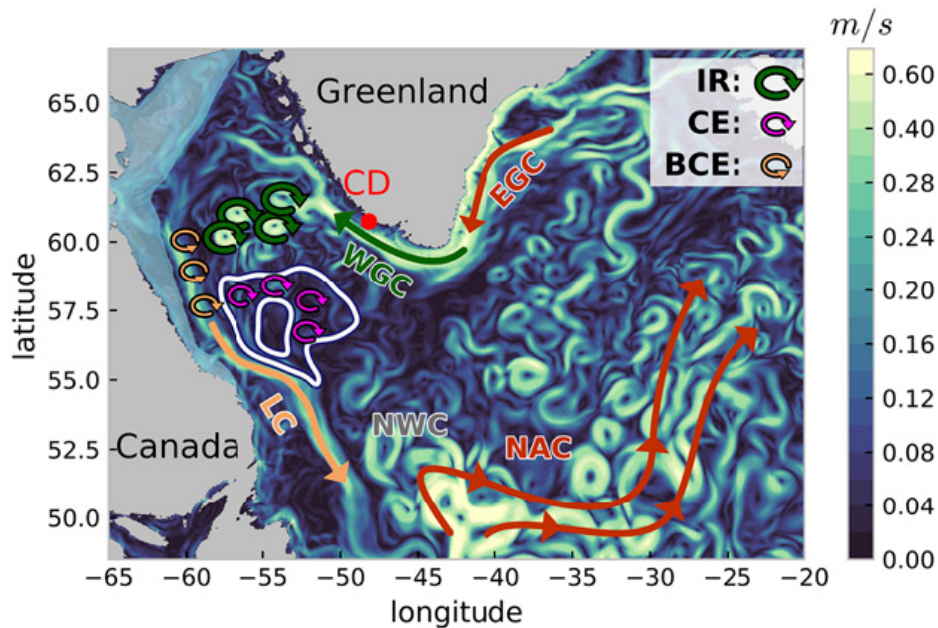
Figure 3: Schematic adapted from Rieck et al. (2019) showing the general near-surface circulation including the West Greenland Current (WGC) and the Labrador Current (LC). Circular arrows represent the areas of natural occurence of Irminger rings (large green circular arrows), convective eddies (small pink circular arrows, and boundary current eddies (small orange circular arrows). In addition, contours of the 750 m and 1200 m 2000-2009 mean March mixed layer depth in the Labrador Sea are plotted (white lines). Shading represents the horizontal current speed at 94 m depth.

shallow and deep lens and contain convected water from the most recent and previous convection process, respectively.

The third type of eddies occurring in the Labrador Sea are BC. They are found along the boundary currents WGC and Labrador Current (LC) and are formed through baroclinic instabilities (Chanut et al., 2008). Even though they usually do not propagate far from the boundary currents, it is argued that play a role in the restratification process after convection by extracting heat from the boundary currents and advecting it towards the convection sites (Gelderloos et al., 2011).

Typical formation and occurrence sites from IR, CE, and BC are summarised in **Figure 3**. The large-scale circulation inclusive of the WGC and LC that surround the Labrador Sea along a cyclonic path from the southern tip of Greenland to the southern exit of the Labrador Sea as well as the mean location of the convection site are also shown.

1.3 Eddy field characterisation through altimetry

Observational platforms such as hydrographic surveys, moorings, floats, and gliders have provided data with high temporal and spatial resolution and were used for the characterisation of eddies in the Labrador Sea (e.g. Lilly et al., 1999, 2003; Hátún et al.,

2007; de Jong et al., 2014). Despite the high sampling rate, they represent in some cases only a synoptical view of the mesoscale flow regime. Another possibility to study the mesoscale eddy field and the corresponding spatial variability of kinetic energy lies in the usage of satellite altimetry products that have the advantage of global coverage and uninterrupted time series compared to the ship-based and field measurements. These altimetry products have been extensively used for more than two decades for studies investigating the characteristics of mesoscale variability and nonlinear eddies in the global ocean (e.g Chelton and Schlax, 1996; Chelton et al., 2007, 2011). The majority of these studies make use of gridded sea level anomaly maps that are derived by gridding and optimal interpolation using an objective analysis of available along-track sea level anomaly data. Accounting for inter alia geophysical corrections, smoothing, and latitude dependent spatial and temporal correlation scales, the along-track data is interpolated on a 2-dimensional grid with a global cartesian resolution of $1/4° \times 1/4°$ on a daily basis (Pujol et al., 2016). The mapping procedure, however, suffers from the compromise between the eddy field characteristics that are desired to be resolved and the available sampling capabilities. Particularly, the distance between two satellite tracks is often larger than the local Rossby radius with consequences for the mesoscale flow regime representation in higher latitudes.

Eddy tracking algorithms applied to the gridded altimetry products rely on the signature of sea level anomaly and especially on the sea level anomaly derived variables. Eddy tracking algorithms are usually associated with two major uncertainties considering the sea level anomaly data. First, how does the relatively coarse satellite resolution resolve the sea level anomaly field? Second, how do eddies express themselves in spatially and temporally varying sea level anomaly field? Generally, in the northern hemisphere, cyclonically (anticyclonically) rotating eddies are characterised by a positive (negative) sea level anomaly. The mesoscale eddy field is not the only component that contributes to sea level anomaly variability. Other effects such as expansion and contraction induced by heating and cooling events in the surface ocean do play a role as well (Chelton et al., 2011). Therefore, it is a common approach to introduce dynamical parameters such as the Okubo-Weiss parameter (Okubo, 1970; Weiss, 1991). The Okubo-Weiss parameter is hence applied to the sea level anomaly data to separate vorticity dominated regions from strain dominated regions to identify eddies in the rotation dominated regions (Isern-Fontanet et al., 2003). Moreover, quality threshold values are implemented that account for minimum size and lifespan. Nonetheless, strict thresholds have increasingly become unfavourable since they do not only filter spurious but also real features (Faghmous et al., 2015). More recent eddy tracking algorithms define eddies as a single extremum whose sea level anomaly is greater or smaller than its 24 neighbours (5×5 grid cells) and is surrounded by an enclosed sea level anomaly contour (Faghmous et al., 2015).

A recent study from Amores et al. (2018) questioned the ability to track eddies using gridded maps of sea level anomaly in a wider framework. The authors investigated whether altimetry data sets are able to resolve the horizontal eddy scales in the North Atlantic and the Mediterranean Sea using a high-resolution model (1/60°) as reference. The eddy tracking algorithm from Faghmous et al. (2015) was applied to four different sea level anomaly products: the high-resolution model sea level anomaly, the high-resolution sea level anomaly resampled to the gridded satellite resolution, optimally interpolated and gridded synthetic satellite tracks extracted from the high-resolution model sea level anomaly, and the observational gridded sea level anomaly obtained from CMES (Copernicus Marine and Environment Monitoring Service). It was found that only 6 % (16 %) of the total eddies in the North Atlantic (Mediterranean Sea) are captured by the satellite-like products. On top of that, median values for eddy radius and amplitude are up 7-8 times (2-3 times) lower than the low-resolution products accompanied by higher values for eddy density in the North Atlantic (Mediterranean Sea). It can be concluded that the satellite-like products largely overestimate the horizontal eddy length scale and strength. The main reason is the spatial resolution of the gridded products (1/4° and 1/8°, respectively). Particularly, the across-track satellite distance is larger than the Rossby deformation radius failing to resolve smaller-scale structures. As a direct consequence, the altimetry data suffers from aliasing introducing an artificial eddy field representation such that the gridding algorithm may merge several small-scale eddies into a larger one. Summarised, the characterisation of the eddy field using altimetry products as well as the eddy tracking algorithm associated uncertainties most likely lead to a distortion of the real eddy field and need to be used with caution.

A future satellite mission aims to solve the aliasing of the badly resolved eddy field. The Surface Water Ocean Topography (SWOT) altimeter mission planned for launch in 2021 will revolutionise the way the ocean is observed by resolving the mesoscale and submesoscale circulation at scales up to 15 km. SWOT represents the transition from profile to swath altimetry and features a swath width of 120 km with a 20 km nadir gap (Fu et al., 2012; Fu and Ubelmann, 2014; Morrow et al., 2019). Of particular interest is the observation of the submesoscale flow regime which is introduced in the following.

1.4 Submesoscale flow regime

For decades the processes and dynamics of the submesoscale flow have not been know or understood, partly owed to the lack of high-resolution observations and models. First observations of spatial scales smaller than the highly energetic mesoscale flow in the Labrador Sea are provided by McWilliams (1985) who detected submesoscale eddies with coherent properties (therefore called submesoscale coherent vortices). These

coherent vortices featured mid-depth cores of negative anomalies in temperature and salinity, have scales smaller than the first baroclinic Rossby radius and are thus highly related to the convective eddies found by Lilly et al. (2003).

In contrast to the mesoscale, the submesoscale flow regime is found on spatial scales in the order of $\mathcal{O}(0.1\text{--}10\,\text{km})$ (McWilliams, 2016). It is only since the new millennium when the submesoscale regime received more attention due to the progress of submesocale permitting or resolving numerical modelling, computing power, and high-resolution satellite-based images of the ocean surface revealing submesoscale features.

The submesoscale regime represents the margin between the rotational and balanced regime (large-scale circulation and mesoscale eddy field) and the non-rotational and unbalanced regime (3-dimensional small scale turbulence processes) meaning that they are characterised by equally strong contributions from planetary vorticity, lateral, and vertical shears accompanied by $O(1)$ Rossby and Richardson numbers (Thomas et al., 2008; McWilliams, 2016). Therefore, it seems an important component in understanding the oceanic energy cascade considering the energy that is exchanged from planetary scale to microscales **Figure 1**.

The energy cascade in geostrophic turbulence is characterised by an inverse energy cascade and was first described by Charney (1971). Nonlinear eddy-eddy interactions are thought to cause the energy transfer from the baroclinic mode to the barotropic mode at horizontal scales given by the Rossby radius of deformation. At those scales, energy is transferred to even larger barotropic scales. Scott and Arbic (2007) stated that the inverse energy cascade is not only confined the barotropic mode but also to the first baroclinic mode. It appears clear that the inverse energy cascade itself does not provide a route to energy dissipation from large to small scales. The arising question is how the oceanic energy budget is closed, i.e. how is mesoscale energy transferred to small-scale turbulence where viscous dissipation acts? Possible processes are bottom drag/ friction, internal-gravity wave emission by eddies and other unspecified process that permit a forward energy cascade to microscales (McWilliams, 2016). Even though bottom drag/ friction seems to be the most efficient energy sink of geostrophic eddy motions, the majority of ocean currents are found well separated from the bottom. McWilliams (2016) suggests submesoscale currents to be a significant conduit to energy dissipation in the ocean interior and near the surface.

In contrast to the geostrophic eddy field, the submesoscale eddy field is characterised by vertical velocities larger than the divergence induced vertical velocities (Ekman pumping mechanism) that are associated with the mesoscale regime (Lapeyre and Klein, 2006a). Therefore, submesoscale turbulence represents a high potential in observing and understanding the vertical transport of physical and biogeochemical tracers between the atmosphere-ocean interface, mixed layer, and ocean interior (Lapeyre and Klein, 2006b; Capet et al., 2008; Klein and Lapeyre, 2009). Of particular importance is the biological carbon pump and the corresponding ocean's role in regulating atmospheric carbon
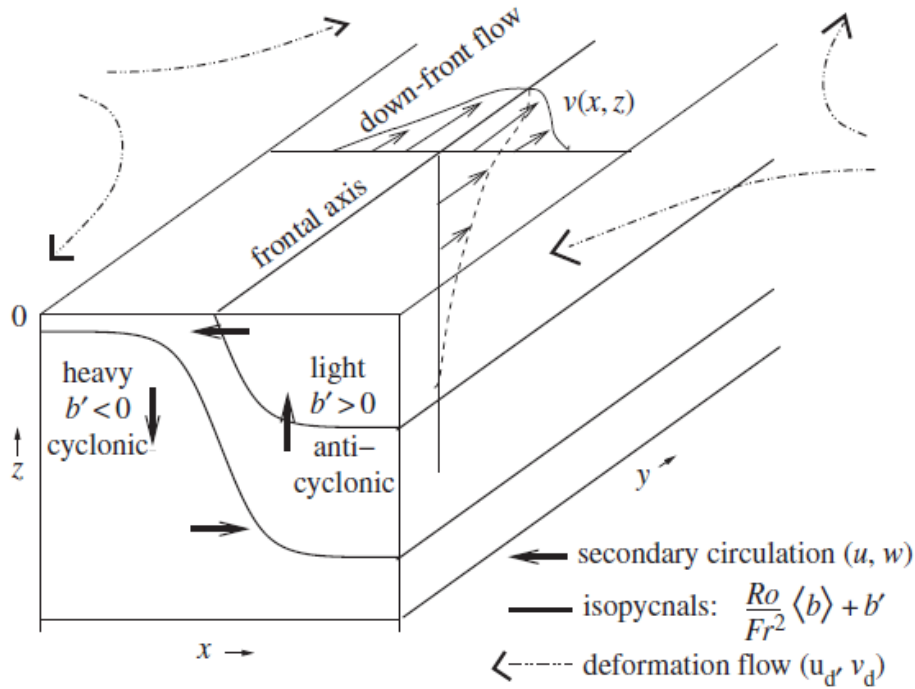
Figure 4: Schematic adapted from McWilliams (2016) visualising surface-layer frontogenesis by large-scale deformation flow. The along-front flow is in approximate geostrophic balance, whereas the secondary circulation in the cross-front plane (x-z plane) characterised by vertical velocities is ageostrophic.

dioxide that has been and will be given new insights by resolving the submesoscale flow (Fu and Ferrari, 2008; Lévy et al., 2012; Liu and Levine, 2016).

Moreover, submesoscale turbulence gives rise to seasonal variability of the eddy field since the mesoscale is not subject to it (Callies et al., 2015). Submesoscale flow can arise from two processes: mesoscale-driven frontogenesis and baroclinic instability. The former describes the intensification of pre-existing horizontal surface buoyancy gradients due to large-scale (mesoscale) straining and is visualised in **Figure 4**. The gradient increase results in a geostrophic imbalance of the along-front flow which creates an ageostrophic secondary circulation in the cross-front plane. This secondary circulation acts to restore the geostrophic balance by advectively tilting isopycnals toward the horizontal and accelerating the geostrophic flow. Additionally, it develops vertical velocities, i.e. upwelling on the light side and downwelling on the heavy side. The secondary circulation is described by the following equation

$$\frac{D(\nabla_H \rho)}{Dt} = (\nabla_H \vec{u})^T \nabla_H \rho - \frac{\partial \rho}{\partial z} \nabla_H w \tag{1}$$

where ρ is the density field, $\vec{u}$ is the velocity field, and w is the vertical velocity. **Equation 1** states the balance between the horizontal density gradient evolution $\frac{D(\nabla_H \rho)}{Dt}$, the straining of the density field by the large-scale horizontal velocity field $(\nabla_H \vec{u})^T \nabla_H \rho$, and the flattening of the isopycnals by the vertical velocity $\frac{\partial \rho}{\partial z} \nabla_H w$ (Lapeyre et al., 2006).

Thus, a disruption of the geostrophic balance by large-scale straining is counteracted by a developing ageostrophic circulation. Near the surface, the vertical velocity vanishes such that there is an irreversible cascade of surface density variance to small scales. This explains the existence of small-scale density gradients with large amplitudes. Thus, the thermal wind or geostrophic balance is maintained by horizontal ageostrophic velocity that energises the entire submesoscale range near the surface (Lapeyre et al., 2006; Capet et al., 2008).

The second mechanism that drives submesoscale flows are assigned to baroclinic instabilities in the mixed layer (Haine and Marshall, 1998; Boccaletti et al., 2007). The deeper the mixed layer the more energetic the submesoscale flow, i.e. the more potential energy is converted in kinetic energy. Since mixed layer depth variability is influenced by atmospheric forcing Callies et al. (2015) suggest that baroclinic instabilities is the responsible mechanism for submesoscale flow seasonality.

1.5 Study objective

Considering the difficulties in resolving both the mesoscale and submesoscale eddy field in high-latitude, small Rossby radius oceans using altimetry, an alternative to study the eddy field is given by high-resolution numerical ocean general circulation models. The model used in this study is the submesoscale-permitting NATL60, a model configuration based on the Nucleus for European Modeling of the Ocean (NEMO) code version 3.6 featuring a global horizontal resolution of $1/60°$ (0.8–$1.6\,\mathrm{km}$ grid spacing) and 300 vertical levels for the North Atlantic basin. It was explicitly designed in preparation for the SWOT altimeter mission. The NATL60 is supposed to simulate the oceanic scales of motion that are expected to be observed by the SWOT mission. By investigating the spatial and temporal variability of eddy scales in NATL60, the spatial and temporal correlation scales used for the SWOT inversion and mapping algorithms can be adapted. This might turn out to be a technical advancement from the current optimal interpolation applied in the AVISO mapping procedures which do not consider temporal variability of spatial correlation scales. Instead, correlation scales are fixes and mainly described as a function of latitude (Pujol et al., 2016). A basin-scale analysis in the North Atlantic of coherent structures down to scales of $10\,\mathrm{km}$ in the NATL60 was performed by (submitted for review Ajayi et al., 2019). Using an eddy detection algorithm, eddies were analysed in terms of their length scale for winter (January-March) and summertime (July-September) for multiple boxes in the North Atlantic. They show that there is a clear tendency for eddies with reduced length scales during the winter months attributed to increasing mixed layer depths, correspondingly elevated levels of potential energy, and eventually enhanced mixed layer instabilities. Moreover, the seasonal variability is associated with submesoscale eddies (10–$20\,\mathrm{km}$), whereas mesoscale eddies as suggested by Callies et al. (2015) barely undergo a sea-

sonal cycle. Other findings include the increased nonlinearity as well as the increased spread of nonlinearity for eddies in the 55°N latitudinal band compared to lower latitude.

The primary objective of this study is the comparison between observation-based and model-based derived eddy field characteristics in the central Labrador Sea. The observations are provided by two recent research expeditions that were equipped with continuously measuring current profilers giving access to high-resolution data of the horizontal velocity. The velocity fields in observations and model are analysed in the framework of a cylindrical coordinate system based on nonlinear least-squares Gauss-Newton optimisation. One of the major achievements of this study is the alternative perspective on the eddy field with respect to the altimetry products through the application of the Gauss-Newton method to the velocity data obtained by a single ship track.

The thesis is organised as follows. **Chapter 2** will introduce the study domain, the observations and the model data followed by a detailed description of the data processing and the optimisation algorithm. **Chapter 3** presents the horizontal velocity field measured during the research expeditions as well as the discrepancies in the velocity field that were observed between the ship-based and altimetry-based measurements. Afterwards, the optimisation-derived eddy characteristics from the observations will be compared with the high-resolution NATL60 model eddies. Using the NATL60 model as a reference dataset, a skill assessment will then evaluate the reliability and accuracy of the eddy characterisation method. Finally, it will be discussed to what extent the model is capable of representing the mesoscale and submesoscale velocity field regime in the Labrador Sea. The study is closed by a summary and conclusion of the results.

2   Data and Methods

This study is based on observations from two research expeditions as part of the Overturning in the Subpolar North Atlantic program (OSNAP) in the Labrador Sea and a high-resolution numerical model. The following chapter will give an overview of the available observations and the associated measuring devices, the model data as well as a detailed description for the eddy field characterisation method.

2.1   Observations

Observations are provided by two research cruise: MSM74 and MSM40. MSM74 took place from May 25 to June 26 aboard RV Maria S. Merian whereas MSM40 took place from August 6 to August 24 aboard RV Thalassa. Both cruises were primarily dedicated to the recovery and redeployment of oceanographic moorings as well as to the hydrographic survey of the water column aiming to investigate the water mass transformation and boundary current variability in the Labrador and Irminger Sea. Information about the hydrographic structure was obtained from discrete Conductivity-Temperature-Depth (CTD) profiles. The current structure of the upper water column was quasi-continuously measured with ship-based Acoustic Doppler Current Profilers (SADCP) and full-depth profiles were obtained at the CTD stations using a lowered ADCP (LADCP) system. The research area and the ship-based observations from MSM74 and MSM40 are shown in **Figure 5**.
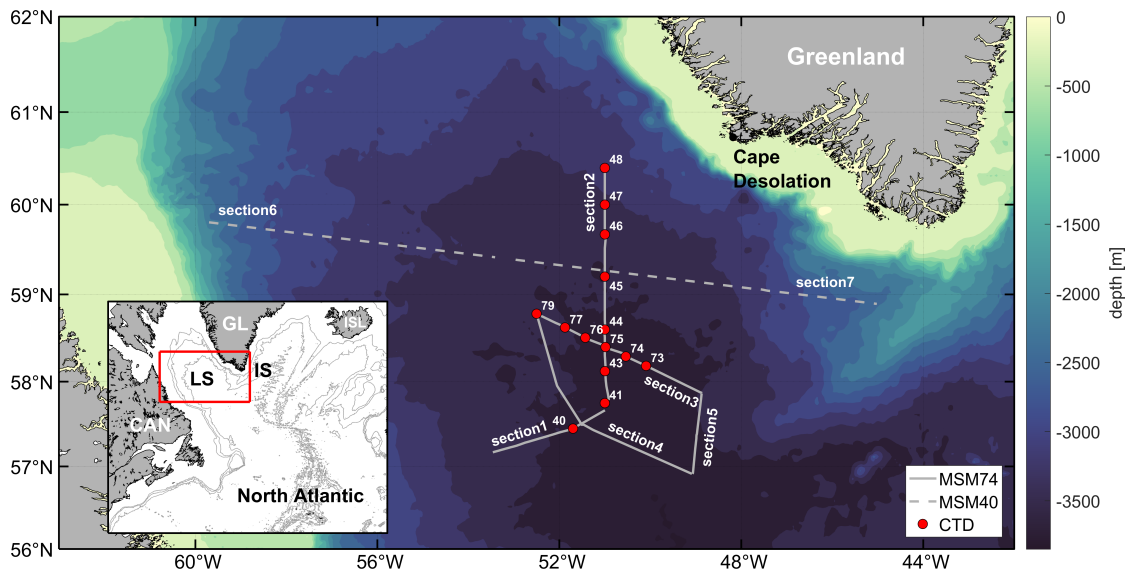

Figure 5: Map indicating the area of research in the central Labrador Sea. The solid and dashed black lines represent the analysed cruise tracks from MSM74 and MSM40, respectively. Full-depth CTD casts conducted during MSM74 are indicated by the red dots. The cast numbers are also listed. The cruise tracks are subdivided into individual sections from section 1 to section 5 covered by MSM74 and section 6 and section 7 covered by MSM40 in order to allocate the detected eddies to the cruise track segment.

Table 1: Depth range as given by manufacturer specification, actual depth range, bin size, ping mode, ping precision, and standard error for SADCPs operating throughout MSM74 and MSM40. The standard error is calculated assuming a mean amount of 25 pings per bin and averaging interval. BB stands for broad band and NB stands for narrow band.

| | MSM74 | | MSM40 | |
	38 kHz	75 kHz	38 kHz	150 kHz
depth range [m]	53.5-1621.5	17.5-809.5	34-1330	16-304
actual depth range [m]	117.5-1000	33.5-500	58-800	24-304
bin size [m]	32	8	24	8
ping mode	NB	BB	BB	BB
ping precision [cm/s]	10	15	10	8
standard error $\sigma_{\bar{v}}$ [cm/s]	2	3	2	1.6

2.1.1 Ship Acoustic Doppler Current Profiler

Both cruises were equipped with two Teledyne RD Ship Acoustic Doppler Current Profilers (SADCP) operating at 38 kHz, 75 kHz during MSM74 and 38 kHz, 150 kHz during MSM40. Depth range, bin size, ping mode, and ping precision for each individual instrument is listed in Table 1. Note that the actual depth range may deviate from the manufacturer specification. The ping precision is a measure for dispersion for a single ping per bin which ultimately depends on the specified ping mode and bin size. The standard error $\sigma_{\bar{v}}$ of the mean velocity is given by

$$\sigma_{\bar{v}} = \frac{\sigma}{\sqrt{N}} \tag{2}$$

where σ is the standard deviation of the population and N is the number of pings or samples per bin and averaging interval. The standard errors in Table 1 are computed by assuming an average amount of samples $N = 25$ per averaging interval.

In the area of interest in which the SADCP data is analysed several Conductivity-Temperature-Depth (CTD) profiles were conducted. During CTD profile measurements the ship velocity is intentionally reduced to near zero in order to ensure a stationary ship during the CTD cast. There are two reasons to exclude velocity data that were collected whenever the ship velocity fell below a certain threshold. First, during MSM74 storms and harsh weather made it sometimes impossible for the ship to stay on station when CTD profiles were taken. By excluding velocity data that was collected during low ship speed, thereby shortly before and after the CTD cast, one avoids to include velocities that were sampled too far off the proposed section. Second, during a CTD cast the ship's bow thruster which ensures a stationary ship was being activated. Therefore, velocities measured during CTD profiles are not considered since they may be afflicted by the inference with the ship's bow thruster in the upper layers near the surface. Ultimately, all data that was collected when the ship's velocity fell below 5 kn

(equivalent to $\sim 2.57\,\mathrm{m\,s^{-1}}$) was neglected.

The SADCP averaging interval was set to 60 s. The ship velocity along the analysed cruise track ranged roughly between $3\,\mathrm{m\,s^{-1}}$ and $6\,\mathrm{m\,s^{-1}}$. This results in a spatial resolution between velocity samples of 180 m and 360 m, respectively.

In addition, the velocity was filtered by percent-good data which gives the fraction of data that passed a variety of rejection criteria. Rejection criteria are for example a low signal-to-noise (S/N) ratio, a low echo amplitude, and a large error velocity. Samples below the quality threshold of 75 % were excluded from the data analysis. Current velocities were then horizontally averaged on a regular grid of 1 km resolution along the cruise track and smoothed using Gaussian weighting. The influence and cut-off radii along the cruise track were chosen as 2 km, 4 km. Influence and cut-off radii in vertical direction were set to 24 m, 48 m and 8 m, 16 m for the 38 kHz and 150 kHz instrument aboard MSM40 and 32 m, 64 m and 8 m, 16 m for the 38 kHz and 75 kHz instrument aboard MSM74 respectively.

The analysed cruise tracks (**Figure 5**) were subdivided into individual sections from section 1 to section 5 for MSM74 and section 6 and section 7 for MSM40 such that the detected eddies can be easily allocated to the cruise track segment. The MSM74 cruise track starts west of 53°W and north of 57°N pointing northeast (section 1) before heading north toward the West Greenland Shelf along 51°W (section 2). The cruise track returned from the shelf to the central Labrador Sea and continued west of 48°W and south of 58°N towards the northwest (section 3). The cruise track then turned southeast (section 4) before heading north again at 57°N, 47°W (section 5). The cruise track considered in MSM40 crosses the entire Labrador Sea from 60°W to 45°W being separated at 51°W (section 6 and 7). The wide gaps between section 1 and 2 as well as between section 6 and 7 are due to low ship speed and off-track measurements.

2.1.2 Conductivity-Temperature-Depth profiles

Several full-depth CTD profiles were conducted during MSM74 measuring the vertical properties of the hydrography along the ship track. The CTD rosette system used during the campaign was equipped with a SBE911plus CTD sonde featuring inter alia one pressure sensor, two sensors each for temperature, conductivity, and oxygen as well as fluorometer and turbidity meter. The variables of interest for this study are temperature, salinity, and pressure. While the temperature sensor was calibrated prior to the cruise, accurate calibration of the salinity data was performed during the cruise including the validation of salinity measurements against the discrete analysis of salinity water samples with the Guildline Autosal salinometer. See the MSM74 cruise report fur further details (https://doi.org/10.2312/cr_msm74).

In addition to the CTD sonde, a LADCP system was attached and installed to the CTD rosette. The LADCP system consisted of an upward and downward-looking

Teledyne Workhorse ADCP. Since the ADCPs were exchanged several times during the expedition due to technical and logistical reasons, ADCPs of different frequencies were used (300 kHz and 600 kHz). The LADCP systems measured zonal (eastward) and meridional (northward) current velocity component. It was processed by a complex algorithm using an inverse procedure with constraints from simultaneous measures by the shipboard ADCP and CTD depth information (Visbeck, 2002).

The location of the CTD and LADCP casts is shown in **Figure 5**. In total, 15 full-depth profiles were considered in this study along section 1 to section 5 and used to analyse the hydrographic properties of the eddy field in the central Labrador Sea. There are no full-depth CTD profiles along the analysed MSM40 ship track through the central Labrador Sea. Underway CTD casts taken throughout MSM40 proved to be too shallow (200–300 m) and were neglected from the study.

2.1.3 Altimetry

Ssalto/Duacs gridded and along-track multimission altimeter products available through the Copernicus Marine Environment Monitoring Service (formerly distributed by Aviso+) were taken into account during this study giving access to sea surface height with respect to a twenty-year 2012 mean in both near-real-time (NRT) and delayed-time (DL).

NRT data is mostly dedicated to providing operational oceanography with directly usable high-quality altimeter measurements on a daily basis whereas DL consists of further processing and calibration processes expected to give more accurate results than NRT. Throughout MSM74 and its data analysis NRT data was used. Since NRT is only available for a few months at most, i.e. since the latest update of the DL product, the sea level anomaly field during MSM40 was analysed using DL data.

The NRT along-track satellite data for MSM74 was taken from the altimeter mission Saral, Cryosat-2, Jason-2, Jason-3, and Sentinel-3A. The sea level anomaly is low-pass filtered along the track with a cut-off wavelength of 65 km for the global ocean and varies with latitude. This distance corresponds to the horizontal scale that can be resolved and observed by altimetry with a S/N ratio greater than 1. The filtered along-track products are subsampled such that the horizontal resolution between data points is 14 km.

The gridded sea level anomaly product combines all available altimeter mission to create a sea level anomaly field on a regular grid with a global cartesian $1/4° \times 1/4°$ resolution. It is created by applying an optimal interpolation that, inter alia, includes improved spatial and temporal correlation scales as a function of latitude and longitude (Pujol et al., 2016). Mean zonal correlation scales that are primarily latitude dependent vary from 80 km in high latitudes to more than 400 km in low latitudes. Temporal correlation scales being more equally dependent on latitude and longitude are in the range from 10 days to 30 to 45 days in midlatitudes. The gridded products are limited

to mesoscales due to the inter-satellite track distance and the revisit time period or in other words due to the spatial and temporal scaling. Particularly, the submesoscale is not expected to be resolved. However, it is argued that 15 % of the signal variance is attributable to small-scale variability which is related to submesoscale processes. In addition, the gridded products provide the sea level anomaly derived geostrophic velocities.

The so-called X-track along-track sea surface height data is used for MSM40. It comes in DL products and features 1 Hz along-track sea level anomaly time series reprocessed on a regional basis. Projected onto reference tracks it covers several coastal regions around the globe including the Labrador Sea. It is characterised by tidal corrections and a horizontal resolution between data points of 6 to 7 km. The cut-off wavelength is 40 km. The chosen X-track mission contains the satellites Topex/Poseidon, Jason-1, Jason-2, Jason-3 covering the period from February 1993 to July 2017.

2.2 Model data

This analysis will make use of data from the NATL60, a model configuration based on the Nucleus for European Modeling of the Ocean (NEMO) code version 3.6 provided by the MultiscalE Ocean Modelling (MEOM) research group at the Institut des Géosciences de l'Environnement located in Grenoble, France. It spans the North Atlantic from 26.5°N to 65°N and 80°W to 9.5°E and has a global resolution of 1/60° which corresponds to a horizontal resolution ranging between 0.8 km and 1.6 km. It features 300 vertical
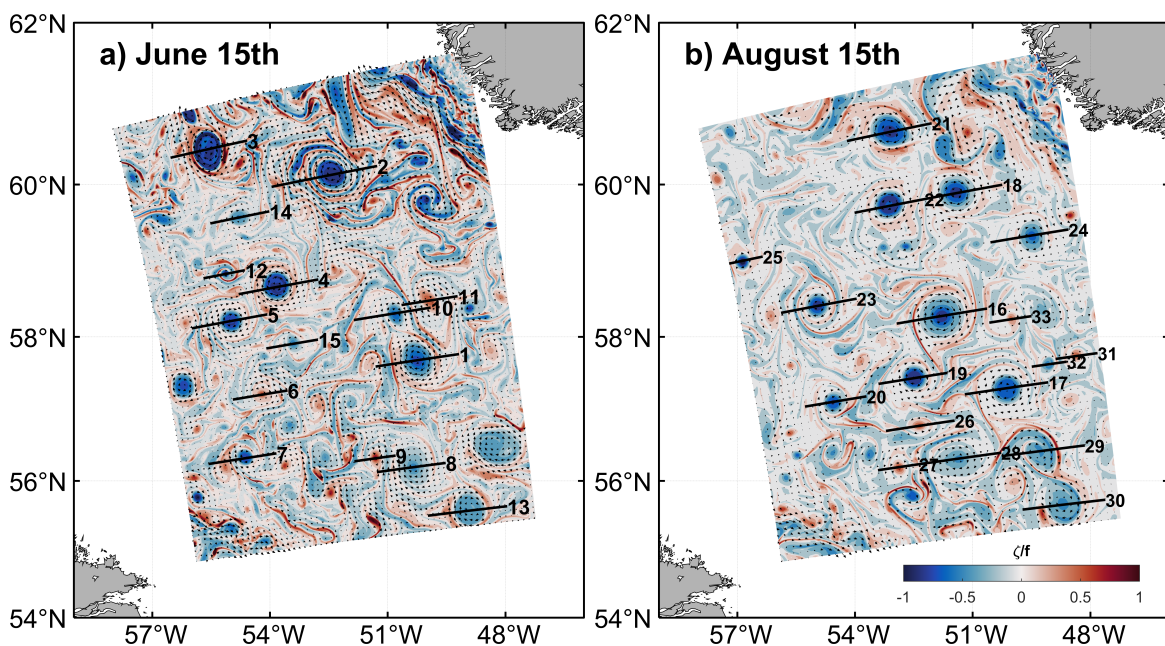

Figure 6: Instantaneous NATL60 surface relative vorticity field $\zeta = v_x - u_y$ normalised by the Coriolis parameter f and horizontal velocity field for a) June 15 and b) August 15 indicating the analysed eddies numbered from 1 to 33 in the area of interest.

levels with 1 m thickness at the surface, increasing toward 50 m in the deep ocean. Initial and boundary conditions are provided by GLORYS2-V3, an eddy permitting 1/4° resolution reanalysis developed by Mercator Ocean. Atmospheric forcing is taken from the Drakkar Forcing Set (DFS5.2) which is based on the atmospheric reanalysis ERA-interim produced by the European Centre for Medium-Range Weather Forecasts (ECMWF) featuring a temporal resolution of 3 hours and a spatial resolution of 0.7° for the period 1979-present. The provided model run originates from the second simulation CJM165 and covers the period from June 2012 to October 2013. The case study data for the characterisation of the eddy field was extracted from June 15 and August 15 2013. The instantaneous data considered here serves as the reference for the observational data of MSM74 in June and MSM40 in August. The modelled relative vorticity and horizontal velocity field from these snapshots are shown in **Figure 6** denoting the extracted eddies that were used for the characterisation of the model eddy field.

The NATL60 model consists of a staggered Arakawa-C type grid which computes the zonal velocity component u at the centres of the left and right faces, and the meridional velocity component v at the centre of the upper and lower grid faces (**Figure 7**). The tracer sits at the grid centre. The relative vorticity ζ_z was computed by a centred differencing scheme

$$\zeta_z = \frac{v^{i+1,j} - v^{i,j}}{e1f^{i,j}} - \frac{u^{i,j+1} - u^{i,j}}{e2f^{i,j}} \tag{3}$$

where $e1f$ and $e2f$ is the f-grid box spacing in zonal direction between two neighbouring v-grid points and in meridional direction between two neighbouring u-grid points respectively. As a result, the relative vorticity is located at the f-grid represented by the grid corners. Ultimately, all model variables were interpolated to the f-grid such that they lie at the same grid. In fact, the model zonal and meridional current u and v are
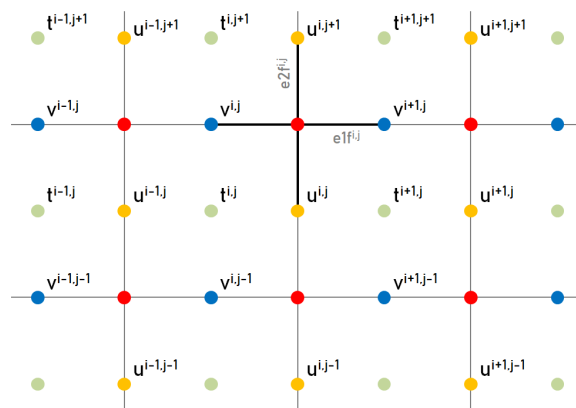

Figure 7: Visualisation of the staggered Arakawa-C grid where u is the zonal current (yellow dots), v the meridional current (blue dots), and t the tracer (green dots) such as temperature, salinity, and sea surface height. The f-grid is represented by the grid's corner (red dots) and represents relative vorticity.

not the eastward and northward current as it is the case in the SADCP but the current along the model i- and j-axis which slightly deviate from the eastward and northward axis, respectively. In order to implement the velocities to the Gauss-Newton algorithm, the model zonal and meridional current were rotated to the eastward and northward current as follows

$$u_{rot} = u\cos(\phi) - v\sin(\phi) \tag{4}$$

$$v_{rot} = u\sin(\phi) + v\cos(\phi) \tag{5}$$

where ϕ is the angle between the line that spans two neighbouring grid points and the positive x-axis (eastward).

2.3 Eddy centre problem

Following Castelão et al. (2013) and Castelão and Johns (2011), the surveyed eddies are analyzed in the framework of a cylindrical coordinate system such that every point in the xy plane is defined by the radial distance r to the origin and the azimuthal angle θ which is the angle between the positive x-axis and the line from the origin to a point P in the plane. Conversion from cartesian (x, y, z) to cylindrical coordinates (r, θ, z) is done via:

$$r = \sqrt{x^2 + y^2} \tag{6}$$

$$\theta = \arctan(y/x) \tag{7}$$

$$z = z \tag{8}$$

In cylindrical coordinates, the total velocity $\vec{V}$ is defined as the sum of the radial $(\vec{v}_r)$ and azimuthal $(\vec{v}_\theta)$ velocity component. The velocity components are given by

$$v_r = u\,\cos(\theta) + v\,\sin(\theta) \tag{9}$$

$$v_\theta = -u\,\sin(\theta) + v\,\cos(\theta), \tag{10}$$

where u and v are the velocity samples in eastward and northward direction respectively. In order to determine the relation $\vec{V}(r)$, the eddy centre needs to be estimated. The eddy centre determination is achieved by an optimisation problem which will be explained in the following.

2.3.1 Gauss-Newton algorithm

The eddy centre determination is based on the following assumption. In theory, the momentum of a perfectly axisymmetric and non-translating eddy, when projecting onto a cylindrical coordinate system, should be contained in the azimuthal velocity

component. In contrast, the radial component approaches zero. Consequently, the eddy centre is estimated by applying a nonlinear damping least-squares Gauss-Newton optimisation algorithm which minimises the difference between the total velocity and the azimuthal velocity.

In general, in least-squares problems, the goal is to minimise an objective function f

$$\min_{x \in \mathbb{R}^n} f(x) = \sum_{j=1}^{m} r_j^2(x) \tag{11}$$

Here, the objective function is the sum of squared residuals r_j from the residual vector r, and x is a n-dimensional parameter vector. Throughout this study one assumes that $m \geq n$, i.e. the number of samples is larger than the number of parameters to be determined. Fulfilling this condition prevents the model from overfitting. The goal is to determine appropriate values for the parameter vector x such that an observational data set y best fits a model ϕ. The residual $r_j = \phi_j - y_j$ then represents a measure for the discrepancy between model and observational data. In other words, the Gauss-Newton method is an iterative algorithm that solves a system of nonlinear equations and gives an estimate for unknown variables which in turn fit a theoretical model to an observational data set. In detail, the algorithm is based on computing a descent or search direction p_k^{GN} which is determined by a set of normal equations

$$J(x)^T J(x) p^{GN} = -J(x)^T r(x) \tag{12}$$

where $J(x)$ is the Jacobian which represents the first partial derivative of the residual vector r with respect to the parameter vector x and $J(x)^T$ is its transpose:

$$J(x) = \left[\frac{\partial r_j}{\partial x_i} \right] \qquad j = 1, 2, ..., m; \ i = 1, 2, ..., n \tag{13}$$

The Gauss-Newton algorithm is a modified version of Newton's method:

$$\nabla^2 f(x) p^N = -\nabla f(x) \tag{14}$$

where

$$\nabla f(x) = \sum_{j=1}^{m} r_j(x) \nabla r_j(x) = J(x)^T r(x) \tag{15}$$

$$\nabla^2 f(x) = J(x)^T J(x) + \sum_{j=1}^{m} r_j(x) \nabla^2 r_j(x) \tag{16}$$

The main advantage of the Gauss-Newton method over Newton's method is there is no need to calculate the second derivative $\nabla^2 f(x)$ since it is approximated by $J(x)^T J(x)$. The second term on the right-hand-side of (16) is neglected since $\nabla^2 r_j(x)$ is relatively

small when the residuals are small, i.e. close to the solution. For that reason, the Gauss-Newton method is also more cost-efficient and saves a lot of computational time. Solving the normal equations for p_k^{GN} yields

$$p_k^{GN} = -(J_k^T J_k)^{-1} J_k^T r_k \tag{17}$$

where the index k stands for the k-th iteration. For the sake of simplicity, the parameter vector x is neglected in this notation. The search direction p_k^{GN} is calculated at each iteration step and used for updating the parameter vector via:

$$x_{k+1} = x_k + \alpha_k p_k^{GN} \tag{18}$$

In contrast to Newton's method, the direction p_k^{GN} is always a descent direction given that J_k has full rank and $J_k^T r_k$ is non-zero. Thus, it represents a suitable search direction. However, in order to ensure a reasonable reduction of f, such that the overall algorithm converges to a local or global minimum of f, a damping factor is introduced that determines the step length at each iteration. The step length α_k is chosen such that it fulfils the following condition:

$$f(x_k + \alpha_k p_k^{GN})^T \leq f(x_k) + c_1 \alpha_k \nabla f(x_k)^T p_k^{GN} \tag{19}$$

where $c_1 \in (0, 1)$. It represents the sufficient decrease condition, also known as the Armijo rule. It prevents the line search from taking overly long steps. The constant c_1 was chosen to be 0.5. At each iteration, the algorithm starts with the maximum possible step length $\alpha = 1$. Whenever the Armijo condition is not fulfilled, the step length is reduced by the factor $\tau = 0.5$ until the inequality is valid.

The Gauss-Newton method that minimises the difference between the total velocity and the azimuthal velocity is written as:

$$\vec{V} = -u\sin(\theta) + v\cos(\theta) + \epsilon \tag{20}$$

$$\theta = \arctan(y_r/x_r) \tag{21}$$

$$y_r = y - y_c \tag{22}$$

$$x_r = x - x_c, \tag{23}$$

where x and y are the positions of the velocity samples, x_c and y_c are the positions of the eddy centre, and ϵ is the residual measuring the discrepancy between the model and the observational data. The velocity samples' longitude and latitude were converted to distance in positive x and y-direction relative to a point of reference which was chosen to be the mean longitude, latitude for a given section. During the algorithm formulation and development it was found that the algorithm gives better and more robust results when the input variables are properly scaled such that the components of the parameter

vector are equally weighted. Thus, all input variables are scaled in the range $[-1, 1]$ with preserving sign. The distance x_r and y_r and the resulting angle θ are calculated for each velocity sample along the cruise track. The final eddy centre estimate is then associated with x_c and y_c for which the radial velocity is minimised (or for which the azimuthal velocity is maximised). The principle of the Gauss-Newton method and the to be determined variables in the cartesian coordinate system are visualized in **Figure 8**.

Since the final estimate for the eddy centre ultimately depends on the start values with which the algorithm was initialized a cluster of different longitude, latitude pairs were used. The initial position that is associated with the lowest sum of squares at the last iteration then represents the best guess for the eddy centre. Castelão and Johns (2011) argue that the velocity observations near the eddy ring might be influenced by the surrounding flow. Therefore, velocity samples are excluded from the eddy ring toward its centre in an iterative procedure. The final eddy centre estimate results from taking the mean of all available eddy centre estimates along the current section. Further, it was noted by Castelão and Johns (2011) that it is necessary to account for the translational
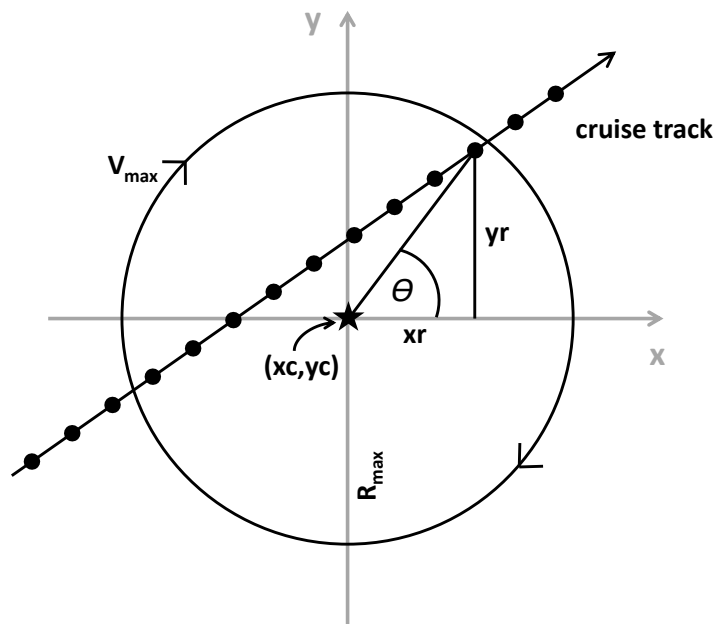

Figure 8: Sketch of the Gauss-Newton method applied to the eddy centre problem. The black arrow represents the cruise track and its heading, the black dots denote the position of the velocity samples, and the black star is the eddy centre (x_c, y_c). x_r and y_r are the components in eastward and northward direction between the position of a velocity sample and the proposed eddy centre. The black ring illustrates the eddy ring. For visualization reasons, the eddy centre is the origin of the coordinate system.

eddy speed in addition to the rotational flow in the optimisation process since the
eddy may propagate by a non-negligible distance while it is surveyed. In their study
it is argued that the final eddy centre estimate can differ by a significant amount (up
to 30 km) if one does not optimise for the mean flow. Here, the translation speed is
neglected because most of the eddies were captured within a few hours because of their
relatively small size compared to the North Brazil Rings studied by Castelão and Johns
(2011). However, attempts were made to opimize for both the eddy centre x_c, y_c and
the eddy centre motion u_c, v_c. It was found that the eddy centre displacement lies
in the order of magnitude $O(100\,\text{m})$. The corresponding eddy motions were in the
range 5 to 15 cm s^{-1}. These values were found reasonable when compared with the
eddy translation speed in the NATL60 model. Whatsoever, the algorithm appeared not
to be sufficiently robust. Further, it is questionable how reliable the optimised mean
flow is. To some extent, it seemed that the algorithm corrected for the velocity in such
a way that it distorted the eddy properties. Ultimately, the optimisation of the four
parameters (x_c, y_c, u_c, v_c) turned out to be computationally too expensive and might
be reconsidered in future studies.

For the Gauss-Newton algorithm the velocity components were split into their mesoscale
and submesoscale component. The mesoscale component is determined by applying a
boxcar filter with a horizontal and vertical filter length of 10 km and 130 m respectively.
Assuming

$$\vec{u} = \vec{u}_{ms} + \vec{u}_{sms} \tag{24}$$

where $\vec{u}_{ms}$ is the mesoscale component and $\vec{u}_{sms}$ the submesoscale component, the
submesoscale component is then the difference between the total and mesoscale ve-
locity component. The mesoscale velocity component was used for the eddy centre
determination.

2.4 Gauss-Newton derived eddy characteristics

The accurate determination of the eddy centre allows for the derivation of eddy defining
parameters such as radius, azimuthal velocity, relative vorticity, etc. Throughout this
study, attributable to the assumption in the Gauss-Newton algorithm, it is assumed
that the sampled eddies are perfectly axisymmetric and non-translating. Further, the
eddies are analysed in the framework of an idealised vortex. This idealized vortex is
defined as follows

$$v_\theta(r) = \begin{cases} r\frac{V_{max}}{R_{max}} & \text{for } r < R_{max} \\ V_{max}e^{-\frac{(r-R_{max})}{\lambda}} & \text{for } r > R_{max} \end{cases} \tag{25}$$

where r is the radius, R_{max} the maximum radius, V_{max} the maximum azimuthal velocity, and λ the e-folding scale. The velocity structure is characterized by solid-body rotation in the inner core ($r < R_{max}$), i.e. the azimuthal velocity is proportional to the radius. The outer ring ($r > R_{max}$) velocity structure is for the moment assumed to follow an exponential function. This was, inter alia, also suggested by Olson (1980) who concluded the outer ring velocity structure from the 1977 Cyclonic Ring Experiment on Gulf Stream rings.

Each eddy section obtained from either MSM74, MSM40, or NATL60 will be subdivided into two radial sections and analysed individually. Since the eddies were never crossed exactly through their centre, the subdivision occurs where the distance to the eddy centre is minimum. The analysed eddy characteristics will now be introduced.

2.4.1 Radius, azimuthal velocity, and outer ring decay scale

Once having determined the eddy centre x_c, y_c in the cartesian frame, one can estimate the radius and the maximum azimuthal velocity. The maximum azimuthal velocity can be understood as the swirl velocity, i.e. the rotational velocity component of the vortex. However, this definition needs to be used with caution since as previously mentioned the rotational velocity was not explicitly optimised. Therefore, it is preferred to stick to the definition of maximum azimuthal velocity. The radius is defined as the distance from the eddy centre at which the maximum azimuthal velocity occurs. Radius and maximum azimuthal velocity are thus denoted as R_{max} and V_{max} and are defined as the mean of both radial sections, if applicable.

An idealized eddy is in solid-body rotation in the inner core. Observations and numerical studies, however, show that the velocity structure differs from solid-body rotation near the eddy ring. Apart from the maximum azimuthal velocity, this study attempts to determine the deviation of the azimuthal velocity from solid-body rotation within the inner core and especially at R_{max}. Particularly, it estimates the maximum azimuthal velocity the eddy would have if it were in solid-body rotation. This is achieved by applying a linear fit to the inner core velocity data that is in solid-body rotation. The theoretical maximum azimuthal velocity the eddy would have for solid-body rotation is then obtained by extracting the velocity at R_max from the linear fit.

The outer ring e-folding scale λ is determined by applying an exponential fit to the outer ring azimuthal velocity (25).

2.4.2 Relative vorticity and Rossby number

Relative vorticity is defined as the curl of the velocity vector $\vec{u}$. In cartesian coordinates it is defined as

$$\vec{\zeta} = \vec{\nabla} \times \vec{u} = \left(\frac{\partial w}{\partial y} - \frac{\partial v}{\partial z} \right) \vec{e}_x + \left(\frac{\partial u}{\partial z} - \frac{\partial w}{\partial x} \right) \vec{e}_y + \left(\frac{\partial v}{\partial x} - \frac{\partial u}{\partial y} \right) \vec{e}_z \qquad (26)$$

where $\vec{u} = (u, v, w)$, $\vec{\nabla} = \left(\frac{\partial}{\partial x}, \frac{\partial}{\partial y}, \frac{\partial}{\partial z}\right)$, and $\zeta_z = \frac{\partial v}{\partial x} - \frac{\partial u}{\partial y}$ is the vertical component describing the relative vorticity in the horizontal plane. In cylindrical coordinates it is given by

$$\vec{\zeta} = \vec{\nabla} \times \vec{v} = \left(\frac{\partial v_z}{\partial \theta} - \frac{\partial v_\theta}{\partial z}\right)\vec{e}_r + \left(\frac{\partial v_r}{\partial z} - \frac{\partial v_z}{\partial r}\right)\vec{e}_\theta + \left(\frac{\partial (rv_\theta)}{\partial r} - \frac{\partial v_r}{\partial \theta}\right)\vec{e}_z \tag{27}$$

where $\vec{v} = (v_r, v_\theta, v_z)$ and $\vec{\nabla} = \left(\frac{\partial}{\partial r}, \frac{\partial}{\partial \theta}, \frac{\partial}{\partial z}\right)$. Neglecting the radial velocity component v_r the relative vorticity is thus defined as

$$\zeta_z = \frac{1}{r}\frac{\partial}{\partial r}(rv_\theta) \tag{28}$$

Inserting the linear velocity model of Equation (25) gives the following estimate for the eddy vorticity

$$\zeta_z = 2\frac{V_{max}}{R_{max}} \tag{29}$$

The dimensionless Rossby number of the gradient flow is defined as

$$Ro = \frac{V_{max}}{f_0 R_{max}} \tag{30}$$

and describes the ratio between inertial and Coriolis forces. For low Rossby numbers ($Ro << 1$) the flow is dominated by the Coriolis acceleration , i.e. it is in approximate geostrophic balance and therefore significantly influenced by the Earth's rotation. It also represents a measure for the nonlinearity of the flow regime which increases in importance for large Rossby numbers.

2.4.3 Sea surface height signal

Information about the eddy velocity and radius can be used to estimate the sea surface height signal using the cyclogeostrophic balance

$$fv_\theta = g\frac{\partial \eta}{\partial r} - \frac{v_\theta^2}{r} \tag{31}$$

where f is the Coriolis parameter, g the gravitational acceleration, and η the sea surface elevation. It describes the balance between the Coriolis acceleration, the pressure gradient force, and the centrifugal acceleration. Following Castelão and Johns (2011), the azimuthal velocity can be expressed in terms of ζ_z

$$v_\theta = r\frac{V_{max}}{R_{max}} = \frac{1}{2}r\zeta_z \tag{32}$$

Inserting in the cyclogeostrophic balance (31) yields

$$\frac{\zeta_z}{4g}(2f + \zeta_z)r = \frac{\partial \eta}{\partial r} \tag{33}$$

Intergrating along the radius while assuming that the Coriolis parameter is constant ($f = f_0$) gives us the relationship between sea surface height and radius for the inner core

$$\eta(r) = \eta_0 + \frac{\zeta_z}{8g}(2f_0 + \zeta_z)r^2 \qquad \text{for } r < R_{max} \tag{34}$$

where η_0 is the integration constant and the maximum sea surface elevation. For the outer ring one inserts the exponential velocity model in (31)

$$fV_{max}e^{-\frac{(r-R_{max})}{\lambda}} = \frac{1}{g}\frac{\partial \eta}{\partial r} - \frac{1}{r}\left(V_{max}e^{-\frac{(r-R_{max})}{\lambda}}\right)^2 \tag{35}$$

$$\frac{1}{g}\left[fV_{max}e^{-\frac{(r-R_{max})}{\lambda}} + \frac{1}{r}\left(V_{max}e^{-\frac{(r-R_{max})}{\lambda}}\right)^2\right] = \frac{\partial \eta}{\partial r} \tag{36}$$

Integrating along the outer ring yields the following sea surface height structure

$$\eta(r) = \frac{V_{max}}{g}\left(-f\lambda e^{-\frac{(r-R_{max})}{\lambda}}\right) \qquad \text{for } r > R_{max} \tag{37}$$

In this expression the contribution of the centrifugal acceleration to sea surface height in the outer ring is neglected since it is relatively small compared to the Coriolis accerelation. The maximum sea surface elevation η_0 is then eventually determined by equating (34) and (37) for $r = R_{max}$

$$\eta_0 = -\frac{\zeta_z}{8g}(2f_0 + \zeta_z)R_{max}^2 - \frac{V_{max}}{g}\lambda f \tag{38}$$

$$= -\frac{V_{max}}{2g}\left(V_{max} + f_0 R_{max} + 2\lambda f\right) \tag{39}$$

2.4.4 Nonlinearity

Nonlinearity parameter is adapted from quasi-geostrophy theory and is applied as follows

$$\alpha = \frac{V_{max}}{\beta_0 R_{max}^2}$$

where $\beta_0 = df/dy$ is the planetary vorticity gradient. The nonlineary parameter takes into account the speed-based eddy length scale R_{max} and maximum azimuthal velocity V_{max}, and describes in general the ratio between the relative vorticity advection and planetary vorticity advection. The term nonlinear relates to definition of coherent

(mesoscale) eddies for which the the ratio is $\alpha > 1$.

2.5 Power spectral density

The along-track horizontal velocity $(u^2 + v^2)^{1/2}$ field obtained from MSM74 and MSM40 was analysed in terms of mesoscale and submesoscale spatial variability. Spectral analysis was applied to the 38 kHz, 75 kHz, and 150 kHz ADCPs using Welch's method with a Hamming window of 50 % overlap. As a result, the power spectral density is given as a function of spatial frequency. The spatial frequency, denoted as the wavenumber k, is a measure of how often a signal repeats per unit of distance. Given the unit of distance 1 km, the wavenumber is given in cycles per kilometre (cpkm). The power spectral density is in units of $m^2\,s^{-2}$/cpkm. Aiming to compare the observations to the NATL60 model, an artificial ship track was simulated through the central Labrador Sea in the respective months of MSM74 and MSM40. The model velocity was then interpolated to a track with an along-track resolution of 1 km.

3 Results and Discussion

In the following chapter, the along-track horizontal velocity field as measured during MSM74 and MSM40 will be used to analyse and characterise selected eddies in the central Labrador Sea. It will be shown that the high-resolution ship-based measurements feature large discrepancies to the satellite-derived geostrophic velocities. The eddy field observed during the research expeditions is then characterised using the Gauss-Newton optimisation algorithm and compared with model eddies extracted from NATL60. Model eddies are found to have on average smaller radii and higher azimuthal velocities and are consequently more nonlinear. The hydrographic survey suggests the presence of IR with warm, salty lenses of water either surface trapped or overlaid by a cold, fresh cap of water. A Gauss-Newton optimisation sensitivity experiment applied to the model data ensures that the eddy reconstruction reproduces the eddy characteristics in most cases within an acceptable error margin. The mesoscale eddy field is found to be fairly well represented, whereas the submesoscale flow regime suffers from an underrepresentation.

3.1 Ship-based horizontal velocity field

Zonal and meridional current velocities were quasi-continuously measured during both research cruises. The smoothed and gridded horizontal velocities for the upper 800 m are shown in **Figure 9** for MSM74 and in **Figure 10** for MSM40. The black lines serve as a separation line such that the velocity field can be assigned to the individual sections shown in **Figure 5**. The velocity records indicate large spatial variability along the ship tracks with respect to mean background current which is here estimated to be well below $10\,\mathrm{cm\,s^{-1}}$. The spatial variablity of horizontal velocity is likely caused by the presence of mesoscale eddies. The main indicator for the mesoscale eddy activity is the changing sign of the zonal and meridional velocity components on scales of several tens of kilometers along the ship track. The most dominant eddy features that were crossed near the center are E1 (section 1, 170 km), E6 (section 4, 800 km), and E9 (section 5, 1100 km) during MSM74 (**Figure 9**) and E12 (section 7, 400 km) during MSM40 (**Figure 10**). The remaining velocity variability along the sections is probably induced by eddies that were either crossed a few kilometers off the centre or were only scratched near the rim.

Whatsoever, the horizontal velocity field, i.e. the eddy field, as measured by the SADCP is characterised by maximum velocity magnitudes in the range of 50 to $60\,\mathrm{cm\,s^{-1}}$. In most cases, especially during MSM40, the horizontal velocity is surface intensified (1 to 300 m) suggesting baroclinicity and thus vertical shear of horizontal velocites within the water column. However, a barotropic velocity structure featuring constant velocities with increasing depth is evident as well.
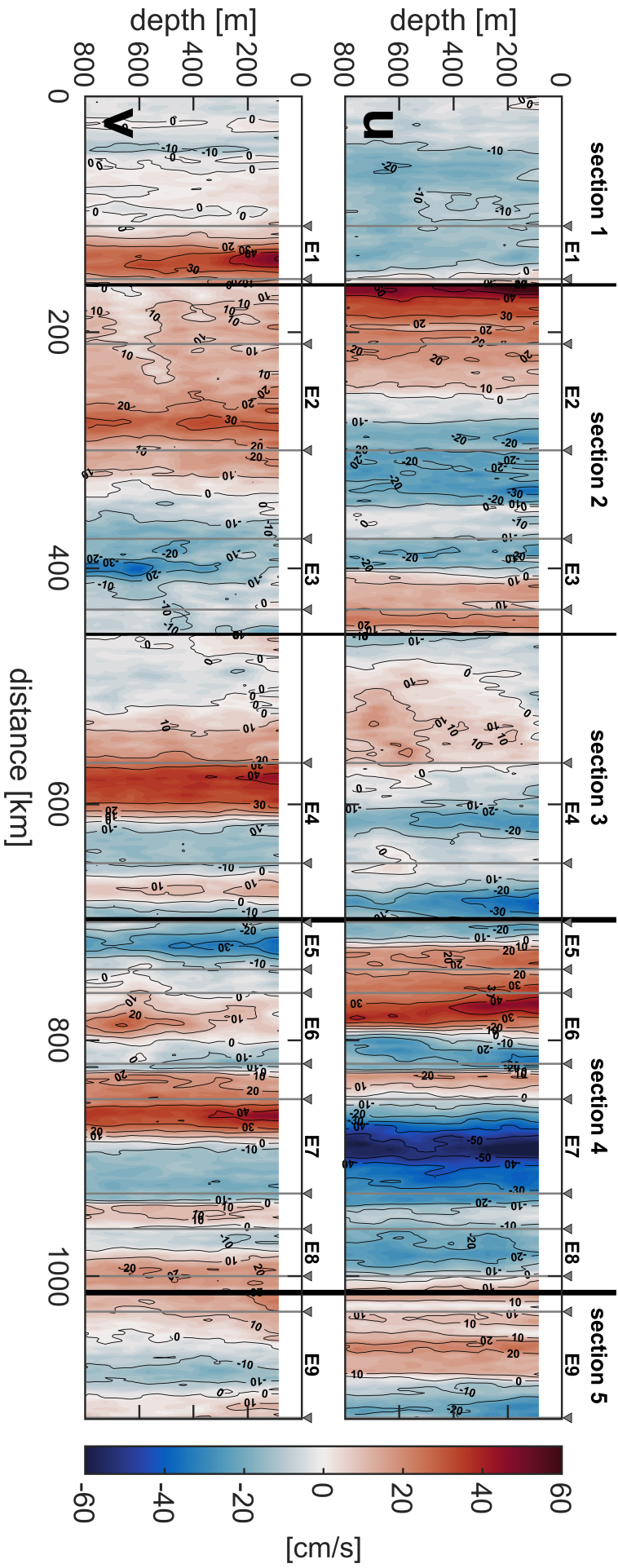
Figure 9: Smoothed and gridded 38 kHz SADCP data showing the zonal current u (upper panel) and meridional current v (lower panel) velocity along the MSM74 cruise track for the upper 800 m. Thick black lines represent the separation of the MSM74 cruise track in section 1 to section 5 as shown in Figure 5. The overlaid gray lines represent the eddy influence area that was considered to determine the individual eddy characteristics using the Gauss-Newton method at later stage.
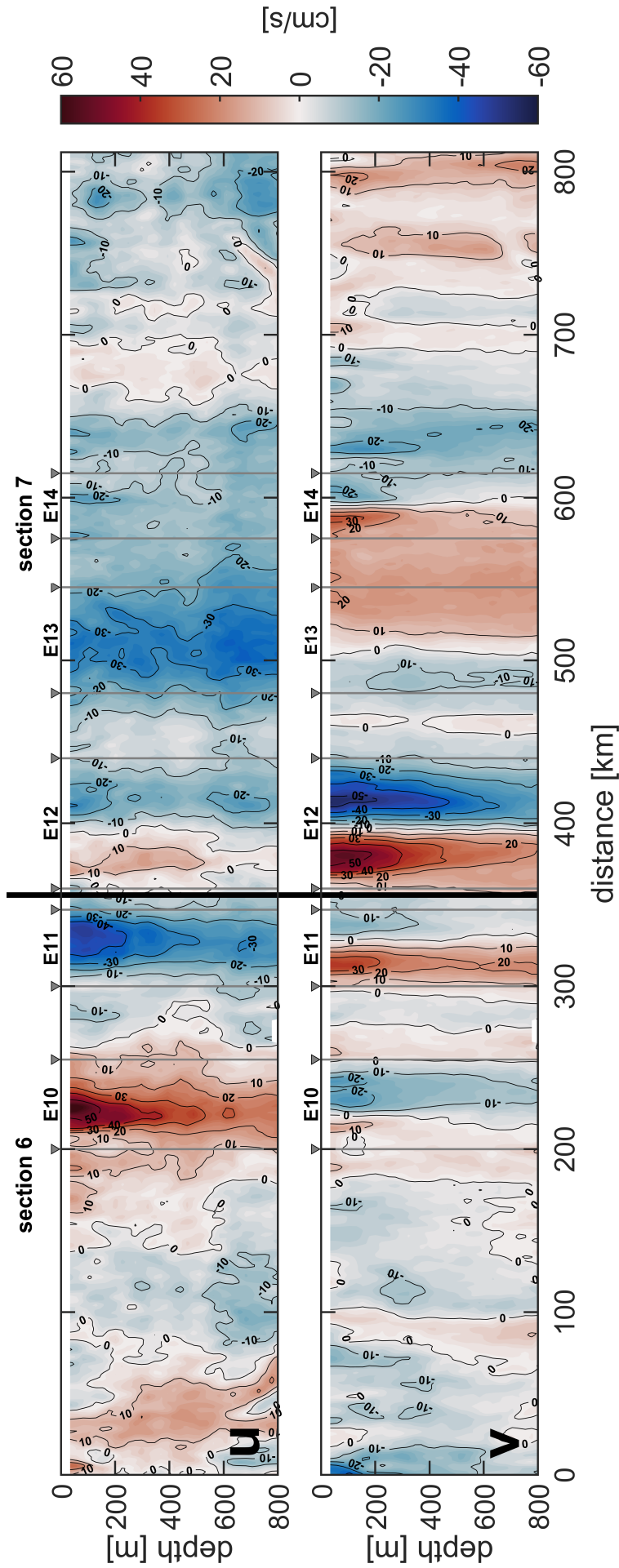
Figure 10: Same as **Figure 9** but for section 6 and section 7 during MSM40.

Both the zonal and the meridional velocity were divided into their mesoscale and sub-mesoscale velocity component by applying a simple boxcar filter. The resulting velocity decomposition is shown for both ADCPs and for both cruises in the supplementary material (**Figure A1** to **Figure A8**). Note that the 75 kHz data from MSM74 contains measurement artifacts that could not be removed by the applied post-processing procedure and expresses itself in the artifical downward signal propagation at mid-depths (**Figure A4**). The horizontal velocity fields in **Figure A4** and **A8** cleary indicate a maximum of submesoscale velocities near the surface in the upper 100 m featuring magnitudes of up to more than $10\,\mathrm{cm\,s^{-1}}$. For both MSM74 and MSM40 the velocity magnitudes are decreasing with increasing depth. Overall, it seems that the along-track variability as well as the velocity magnitude of the submesoscale flow is larger for MSM74 than MSM40.

3.2 Altimetry-derived eddy field

Gridded sea level anomaly maps including the sea level anomaly derived surface velocities were provided in NRT during MSM74 and used to adapt the ship track through the mesoscale eddy field. **Figure 11** visualises the gridded sea level anomaly with the associated geostrophic velocities from June 6 (**Figure 11a**) and June 13, 2018 (**Figure 11b**) in addition to the cruise tracks and the corresponding upper 300 m average velocity vectors during MSM74.

The eddy field on June 6 according to the altimetry-derived sea level anomaly field featured a strong cyclonic eddy (negative sea level anomaly) surrounded by three anticyclonic eddies (positive sea level anomaly). The formation of such coherent compound vortices have been extensively studied in laboraty and numerical simulations (Van Heijst and Kloosterziel, 1989; Van Heijst et al., 1991; Kloosterziel and Van Heijst, 1991; Carnevale and Kloosterziel, 1994; Beckers and Van Heijst, 1998). They are believed to emerge from an isolated monopolar vortex which is characterised by a vorticity core surrounded by a vorticity shield with opposing vorticity. Moreover, the background strain field that induces circular azimuthal velocity variations is argued to drive the instabilities which in turn eventually form the compound vortices (Higgins et al., 2002). The sea level anomaly structure detected in **Figure 11a** resembles the general structure of a triangular vortex, first reported by Kloosterziel and Van Heijst (1991). The most dominant feature on June 13 was a meridionally aligned eddy dipole. At first sight, there is good agreement between the ship-based and altimetry-derived velocities. However, particularly during MSM74 there is evidence for numerous discrepancies. The most prominent discrepancy is seen for the intense eddy dipole in (**Figure 11b**). The gridded sea level anomaly indicates an intense cyclone that spans from 58°-59°N and 50°-52.5°W which stands in contrast to the analysed SADCP data which rather suggests the existence of two smaller-scale cyclones (see E4 and E5 along section 3). Further, the

anticyclone in 57.7°-58.2°N and 51.5°-52.5°W that was captured by the Gauss-Newton algorithm does not appear at all in the gridded sea level anomaly or gridded horizontal velocity field. In fact, SADCP velocities at the southern flank of E6 are opposite to the geostrophic velocities. Considering its estimated size and measured azimuthal velocity, the eddy in 57.3°-57.9°N and 48.5°-49.5°W (E9) also seems inadequately represented by altimetry.

Overall, it appears that the eddies tracked in the SADCP data are smaller in size compared to the altimetry products. A recent study from (Amores et al., 2018) investigating the ability of altimetry products in the reconstruction of the eddy field in the Mediterranean Sea and in the North Atlantic has come to a similar result. The poor spatial and temporal resolution of satellite tracks is responsible for the eddy field distortion, such that amplitude and radius are not accurately reproduced. Since the across-track distance of satellite tracks is well below the Rossby radius of deformation in the Labrador Sea ($L_D \sim 10\,\text{km}$), aliasing effects are expected to be included in the
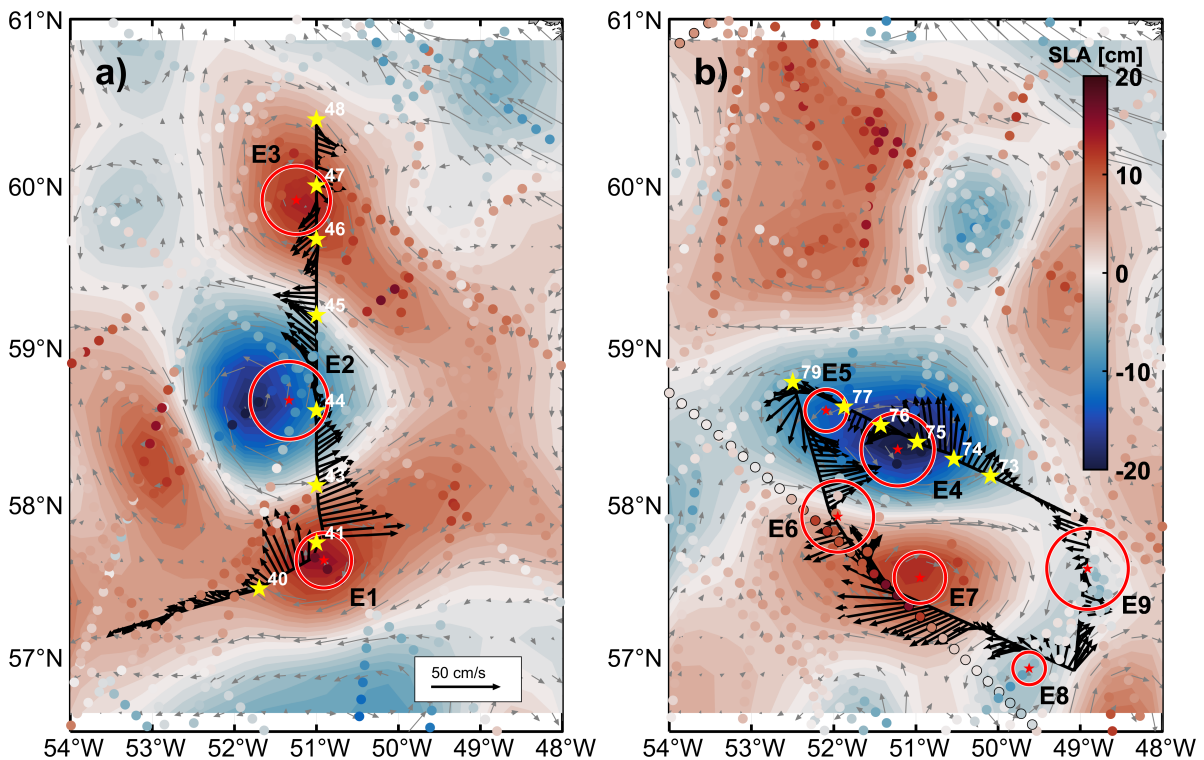

Figure 11: Upper 300 m average SADCP velocities (black arrows) sampled during MSM74 along a) section 1 and 2 and b) section 3 to 5. SADCP velocites are plotted above gridded near-real time sea level anomaly maps from a) June 6 and b) June 13, 2018 adapted from Copernicus/AVISO+ with overlying sea level anomaly derived velocities (gray arrows). The scattered data points represent along-track sea level anomaly from two previous and two following days relative to the date of the gridded sea level anomaly map or SADCP section. The red stars and red circles denote the Gauss-Newton estimated eddy centre and ring for eddies sampled along the cruise track. Eddies detected along the ship track are consecutively numbered. The yellow stars represent full depth CTD stations. CTD casts numbers are also shown.

merged sea level anomaly maps. As a consequence, smaller-scale eddies are often interpreted as larger-scale structures. This is also true for the case study data obtained from MSM74.

Sea level anomaly maps are derived by gridding and optimal interpolation using objective analysis of the available along-track sea level anomaly data. The mapping methodology includes geophysical corrections and reproduced smoothing of the along-track data, as well as predefined longitude and latitude dependent spatial and temporal correlation scales and measurement errors. These parameters, nonetheless, represent a compromise between the eddy field properties that are desired to be resolved and the sampling capabilities that are associated with the altimeter constellation (Pujol et al., 2016). Moreover, the spatial and temporal across-track sampling limits the reconstruction of dynamical oceanic features even in the mesoscale range. While gridded sea level anomaly products may fail the mesoscale signal reconstruction, along-track sea level anomaly products with a resolution of 1 Hz are more suitable for the capture of smaller-scale features. In order to verify whether the eddy field reconstruction suffers from the interpolation onto a 2-dimensional grid, the NRT along-track sea level anomaly is plotted in addition to the gridded product in **Figure 11**. The along-track sea level anomaly data for two previous and two following days with respect to June 6 and June 13 for all available satellites at that time mostly coincide with the merged sea level anomaly data. Here, the focus is put on eddy E6 in **Figure 11a** which does not appear in the gridded product at all. A closer look at the highlighted satellite track (filled circles with black marker edges) reveals a local minimum in sea level anomaly with respect to the global maximum southeast of E6 close to E7. This local maximum might accompany with another anticyclone as suggested by the Gauss-Newton eddy tracking method. Furthermore, it implies that E6 is independent of the velocity and sea level anomaly field that is associated with E7. This highly suggests that the sea level anomaly signal was smoothed out by the applied relatively coarse correlation scales and underlines the aliasing effect introducing the eddy field distortion due to low-resolution across-track sampling.

The sea level anomaly data during MSM40 is considered as well in the analysis (**Figure 12**). Note that sea level anomaly for both gridded and along-track products is only available in delayed time mode. The only dominant feature in the MSM40 dataset is eddy E12 that was detected around 52.2°W, 59.4°N along section 7. All other eddies were surveyed near the rim. E12 is detected by the altimetry products but its size and magnitude may be underrepresented.

The Gauss-Newton algorithm provides an alternative perspective on the eddy field and correspondingly on the spatial distribution of eddy kinetic energy based on a single ship track. Unfortunately, it also comes with some disadvantages. These disadvantages include inter alia the fact that the eddy centre determination ultimately depends on the location of the ship track through the eddy. In addition, the algorithm does not
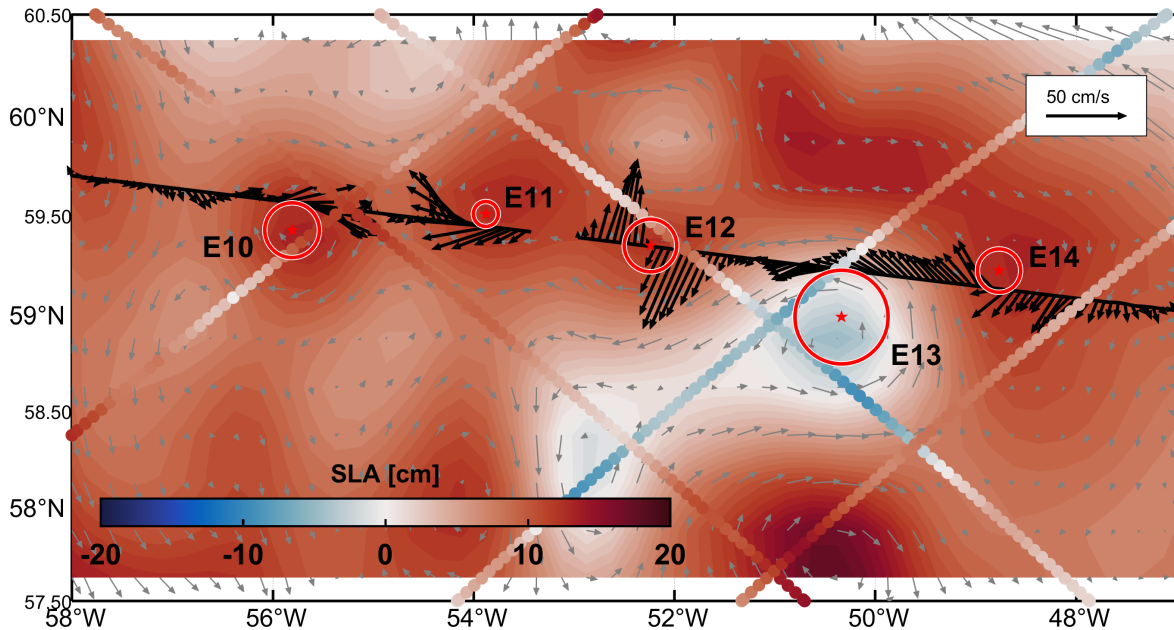
Figure 12: Upper 300 m average SADCP velocities (black arrows) sampled during MSM40 along section 6 and 7. SADCP velocites are plotted above gridded sea level anomaly maps from August 17, 2014 adapted from Copernicus/AVISO+ with overlaying sea level anomaly derived velocities (gray arrows). Since near-real time data is only available for a few months at most after they have been uploaded on Copernicus/AVISO+, the delayed and reprocessed product projected onto reference tracks was used for the analysis of MSM40. The shown along-track sea level anomaly was extracted from August 10, 11, 17, 17, and 20.

account for the eddy asymmetry which in turn could influence the convergence of the objective function in the optimisation. The optimisation related disadvantages will be discussed in detail at alter stage when the Gauss-Newton algorithm is subject to an eddy reconstruction skill assessment.

3.3   Gauss-Newton derived eddy characteristics

The Gauss-Newton algorithm applied to the transformed azimuthal and radial velocity components give rise to analysis of eddy characteristics in the framework of a cyclindrical coordinate system. The derived eddy characteristics are listed in **Table 2** indcluding a short variable description. Note that the mesoscale velocity component was used for the eddy centre computation.

In total, 14 eddies were detected of which 9 were surveyed during MSM74 and 5 during MSM40. Of those 14 eddies, 6 eddies feature a cyclonic sense of rotation and 8 eddies an anticyclonic sense of rotation. The maximum radii and azimuthal velocities of eddies derived from the observations lie in the range 7–35 km with a mean of 20 km. Minimum and maximum azimuthal velocity magnitudes are found to be as low as 20 cm s^{-1} and as high as 60 cm s^{-1}. The mean velocity is 35 cm s^{-1}. A maximum of only two radial sections are available per eddy since the research expeditions were not exclusively dedicated to the survey of the eddy field. R_{max} is the mean of those two

Table 2: Gauss-Newton derived eddy characteristics: maximum radius R_{max}, maximum azimuthal velocity V_{max}, outer ring decay scale λ, maximum sea surface height η_0, inner core relative vorticity ζ_{in}, Rossby number Ro of the gradient flow, theoretical maximum azimuthal velocity V_{sb} for solid-body rotation, and eddy type if applicable. Positive values for azimuthal velocity, relative vorticity, and Rossby number denote anti-clockwise rotation (cyclone), negative values denote clockwise rotation (anticyclone). Values are to be understood as the mean of both radial sections with given standard deviation for each eddy. The abbreviations IR1 and IR2 denote the two Irminger ring eddy types. Some eddies were only scratched near their outer ring and therefore do not provide any information about the inner core velocity. Missing error estimates are due to the fact that the eddy was either only scratched near the outer ring or that only one radial section was available. The mean was calculated using the variable's magnitude.

Eddy Nr #	ADCP [kHz]	R_{max} [km]	V_{max} [cm/s]	λ [km]	η_0 [cm]	ζ_{in} 10^{-5} [1/s]	Ro	V_{sb} [cm/s]	type
MSM74									
E1	38	22.8	−44.0	16.0	16.0	−3.9	−0.16	-	IR1
	75	23.3	−44.6	17.1	17.1	−3.8	−0.16	-	IR1
E2	38	33.7 ± 9.9	27.9 ± 6.8	36.8	19.4	1.8 ± 0.9	0.07	-	IR2
	75	35.2 ± 8.2	27.8 ± 7.1	34.0	18.6	1.7 ± 0.8	0.06	-	IR2
E3	38	23.0 ± 1.6	−20.0 ± 4.0	16.9 ± 0.2	7.5	−1.7 ± 0.2	−0.07	-	IR2
	75	23.1 ± 2.2	−21.0 ± 1.9	16.4 ± 3.2	7.8	−1.8 ± 0.0	−0.07	-	IR2
E4	38	22.2 ± 13.2	31.6 ± 10.9	22.5 ± 3.9	13.9	3.1 ± 0.1	0.11	-	-
	75	21.6 ± 13.3	30.5 ± 13.3	25.3 ± 1.0	14.4	3.0 ± 0.1	0.11	-	-
E5	38	21.9	32.4	18.0 ± 4.1	12.4	3.0	0.12	-	-
	75	17.1	29.9	26.7 ± 12.0	13.7	3.5	0.14	-	-
E6	38	22.3 ± 5.0	−37.1 ± 9.0	19.5 ± 17.6	15.0	−3.3 ± 0.1	−0.14	−46.3 ± 0.10	-
	75	22.8 ± 5.2	−37.6 ± 6.3	19.9 ± 17.4	15.5	−3.3 ± 0.2	−0.13	−47.6 ± 0.04	-
E7	38	18.3	−60.3	39.1	33.7	−6.6	−0.27	-	-
	75	18.8	−60.4	41.5	36.1	−6.4	−0.26	-	-
E8	38	11.3	22.1	18.0	6.7	3.9	0.16	-	-
	75	12.2	24.7	17.7	7.6	4.1	0.17		-
E9	38	26.8 ± 2.5	24.4 ± 3.0	9.8	7.4	1.8 ± 0.4	0.07	48.2	-
	75	29.3 ± 0.4	24.9 ± 4.2	10.5	8.1	1.7 ± 0.3	0.07	48.6	-
MSM40									
E10	38	16.0	−49.0	8.1 ± 4.9	11.0	−6.1	−0.24	-	-
	150	15.5	−47.9	8.1 ± 4.9	10.8	−6.2	−0.25	-	-
E11	38	6.8	−41.7	14.0	10.2	−12.3	−0.49	-	-
	150	7.0	−42.0	13.5	10.0	−12.0	−0.48	-	-
E12	38	17.8 ± 0.2	−49.1 ± 1.1	15.5 ± 4.2	16.5	−5.5 ± 0.1	−0.22	−71.9 ± 0.01	-
	150	17.5 ± 0.5	−50.6 ± 0.6	15.7 ± 5.2	17.1	−5.8 ± 0.1	−0.23	−75.0 ± 0.04	-
E13	38	26.0	32.3	40.2 ± 29.4	22.3	2.5	0.10	-	-
	150	26.6	31.4	46.3 ± 41.6	24.3	2.3	0.09	-	-
E14	38	13.0 ± 0.8	−23.7 ± 4.6	30.4 ± 5.1	11.4	−3.6 ± 0.5	−0.15	-	-
	150	13.4 ± 0.9	−26.3 ± 5.0	26.5 ± 2.9	11.5	−3.9 ± 0.5	−0.18	-	-
Mean	38	20.1 ± 6.9	35.4 ± 12.0	21.8 ± 10.6	14.5 ± 7.2	4.2 ± 2.8	0.17 ± 0.11	55.5 ± 14.3	-
	75/150	20.2 ± 7.3	35.7 ± 11.7	22.1 ± 11.4	15.2 ± 7.7	4.3 ± 2.7	0.17 ± 0.11	57.1 ± 15.5	-

radial sections and the given error estimates are the corresponding standard deviations. Even though this is not really representative for the eddy structure, it may give an idea about the eddy asymmetry. High standard deviations are found for E2, E4, and E6 for both R_{max} and V_{max}. The exponential decay rate λ of the outer ring velocity structure outside R_{max} features strong variations from 8 km to over 40 km and is on average 22 km with a standard deviation of 11 km. The maximum sea surface height signal η_0 is estimated to lie in the range 7–35 cm with a mean of 15 cm. The mean inner core relative vorticity ζ_{in} and the mean Rossby number of the gradient flow Ro

are $4.2 \cdot 10^{-5}\,\mathrm{s}^{-1}$ and 0.17. Both relative vorticity and Rossby number are roughly twice as high for MSM40 than MSM74 which is to the most part attributed to the larger azimuthal velocities during MSM40. In particular, the Rossby number shows a tendency for increased nonlinearity for the MSM40 dataset. Notably, high Rossby number values are associated with relatively small radii as well as large velocity and sea surface height magnitudes. For three eddies (E1, E6, and E12), whose centres were only barely missed, a complete inner core velocity structure was obtained. This data was used to calculate the theoretical maximum azimuthal velocity of the eddy if it were in solid-body rotation by applying a linear fit to the inner core velocity profile. On average the maximum azimuthal velocity for solid-body rotation is more than 1/3 higher than the actual azimuthal velocity. According to the optimisation, eddy E9 was crossed close to its centre as well. It was neglected, though, because its inner core velocity structure featured large deviations from solid-body rotation such that a linear fit could not be applied.

The application of the Gauss-Newton algorithm is shown for two examples: E6 during MSM74 (**Figure 13**) and E12 during MSM40 (**Figure 14**). The eddy centre was determined as described in **Chapter 2.3.1** by iteratively excluding velocity samples from the outer ring towards the inner core and taking the mean of all eddy center estimates. The standard deviation for the eddy centre location with respect to a fixed point for E6 is 410 m in eastward direction and 80 m in northward direction (**Figure**
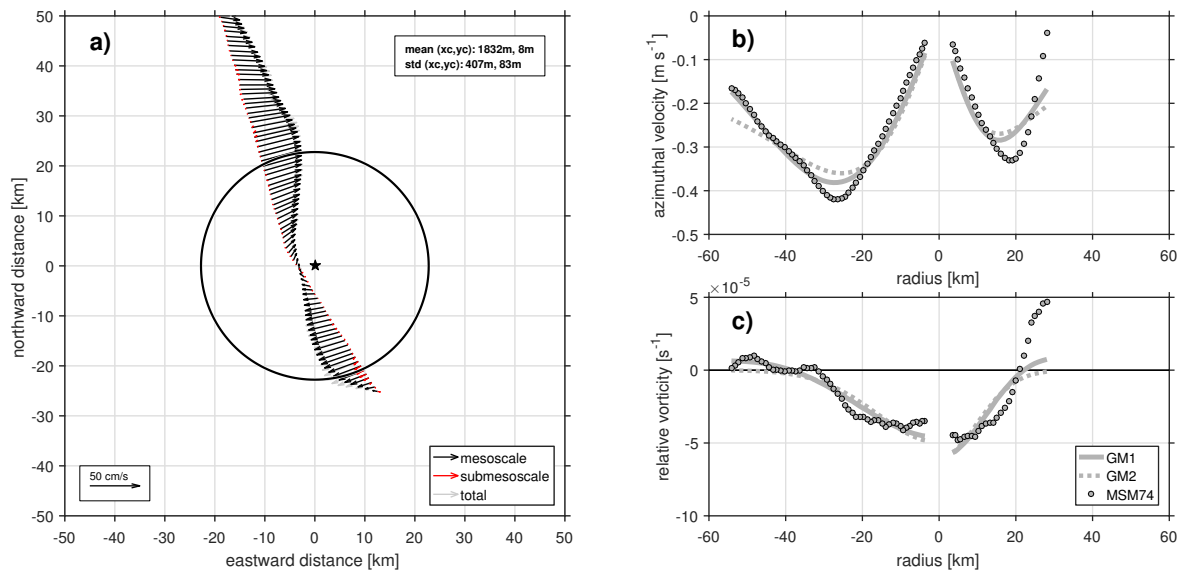

Figure 13: Gauss-Newton algorithm applied to E6 in section4 surveyed during MSM74 showing a) the estimated eddy center (black star) including the speed-based radius (black circle). The black, red, and gray velocity vectors represent the mesoscale, submesoscale, and total velocity component respectively. The calculated eddy centre serves as the origin of the cartesian coordinate system. Additionally, the structure of the b) azimuthal velocity and c) relative vorticity is shown for both inner and outer ring including the Gaussian models GM1 (solid) and GM2 (dotted) fitted to the observations (filled circles).
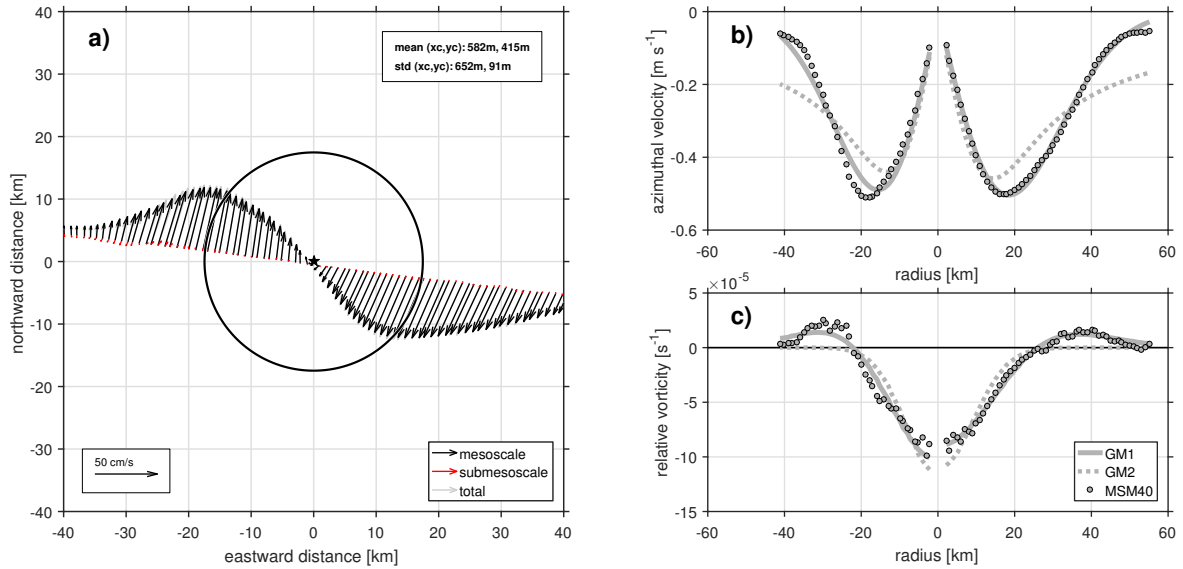
Figure 14: Same than **Figure 13** but for E12 in section 7 surveyed during MSM40.

13a). Elevated submesoscale velocities are found at the southern flank of the eddy. Based on the radial structure of azimuthal velocity (**Figure 13b**) and relative vorticity (**Figure 13c**), the eddy underlies radial asymmetry. The azimuthal velocities at the maximum radius differ by approximately $10\,\mathrm{cm\,s^{-1}}$. Additionally, the southern flank outer ring velocity decays more rapidly suggesting an elevated vorticity shield compared to the northern flank. Relative vorticity within the core region is about $-4 \cdot 10^{-5}\,\mathrm{s^{-1}}$ peaking to $4 \cdot 10^{-5}\,\mathrm{s^{-1}}$ in the outer ring emphasising the large horizontal gradient of relative vorticity at the eddy edge.

The standard deviation for the eddy centre determination of eddy E12 surveyed during MSM40 along section 7 is $650\,\mathrm{m}$ and $90\,\mathrm{m}$ in eastward and northward direction, respectively. In contrast to E6, eddy E12 is of more axisymmetric shape characterised by similar radii and outer ring decay scales (**Figure 14a**). Moreover, structure and magnitude of azimuthal velocity and relative vorticity are similar west and east of the determined eddy centre. Featuring a core relative vorticity of $-9 \cdot 10^{-5}\,\mathrm{s^{-1}}$, the vorticity outside the eddy is only weakly opposed compared to eddy E6.

There are numerous studies that investigated the radial eddy structure of vortices on a broad range of scales from just a few centimetres (Meuel et al., 2013), a few tens of metres (Kanak, 2005) to planetary scales (Chelton et al., 2007, 2011) testing several different theoretical vortex models. Mesoscale eddies have been mostly studied using satellite altimetry. Most of these studies either suggest an exponential (Zhang et al., 2013; Yang et al., 2019) or a Gaussian eddy shape (Chelton et al., 2011; Wang et al., 2015). In order to assess the radial eddy structure of the eddies obtained from the observations and extracted from NATL60, two different Gaussian model fits were performed to the radial velocity. The first Gaussian model (denoted GM1) is described by $v_\theta = c_1 r \exp(-c_2 r^2)$ where c_1 and c_2 are the fitting parameters (Yang et al., 2019).

The second Gaussian model (denoted GM2) was adapted from Meuel et al. (2013) postulating an azimuthal velocity profile of the form $v_\theta = d_1/(2\pi r)(1 - \exp(-r^2/4d_2^2))$ where d_1 and d_2 are the characteristic scales for rotational speed and length, respectively. In both cases, the corresponding relative vorticity was computed by $\zeta = v_\theta/r + \partial v_\theta/\partial r$. Considering the inner and outer ring structure, the GM1 model in **Figure 13b,c** seems to be more appropriate than the GM2 model. Nonetheless, the GM1 model underestimates the maximum azimuthal velocity at the maximum radius. The same applies to GM2. A better fit is achieved for eddy E12 in **Figure 14b,c**. The radial azimuthal velocity and relative vorticity profiles are well described by GM1 for the two radial sections in the inner and outer ring. The GM2 model appears to fail the proper the eddy shape reconstruction. Yet, it will be shown to have its justification in representing the radial eddy shape in the next chapter.

3.4 Observational vs model eddy characteristics

Eddy characteristics as derived from the observed horizontal velocity data are in the following compared with eddies modeled in NATL60. A total number of 33 eddies (27 anticyclones and 6 cyclones) were extracted from the instantaneous model data on June 15 and August 15. The eddies considered in this study were extracted from the domain spanning the area 55°-61°N and 48°-57°W that mostly covers the area of observed eddies sampled during both research expeditions. Eddies of different sizes, shapes, and magnitudes were chosen with the objective to have a varying range of characteristics. In contrast to the observations, the eddy sections are always located close to their respective centre. Eddy characteristics for each individual eddy are listed in **Table B1** in the **Appendix B**. The mean for all considered model eddies are also listed in **Table 3**. The mean radius of the analysed eddies was found to be 15 km ranging between 6 km and 26 km. azimuthal velocities were computed to be in the range 16–89 cm s^{-1} with a mean of 42 cm s^{-1}. The mean outer ring decay scale λ is 21 km. It varies between 6 km and 63 km, though. The maximum sea surface height signal η_0 is as low as 2 cm and as high as 40 cm and features a mean of 16 cm. The model mean inner core relative vorticity ζ_{in} and the mean Rossby number of the gradient flow Ro are $5.5 \cdot 10^{-5}$ s^{-1} and 0.22. The theoretical maximum azimuthal velocity for solid-body rotation V_{sb} is 57 cm s^{-1} and thus on average 25 % higher than the actual maximum azimuthal velocity. The comparison between the observation-based and model mean eddy characteristics give rise to the following discrepancies. The model mean radius was found be 1/4 lower while the maximum azimuthal velocity is roughly 1/5 higher. In particular, the model is characterised by a broader range of maximum azimuthal velocities in contrast to the observations. Consequently, inner core relative vorticity in addition to the Rossby number are roughly 25 % higher implying increased nonlinearity in the model. There is relatively good agreement for the outer ring decay scale, maximum sea surface height,

Table 3: Same as Table 2 but for NATL60 eddies. The complete table is found in **Table B1**.

	R_{max} [km]	V_{max} [cm/s]	λ [km]	η_0 [cm]	ζ_{in} 10^{-5} [s^{-1}]	Ro	V_{sb} [cm s^{-1}]
NATL60							
Mean	15.0 ± 5.5	41.7 ± 20.7	20.7 ± 12.3	15.6 ± 9.0	5.5 ± 1.8	0.22 ± 0.07	56.7 ± 25.8

and theoretical maximum azimuthal velocity whose averages lie within $5\,\%$, $8\,\%$, and $2\,\%$ of the observations, respectively.

Similar to the observations, two exemplary eddies were chosen to illustrate the radial eddy shape. Eddy E21 (**Figure 15a,b**) is characterised by maximum azimuthal velocties and radii that radially deviate from each other by roughly $15\,\mathrm{cm\,s^{-1}}$ and $5\,\mathrm{km}$. The relative vorticity profile closely resembles the one in **Figure 14c**. The GM1 model almost perfectly coincides with the radial azimuthal velocity and relative vorticity in the inner and outer ring. Also, it nicely simulates the maximum radius and azimuthal velocity. On the contrary, the GM2 model is not able to fit the precipitous outer ring velocity. Moreover, it moves the eddy radius by several kilometres towards the eddy centre. The radial eddy shape in **Figure 15c,d** highlights that the horizontal velocity and relative vorticity structure may also be described by the GM2 model which was found non-satisfying for the examples in the observations. The flattening velocity in the outer ring is well captured, whereas the GM1 model does not seem very representative.
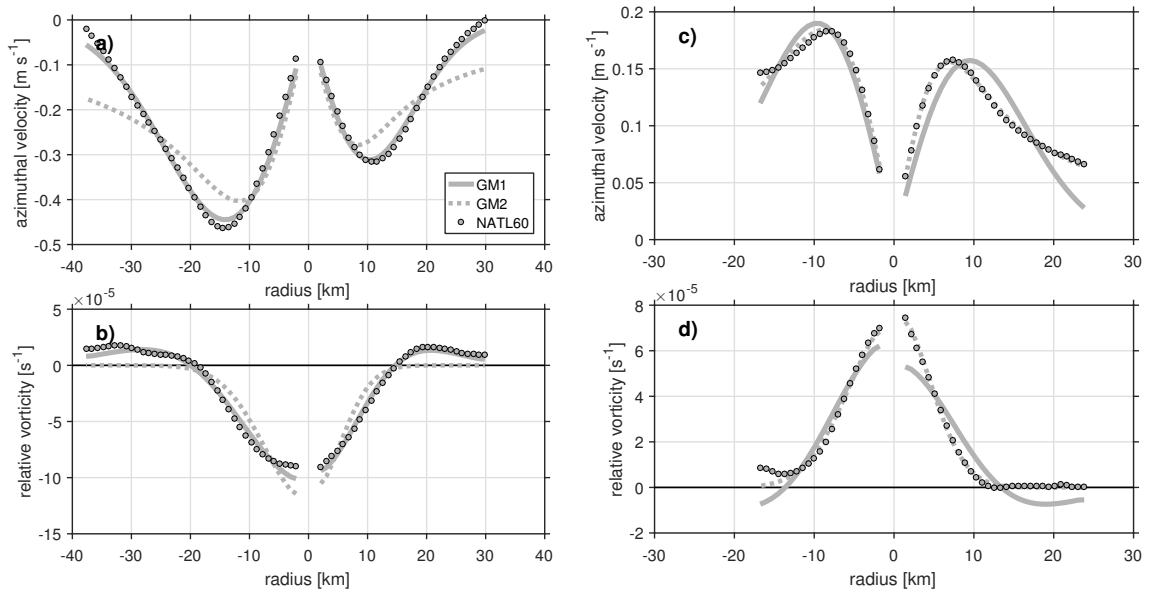

Figure 15: Radial azimuthal velocity and relative vorticity structure for two examplary NATL60 model eddies a,b) E21 and c,d) E32 (filled circles). Two Gaussian models were fitted to the subsampled NATL60 data and are visualised by the solid (GM1) and dotted gray line (GM2).

By comparison with the other examplary model eddy, it does not feature opposing vorticity beyond the eddy edge suggesting a non-existing or weakly pronounced outer ring vorticity shield.

Surely, these four examples are not supposed to be representative of the whole eddy field. Rather, the objective is to point out that the detected eddies are not subject to one specifically defined radial structure. Moreover, it emphasises the importance in studying the dynamics that form the radial eddy shapes. Apart from this, the GM1 with a $\exp(-r^2)$ dependency for the outer ring proved to be the most frequent fit. Of 33 eddies that were extracted from NATL60, 22 eddies were well approximated by the GM1 model, while only 4 eddies turned out to be of the second Gaussian shape type. Interestingly, for three eddies a combination of both models suited best meaning that one radial section was best represented by GM1 and the other by GM2. Also, for three eddies none of the above models applied. A polynomial fit (not shown here) was also conducted in addition to the exponential and Gaussian fit. For all eddies, the radial structure was best represented using a 4th degree polynomial implying an overall quartic strucutre which was also suggested by Kloosterziel and Van Heijst (1991).

The observational and model azimuthal velocity structure for both the inner and outer ring in the framework of an idealised vortex is investigated in detail in **Figure 16**. Eddies surveyed during the research expeditions were only considered in this analysis if they had been crossed through or in the vicinity of the centre. All other eddies did not provide a sufficient inner core velocity structure and were hence neglected. Upper 300 m mean azimuthal velocities were used and normalised by the maximum azimuthal velocity that the eddy would theoretically have if it were in solid-body rotation. The theoretical maximum azimuthal velocity V_{sb}, in turn, is determined by applying a linear fit to the inner core velocity and extracting the fitted velocity at R_{max}. All velocities are given as their magnitude. Radial velocity sections from the observations are provided by E1, E6, and E12. Even though E9 was hit near its center according to the Gauss-Newton optimisation, a linear fit could not be applied to the inner core velocity. It showed large deviations from solid-body rotation and was thus excluded as well.

In addition, the inner and outer velocity structure of an idealised vortex as defined in **Chapter 2.4** is shown. For the outer ring, the mean decay scale from the model eddies was used. All of the eddies feature maximum azimuthal velocities that are lower than the theoretical solid-body rotation velocity. The model maximum azimuthal velocity may be lower than its respective theoretical velocity for solid-body rotation by 10–50 %. Observational maximum azimuthal velocities are by 10–35 % lower than their respective maximum solid-body rotation velocity. Considering the eddy inner ring velocity in **Figure 16a**, both model and observations indicate solid-body rotation for the inner half to two thirds of the eddy inner core, i.e. the azimuthal velocity is proportional to the radius. The second half or last third of the radius is then characterised by a
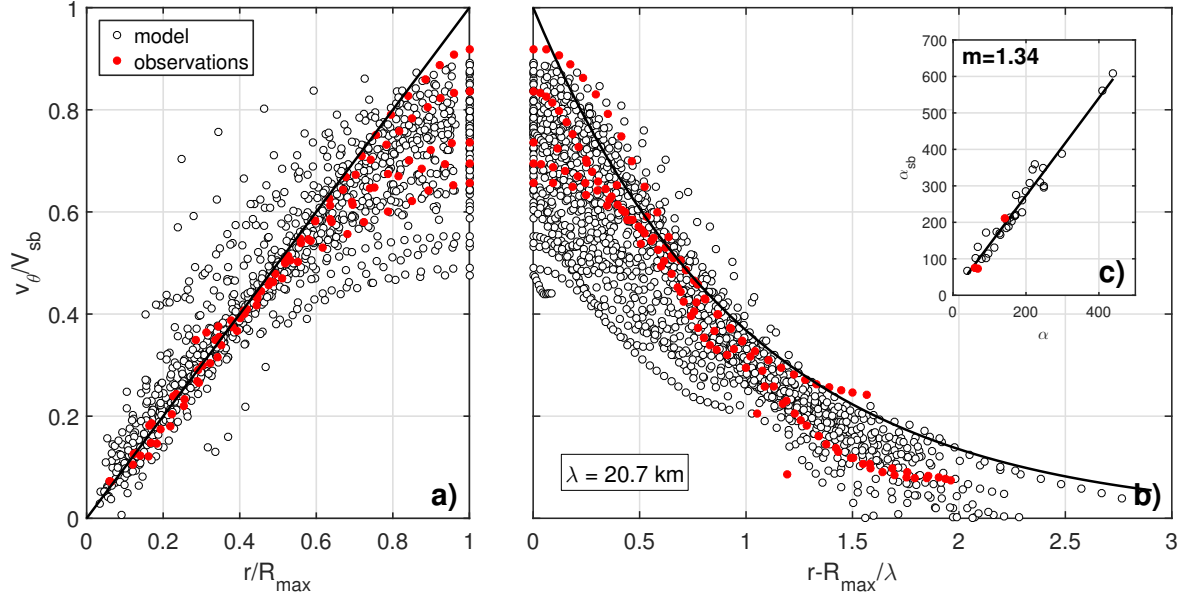
Figure 16: Upper $300\,\mathrm{m}$ mean azimuthal velocity structure for the a) inner ring ($r < R_{max}$) and b) outer ring ($r > R_{max}$) normalised by the theoretical solid-body rotation velocity V_{sb}. Velocity structure is shown for the NATL60 model (black circles) and for the observations (red circles) from MSM74 and MSM40. Observational eddy sections are from E1,E6, and E12. All other eddies were either not crossed through/near their centre or do not provide a sufficient inner core velocity structure and were therefore not considered in this analysis. The thick black lines in a) and b) represent the radial velocity structure for an idealised vortex as defined in **Equation 25**. For the outer ring, the model mean decay scale was used ($\lambda = 20.7\,km$) . In addition, (c) the nonlineary parameter α is plotted against α_{sb}, the theoretical nonlinearity parameter for solid-body rotation.

velocity structure that follows a more Gaussian-like shape. Otherwise, **Figure 16c** illustrates that the outer ring velocity structure can to a large amount be explained by an exponential decay with varying decay rates. The largest deviations are, however, again found at the maximum radius. A nonlinearity parameter adapted from quasi-geostrophy theory was computed for the both the in-situ azimuthal velocity and the theoretical azimuthal velocity for solid-body rotation at R_{max} and plotted against each other in **Figure 16c**. The slope of the applied linear fit is 1.34 suggesting the eddies in observations and model to be about one third less nonlinear than they would be for solid-body rotation. The significance of the observational data is, however, rather limited since only a small amount of eddies were properly surveyed. Therefore, it is not representative for the whole eddy field and should be regarded as a case study.

It turns out that in most cases the idealised vortex structure associated with solid-body rotation in the inner core ($r < R_{max}$) and exponential decay in the outer ring ($r > R_{max}$) is not applicable to the radial velocity structure. Instead, the Gaussian-shaped azimuthal velocity structure according to Yang et al. (2019) has proved more advantageous. While correlating several eddy defining characteristics, a good linear relationship with the Gauss-Newton derived maximum sea surface height signal η_0 and

maximum radius R_{max} as well as maximum azimuthal velocity V_{max}, significant at the 99 % confidence level, was found as shown in **Figure 17a,b**. Hence, the larger the sea surface height signal (also referred to as amplitude), the larger is the radius and the rotation speed. Further, it was addressed how the sea surface height is linked to the radial eddy shape. In particular, the fitting parameters c_1 and c_2 were described as a function of the eddy amplitude (inset in **Figure 17c**) according to Yang et al. (2019) where $\bar{c}_1 = -0.086\eta_0 + 1.21$ and $\bar{c}_2 = 0.262\eta_0 + 0.474$. The resulting normalised velocity structure derived from the eddy amplitude is then $V' = \bar{c}_1 r' exp(-\bar{c}_2 r'^2)$ where V' and r' are the normalised azimuthal velocity and radius, respectively. **Figure 17c** shows the same horizontal velocity structure than **Figure 16** but is normalised by the maximum radius R_{max} for the outer ring as well. The black line represents the average eddy shape of radial azimuthal velocity for NATL60 and for $\eta_0 = 15.6\,\mathrm{cm\,s^{-1}}$. Thus, on average the model eddies feature a Gaussian shape as suggested by Yang et al. (2019). This kind of vortex is termed Taylor vortex and is believed to represent the most common type for oceanic mesoscale eddies (Wang et al., 2015). A model fit to the observations was not performed due to a lack of sufficient data. Anyway, the available data points are plotted in **Figure 17** as red circles and in the inset of **Figure 17c** as triangles. Possible mechanims that potentially drive the radial shape will be discussed in the follwing.

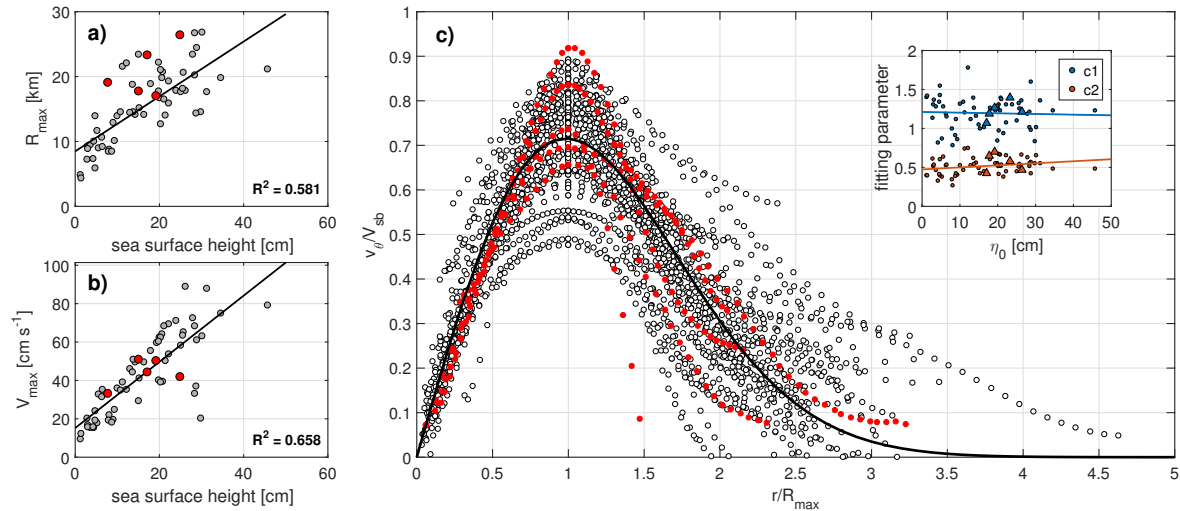Recent literature has emphasised that the reconstruction of eddy shapes is not an

Figure 17: Linear relationship between the NATL60 surface height η_0 and a) maximum radius R_{max} and b) maximum azimuthal velocity V_{max} (filled gray circles). The filled red circles represent the observations for E1, E6, and E12. c) Radial azimuthal velocity as a function of radius normalised by the solid-body rotation velocity V_{sb} and R_{max}, respectively. The thick black line is the average NATL60 eddy shape for $\eta_0 = 15.6\,\mathrm{cm\,s^{-1}}$ as determined by the linear regression of the fitting parameters c_1 and c_2 to η_0 in the inset. The filled red circles represent the observational azimuthal velocity structure. The colored triangles in the inset are also taken from observations.

obvious task. Yang et al. (2019) found that the eddy shape can be described as a function of the eddy amplitude and hence as function of the eddy's life cycle. They achieved to develop a Taylor vortex model that derives the radial shape during eddy growth and decay based on the associated amplitude dependence. The varying shape is induced by shedding and entrainment of fluid at the eddy boundary that ultimately impacts the radial eddy structures. The theory for this is given by Early et al. (2011) and is based on potential vorticity conservation. They studied the evolution and propagation of nonlinear quasigeostrophic mesoscale eddies und investigated the requirements for particles to remain on the contour of zero relative vorticity, i.e. contours of $\nabla^2\eta$. In order to flow tangential to the $\nabla^2\eta$ contour, the particle must conserve its potential vorticity such as

$$\frac{d}{dt}\left[\beta_0 y + \frac{g}{f_0}\nabla^2\eta - \frac{f_0}{D}\eta\right] = 0 \tag{40}$$

where D is the column height. The left, middle, and right term represent the planetary vorticity, relative vorticity, and vortex stretching contribution to potential vorticity, respectively. For a particle that circulates around the eddy core, the changing planetary vorticity contribution is compensated by the height of the zero relative vorticity contour. In addition, the eddy develops a meridional speed during westward propagation which needs to be compensated by the height decay or growth rate. Their simulations revealed that the sea surface height rate of change does not completely account for this compensation. As a result, potential vorticity is not conserved such that the particle increases in relative vorticity and eventually crosses the boundary of zero relative vorticity. Briefly, the outer ring continously sheds and entrains fluid to conserve potential vorticity. Since the eddy core cannot entrain fluid due to the large potential vorticity gradient barrier, it only sheds fluid. Meanwhile, the band of maximum velocity moves towards the centre. Thus, the elevated water exchange at the boundary induced by the varying eddy amplitude may exert a sustained influence on the radial eddy shape.

Another process that is believed to influence the radial structure is vortex stripping, first described by Legras and Dritschel (1993). In their study they investigate the evolution of an isolated vortex subject to a varying range of strain rates induced by the external environment and an associated elongation of the vortex core. For a given critical external strain, an initially circular vortex features stripping of its most external layer due to the penetration of the velocity field. As a consequence, straining or stripping is responsible for the outward advection of vorticity in the external and at later state in the more internal layers in form of escaping filaments producing large vorticity gradients at both the vortex edges and the filaments edges which may be carried to great distances. The authors claim that vortex stripping is the leading process for the generation of high vorticity gradients in geostrophic turbulent flow.

In a more recent study from Zhang and Qiu (2018), the vortex edge is also considered to be largely influenced by the external strain field. In regions with strong background currents and nonlinear eddy-eddy interactions as well as interactions between the mean flow and eddy field, elevated levels of geostrophic strain rates are observed. At the same time, the strength of the geostrophic strain rates is positively correlated with submesoscale ageostrophic kinetic energy levels. This ageostrophic energy in submesoscale dimensions features increased values during both the formation and decay phase and is minimum during the mature phase. The strain rates are maximum around eddy edge and favour the development of submesoscale perturbations which potentially shape the radial eddy structure. At the very least, submesoscale energy levels were found not to be necessarily related to the strength or amplitude of the mesoscale eddy but rather by the background strain field.

Yang et al. (2019) concluded that submesoscale turbulence is of high importance in order to understand the dynamics that shape the eddy edge. A study from Kanak (2005) evaluated the azimuthal velocity structure which is best described by the Burger-Rott model for high-resolution simulations. The model assumes a balance between radial and vertical advection, and diffusion and provided better results than the often used Rankine vortex. Even though the model was applied to small-scale dust devils, it may emphasise the need for the inclusion of submesoscale processes near the eddy edge and the corresponding elevated water exchange in horizontal and vertical direction. Having assessed the horizontal structure of eddies from the observations and high-resolution NATL60 data, the vertical properties and in particular the vertical hydrography are analysed in the next chapter.

3.5 Vertical hydrography properties

During the transit from the central Labrador Sea towards the Greenland Shelf as well back from the shelf westwards to deeper water, a small number of CTD casts were conducted along the ship track in order to capture the physical properties of the vertical hydrography within the eddy field. The positions of the CTD profiles within the sea level anomaly field and the SADCP data are shown in **Figure 11**. In the ideal case, one obtains one CTD cast in the eddy core region and one or two casts outside the core, i.e. in the outer ring or beyond, in order to evaluate the hydrographic properties with respect to the surrounding flow. In practice, this has not been properly achieved during MSM74. The collected vertical profiles along the ship track give an idea of the water mass distribution, though. Assessing both the sea level anomaly field and the along-track horizontal velocity as measured by the SADCP, the following CTD casts are allocated to the individual eddies surveyed during the campaign.

CTD casts #40 and #43 represent the reference profiles in the outer ring of E1, while #41 is situated within the inner ring. CTD casts #43, #44, and #45 are used for

eddy E2 in which #44 represents the inner ring cast. Assigning the CTD casts to eddy E3 has proved difficult. While the sea level anomaly field suggests the CTD casts #46 and #48 to be located in the external environment, vertical profiles of potential temperature, salinity, and potential density imply the opposite stating that only #45 is situated outside the eddy. This issue will be revisited later. CTD casts were also conducted during the east-west transect potentially crossing two eddies (E4 and E5). CTD casts #75 and #76 were concluded to represent the inner ring hydrography while #73 and #74 are outside the ring according to the SADCP data and the Gauss-Newton derived eddy radius. Similar to eddy E3 there are some difficulties in the allocation of the CTD profiles to their location relative to the eddy. The hydrographic properties as well as the mentioned discrepancies are presented in the following. Further, it will be discussed what kind of type the surveyed eddies are.

The three CTD casts that cover the vertical hydrography of the outer and inner ring of eddy E1 show evidence for increased potential temperature and salinity in the eddy core region compared to the surrounding water (**Figure 18a-e**). The warm, salty lens of eddy E1 stretches from the surface to approximately 800 m depth and is characterised by temperatures and salinities of up to 4.1 °C and 34.88 psu as well as maximum anomalies of 0.6 °C and 0.05 psu compared the outer ring.

Eddy E3 (**Figure 18k-o**) also features a lens of warm, saline water that roughly ranges from 50 m and 1000 m with maximum potential temperatures and salinities of 4.3 °C and 34.89 psu and is up to 1 °C and 0.08 psu warmer and more saline than the surroundings. In contrast to eddy E1, eddy E3 is overlaid by a cold, fresh cap in the upper 50 m with temperatures and salinities as low as 2.5 °C and 33.78 psu with corresponding anomalies of 0.7 °C and 0.4 psu relative to the outer ring profiles. Eddy E1 features three pycnoclines: two pycnoclines in the upper 500 m between 50 m and 100 m and between 250 m and 500 m as well as a deep pycnocline below 2500 m assumingly the eddy base. The upper pycnocline of eddy E3 is located in the upper 500 m, whereas the deep pycnocline is found above 2000 m. Interestingly, the deep pycnocline tends to be vertically displaced by a few 100 m within the inner ring.

The analysis of the CTD profiles covering the influence area of E3 expresses uncertainty considering the eddy reconstruction using the Gauss-Newton method. In detail, the hydrographic profiles indicate that the CTD casts #46 and #48 are located rather in the inner ring instead outside of it as suggested by the gridded sea level anomaly field. The wrong representation of the eddy extent and possibly erroneous eddy centre estimate could have arisen from the complex horizontal velocity along the ship track in section 2 around 400 km distance (**Figure 9**). At 400 km the zonal velocity is close to zero (indicative of the eddy centre) increasing towards the north (>400 km) before reducing well below 5–10 cm s^{-1} in the upper 400 m. A closer look at the submesoscale velocity field in **Figure A2** and **Figure A4** reveals an anomalous velocity signal characterised by opposing velocities around 440 km. It stretches from the near-surface to 300 m depth
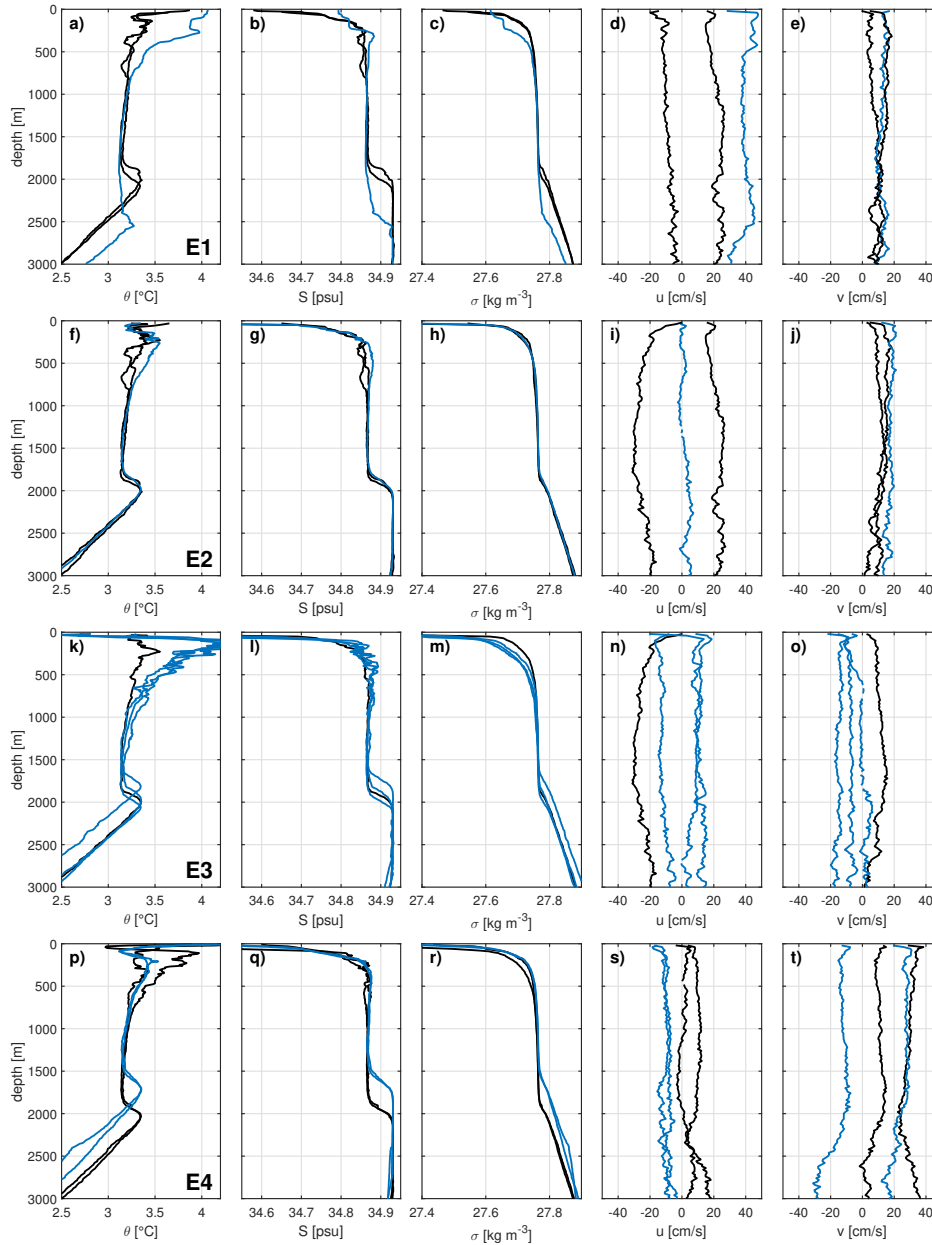
Figure 18: Vertical profiles of potential temperature θ, salinity, potential density anomaly σ_0, zonal and meridional current velocity of E1 (a-e), E2 (f-j), E3 (k-o), and E4 (p-t). The blue lines represent an CTD cast whithin the core or inner ring region, whereas the black lines are reference casts in the outer ring region or beyond.

and counteracts the mesoscale velocity field. Ultimately, it is likely that the presence of these superimposed submesoscale velocities mistakenly distorted the velocity field along the ship track in such way that the local maximum of azimuthal velocity was interpreted as the global maximum. If so, the northward eddy extent is underestimated. Whether the anomalous velocity has its origin in ageostrophic effects or in a submesoscale eddy that is located in the inner ring of the larger-scale vortex, is not evaluated at this point. Both eddies (E1 and E3) are believed to be of IR type characterised by warm, salty lenses of water. The eddies detected here mainly differ by the near surface properties.

The fresh, cold cap of eddy E3 is a common feature of IR. Its origin is the fresh, cold West Greenland Current along Cape Desolation, the main formation site of IR. The cold, fresh cap of water is not present for E1. Most probably, this structure occurs for IR that detach from the boundary current, i.e. from the Irminger current, without extracting the cold, fresh water properties of the WGC.

E2 is of similar type than E3 as a warm, saline dome of water is overlaid by a fresh, cold cap. The warm, saline dome stretches from 250 m to 800 m with maximum values of 3.55 °C and 34.88 psu. Maximum temperature and salinity anomalies lie in the range of 0.3 °C and 0.04 psu compared to the surrounding water. E2 also extends to $1700 - 1800$ m. Assessing the temporal evolution of the gridded sea level anomaly maps (not shown here) reveals that eddy E2 was surveyed twice: first during the meridional transect on June 6 (E2) and second during the westward transect on June 13 (E4). Therefore, the hydrographic properties should be more or less the same. However, the CTD casts #75 and #76 that are believed to be in the inner ring of eddy E4 indicate no clear anomaly in temperature and salinity compared to the sourrounding water. There is some evidence for an anomously warm, salty water volume around 250 m depth with respect to the reference cast #73 (the most outer/eastward CTD cast on section 3). CTD cast #74, located just outside the eddy rim (southeastern flank), is misleading though since it features a positive temperature and salinity anomaly proposing colder and slightly fresher conditions. It cannot be exluded that the discrepancies in the hydrography between E2 and E4 are due to slightly different CTD station positions with reference to the eddy centre accompanied with horizontal and vertical deviations in temperature, salinity, etc. Considering the eddy characteristics derived in **Table 2**, eddy E2 and E4 differ from each other. On the one hand, one can assume that the sea level anomaly field is not appropriately represented by the altimetry product. On the other hand, the Gauss-Newton derived speed-based radius may have given questionable results. Taking into account the LADCP profiles in **Figure 18t**, it is reasonable to conclude that the CTD casts #75 and #76 are located within the inner ring near the northwestern and eastern flank of E4, respectively, owing to the opposing signs in meridional current velocities. Similarly, it can be argued that CTD cast #44 of eddy E2 characterised by near zero zonal current velocity and roughly $20 \, \mathrm{cm \, s^{-1}}$ in meridional velocity **Figure 18i,j** is situated with some certainty within the inner ring near the eastern flank.

Two different types of Irminger rings were detected in the CTD observations from MSM74. IR type 1 (denoted IR1) is characterised by a surface trapped warm, salty dome of water, whereas IR type 2 (denoted IR2) features a surface layer of cold, fresh water above the warm, salty core. Two exemplary eddies were extracted from the instantaneous NATL60 data from June 15 that appeared to be of similar type than those observed in the CTD profiles. The extracted eddies are numbered E1 and E3 in **Table B1**. Potential temperature, salinity, meridional current velocity, and relative
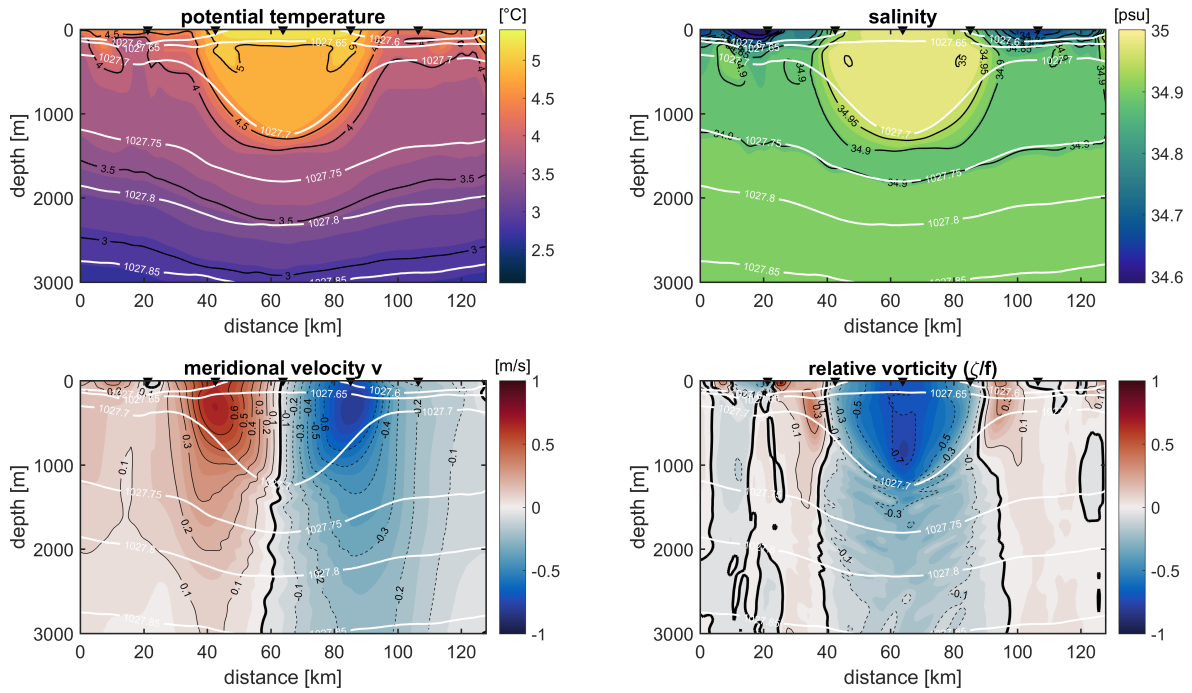
Figure 19: Zonal sections through an model Irminger ring (E1) of first type (IR1) showing a) potential temerature, b) salinity, c) meridional velocity, and d) relative vorticity including contours of potential density (white lines). The black triangles indicate the location where the vertical profile data was extracted.

vorticity normalised by the planetary vorticity are shown in **Figure 19** and **Figure 20** for IR1 and IR2. The overall structure and hydrography compares well with the observations from Lilly et al. (2003); Hátún et al. (2007); de Jong et al. (2014) featuring a clear downward displacement of isopycnals in the upper 1000 m. Similarly, the cold, fresh cap is located in the upper 100–200 m. In slight contrast, by comparison with additional IR of both types in the model data, the velocity structure is not necessarily surface-intensified as it is the case in **Figure 19c**. Of in total 33 eddies that were indentified in the model data from June 15 and August 15 as IR (IR1 and IR2), 10 IR featured intensifed currents away from the surface with maximum velocity magnitudes in the range 100–400 m. Also, the double core structure and bottom-intensified currents as observed by Lilly et al. (2003) and de Jong et al. (2014) could not be detected in NATL60. For both examples shown here, the eddies have strongly negative relative vorticity (< -0.7, E1; < -0.9, E3) in the core region at the eddy base around 900 m depth. They are surrounded by strongly opposite vorticity (> 0.3, E1; > 0.9, E3) exhibiting a large lateral vorticity gradient which is also supported by the horizontal surface relative vorticity field in **Figure 6a**.

Further hydrographic properties are considered in the following. Along the eddy sections in **Figure 19** and **Figure 20**, a small amount of vertical profiles were extracted and individually analysed in **Figure 21**. Primary, the vertical profiles are used to study the horizontal and vertical characteristics of simulated IR. Secondary, the extraction of
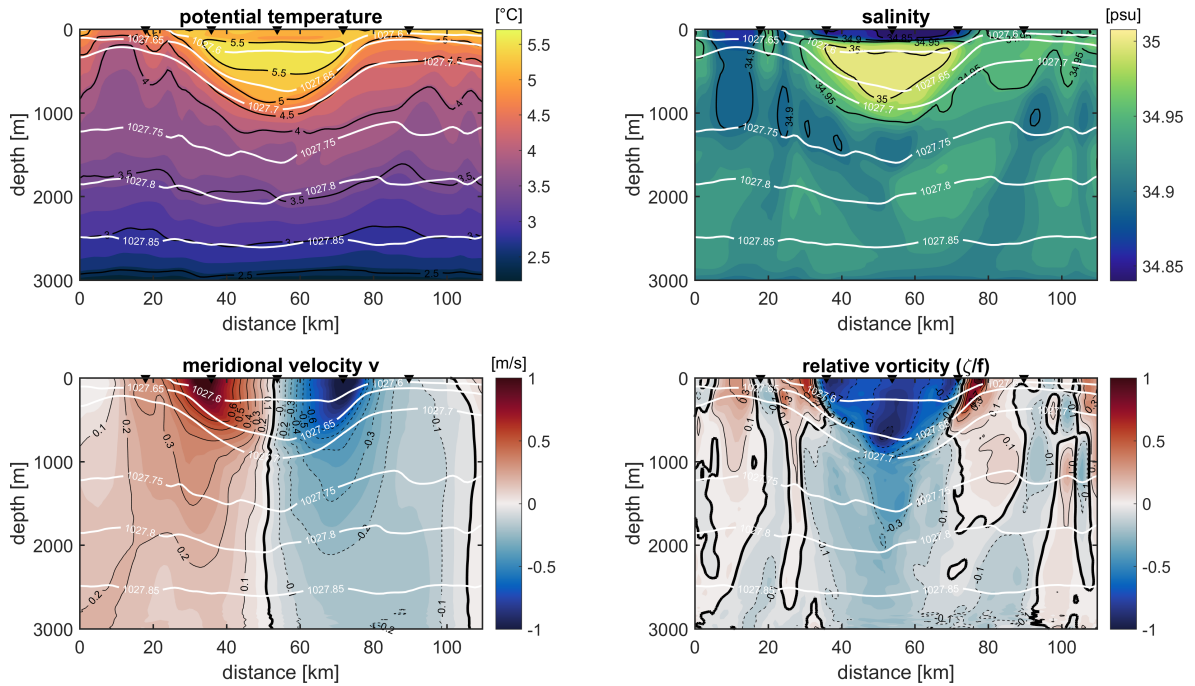
Figure 20: Zonal sections through an model Irminger ring (E3) of second type (IR2) showing (a) potential temerature, (b) salinity, (c) meridional velocity, and (d) relative vorticity including contours of potential density (white lines). The black triangles indicate the location where the vertical profile data was extracted.

discrete vertical profiles serves as a skill assessment of the observational CTD profiles. In detail, the model profiles are used to prove whether a profile within the core and reference casts outside the eddy are sufficient to estimate the anomalies in temperature and salinity that are associated with the eddy with respect to the surroundings. For both eddies in **Figure 21** one cast was chosen to represent the eddy core region (blue line). Two casts were located at the western and eastern flank near the eddy rim which is associated with the velocity maximum (orange lines). The reference casts were extracted several kilometres off the velocity maximum, in the outer ring region (black lines).

Model eddy E1 was identified as IR1. It is characterised by a warm, salty core of water (5 °C, 35 psu) that stretches from the surface to 1500 m with maximum potential temperature and salinity anomalies of 1.3 °C and >0.1 psu at around 750 m depth. The water column of the eddy core is approximately homogeneous from the surface to 1200 m except for the upper 200 m. The region around the velocity maximum, in contrast, is characterised by a constant vertical gradient in temperature and salinity with anomalies of up to 1 °C and 0.1 psu with respect to the eddy core cast implying overall vertical shear. The velocity cores are situated at 350 m exhibiting a baroclinic velocity structure. The vertical profiles show similarities to those shown in **Figure 18a-e**. Differences are noted in zonal and meridional velocity profiles that illustrate velocity fluctuations in the deep pycnocline which are not visible in the observations. Model eddy E3 was identified
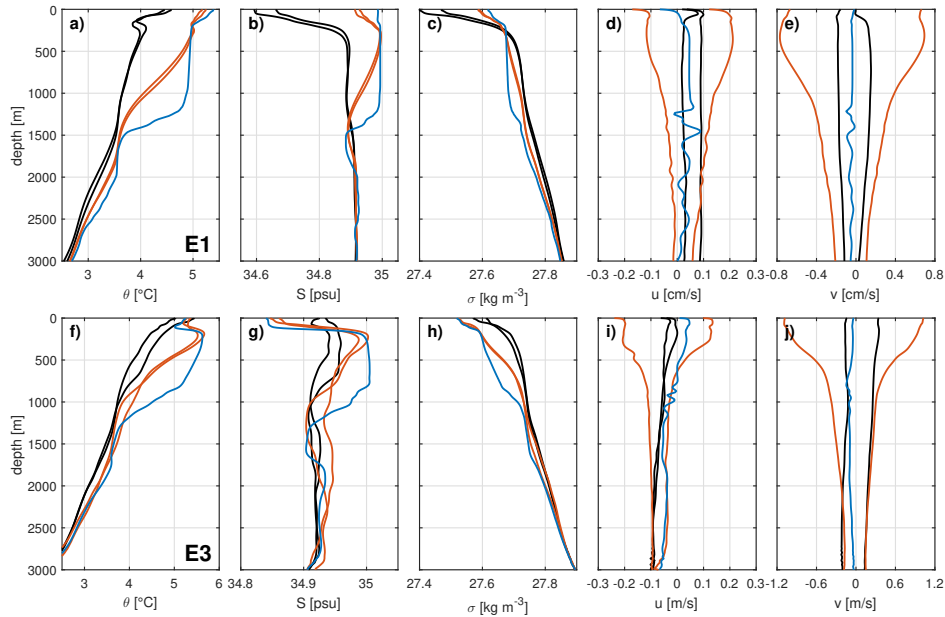
Figure 21: Model vertical profiles of potential temperature θ, salinity, potential density anomaly σ_0, zonal and meridional current velocity of E1 (a-e) and E3 (f-j) extracted from the locations as indicated by the black triangles in **Figure 19** and **Figure 20**. The blue, orange, and black lines represent an CTD cast whithin the core region, near the eddy rim, and in the outer ring region (or beyond) respectively.

as IR2 featuring a cold, fresh cap overlying a warm, salty lens of water. The warm, salty dome ranges from 200 m to 1300 m. Maximum temperature and salinity anomalies in that depth range are 1.5 °C and 0.1 psu. At the surface, temperatures are comparable with the surrounding water, whereas the salinity values are roughly 0.1 psu fresher. The zonal and meridional velocity fluctuations are also seen in the deep pycnocline. Model eddy E3 is best comparable with the observed eddies in **Figure 18f-j** and **Figure 18k-o**. A consistent feature that differs the model from the observations is that the base of the warm, salty water volume coincides with the deep pycnocline. On the contrary, the deep pycnocline of the observational profiles is located deeper within water column well below the anomously warm, salty water.

3.6 Gauss-Newton methodology assessment

The Gauss-Newton algorithm applied to the observational SADCP data has shown to provide an alternative method to detect and characterise the local eddy field using a single track of velocity data. In the following, the reliability of the Gauss-Newton algorithm is discussed making use of the three-dimensional NATL60 velocity field. The individual eddy centre determination of the along-track velocity data in MSM74 and MSM40 is based on only one section which may be through or near the actual eddy centre. However, some of the sections are rather in greater distance to the centre, i.e. they are near the rim. The high-resolution velocity field of the NATL60 model

provides a reference data set which in turn allows for a skill assessment of the eddy field reconstruction by applying the Gauss-Newton algorithm to the subsampled NATL60 model velocities along artifical cruise tracks. These cruise tracks were chosen such that they cross the eddy diagonally from the northwestern to the southeastern as well as from the southwestern to the northeastern flank. The velocity tracks averaged over the upper 300 m were extracted for two exemplary eddies (denoted GN1 and GN2) from the instantaneous velocity field on May 1. The corresponding 2-dimensional horizontal velocity and relative vorticity field for both eddies are shown in **Figure 22a,c)**. The enclosed contour line of zero relative vorticity here defines the reference eddy extent or radius. The reference eddy centre is denoted by the red star and is defined by the minimum absolute velocity. Considering all sections the mean distance to the reference
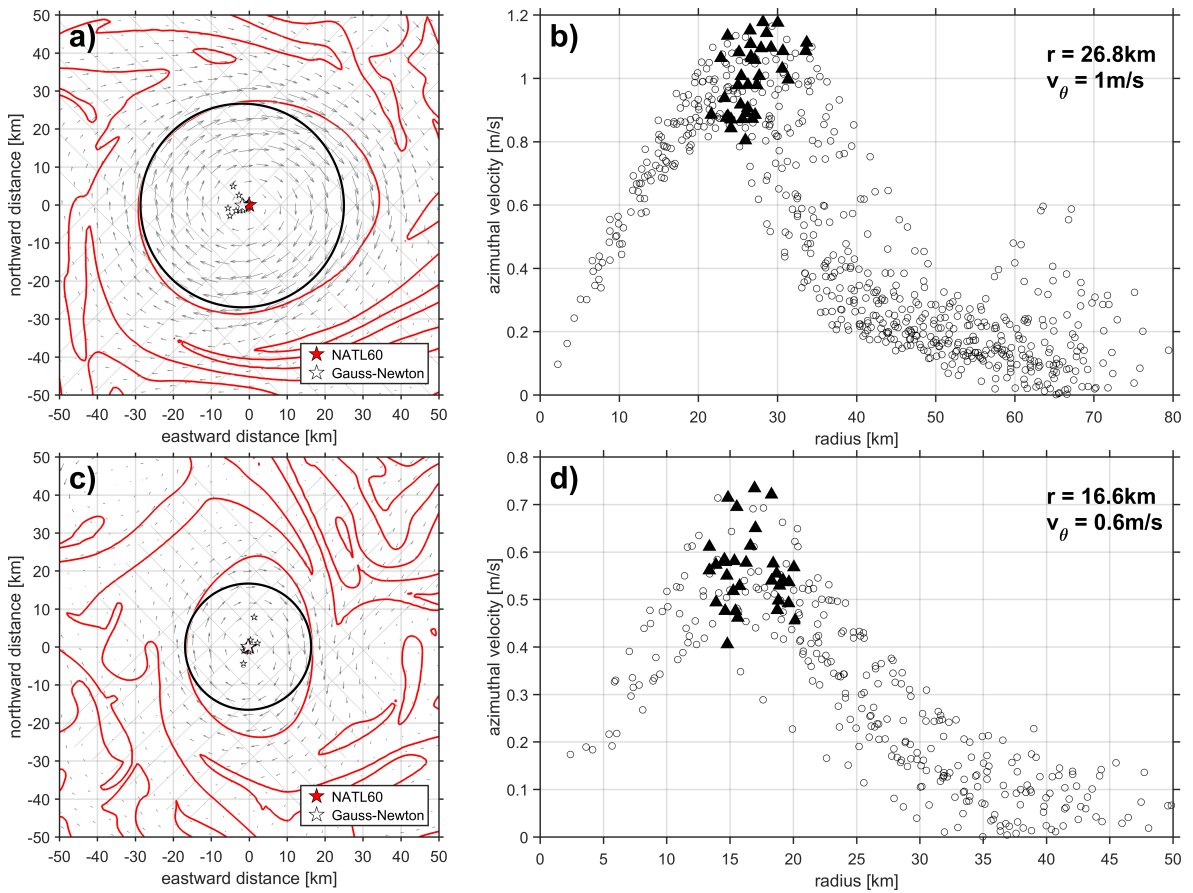

Figure 22: Gauss-Newton algorithm applied to two exemplary eddies (denoted GN1 and GN2) in NATL60 extracted from the instanteneous velocity field on May 1st showing a,c) contours of zero relative vorticity (red contours) as well as the Gauss-Newton derived eddy centre (red star) including the horizontal velocity field (gray arrows) and b,d) the radial azimuthal velocity structure for all sections. The big white star in a,c) represent the Gauss-Newton derived mean eddy centre taking into account all artifical ship tracks. The small white stars are the estimated eddy centres for each individual section. The light gray diagonal lines in the background visualise the sections with the subsampled horizontal velocities. The sections diagonally cross the eddies from the northwestern to the southwestern flank and from the southwestern to the northeastern flank. The black triangles in b,d) mark the maximum azimuthal velocity for each radial section and the corresponding speed-based eddy radius.

Table 4: Skill assessment of the Gauss-Newton eddy reconstruction methodology listing the percentage difference (%) of eddy characteristics among all ship tracks crossing the eddy with respect to the associated mean value for R_{max}, V_{max}, λ, η_0, ζ_{in}, and Ro for GN1 and GN2.

	R_{max}	V_{max}	λ	η_0	ζ_{in}	Ro
GN1	7.9	9.3	19.2	11.0	8.7	5.5
GN2	11.4	10.8	15.1	10.6	16.8	10.5

eddy centre in **Figure 22a** is 2.3 ± 2.0 km. Eddy center estimates are best for sections that lie near the model eddy centre (1.1 ± 0.4 km) and worse for sections that are located near the eddy rim (5.0 ± 2.0 km). The mean distance for sections between the core and the rim is 1.9 ± 1.4 km. The same pattern is seen for the second example in **Figure 22c**. The mean distance to the reference eddy centre is 1.7 ± 2.0 km. The mean distance for sections near the center is 0.8 ± 0.1 km increasing to 1.0 ± 0.7 km for sections between the core and the rim, and 4.0 ± 3.0 km near the rim. Apart from the increasing mean distance for sections located towards the rim, the spread of eddy centre estimates and therefore the corresponding uncertainty of the Gauss-Newton algorithm rises as well. The speed-based estimated eddy extent as derived by the optimisation overlaid by the enclosed contour of zero relative vorticity clearly indicates the asymmetry of the selected eddies of which the second eddy (**Figure 22c**) is of more elliptical shape than the first (**Figure 22a**).

Splitting the artifical cruise tracks in each case in two radial sections and assuming that the radius can be estimated by the distance between the eddy centre estimate and the maximum azimuthal velocity, one obtains a variety of radius estimates as shown in **Figure 18b,d**. The mean radius is estimated to be 26.8 ± 2.8 km with an average maximum azimuthal velocity of $1.00 \pm 0.11 \, \mathrm{m \, s^{-1}}$ for the more circular eddy and 16.6 ± 2.1 km and $0.56 \pm 0.08 \, \mathrm{m \, s^{-1}}$ for the more elliptical-shaped eddy. For obvious reasons the Gauss-Newton algorithm is not capable of reproducing the eddy shape since it assumes a perfectly axisymmetric ring. Nonetheless, it gives satisfying results considering the eddy centre and the derived radius determination. **Table 4** lists the percentage difference of the eddy characteristics among all ship tracks crossing the eddy with respect to the associated mean value for radius, azimuthal velocity, outer ring decay scale, sea surface height signal, relative vorticity, and Rossby number for GN1 and GN2. The percentage difference defines how well the individual Gauss-Newton derived characteristics agree with each other, i.e. it gives a measure for the spread of the values with respect to the mean value. For the derived variables radius, azimuthal velocity, sea surface height signal, and Rossby number it is found the that eddy reconstruction reproduces the eddy characteristics in most cases within $10\,\%$. Outer ring decay scale

and inner core relative vorticity feature slightly higher deviations but remain below 20 %.

Even though most of the eddy characteristics lie within 10 % with respect to the mean value, the method does suffer from the location of the ship track. The closer the ship track is to the actual eddy centre, the more trustworthy is the estimated eddy centre and the eddy centre derived variables. Ship tracks close to the eddy rim need to be used with caution, especially when the track lies outside the velocity maximum. In that case, the Gauss Newton method cannot reconstruct the eddy characteristics. The Gauss-Newton methodology is accompanied with some additional drawbacks apart from the assumption of a circular axisymmetric, non-translating vortex which are evaluated now. The implementation of the Gauss-Newton method is associated with a compromise in terms of convergence of the objective funtion. While it usually just takes a couple of iteration steps for the objective function to converge (quadratic convergence), it is not guaranteed that the global minimum is found. Moverover, the final estimate strongly depends on the intial conditions. For this reason, a cluster of different start values as well the Armijo rule were introduced to the algorithm that attempt to ensure that the intitial guesses are in a suitable range and that the iteration step lengths are not too large. Ideally, the goal is to enforce global convergence. Despite all, once the Gauss-Newton method is attracted by a local minimum, it will stick to it and is considered as the global minimum (even though it is not). In that case, the objective function has only converged locally and is restricted to the local minimum. Besides, the probability that the optimisation converges to a local minimum increases with growing amount of parameters that are aimed to be optimised. This explains why the optimisation for both eddy centre and eddy translation did not provide robust results.

3.7 Mesoscale and submesoscale velocity field representation

The characteristics of sampled eddies in the central Labrador Sea were explicitly analysed and compared with mesoscale features in the high-resolution submesoscale permitting NATL60 model. In particular, it was shown that discrepancies exist in terms of radius and azimuthal velocities. The high-resolution data of horizontal velocities obtained during MSM74 and MSM40 provide information about the velocity fluctuations in spatial domains. In total, the research expeditions conducted an almost 2000 km long high-resolution survey of horizontal velocities in the eddy-enriched central Labrador Sea off the coast of West Greenland. In the following, the mesoscale and especially the submesoscale velocity field representation of the NATL60 model is presented by taking the observational data from MSM74 and MSM40 as reference.

The power spectral density of the horizontal velocity field $(u^2 + v^2)^{1/2}$ as a function of the wavenumber k (spatial frequency) given in cycles per kilometre (cpkm) for two different layers (0–50 m and 350–400 m) and for both expeditions is illustrated in **Figure 23**.

If applicable, the power spectral density from both instruments, 38 kHz, 75 kHz for MSM74 and 38 kHz, 150 kHz for MSM40 is computed.

There is no 38 kHz SADCP data in the upper 0–50 m during MSM74 since the first available bin is deeper than 50 m. Similarly, data for the 150 kHz SADCP during MSM40 does not exit because its vertical range limit lies around 300 m. Also note that the 75 kHz device during MSM74 starts measuring at 17.5 m. For MSM40 data is available from 34 m and 16 m for the 38 kHz and 150 kHz instrument, respectively.

Overall, the power spectral densities for the 38 kHz, 75 kHz measurements during MSM74 and for the 38 kHz, 150 kHz measurements during MSM40 agree with each other. Opposing the two observational datasets, it can be seen that the observed spectra are of similar magnitude in the mesoscale range $\mathcal{O}(100\,\mathrm{km})$, both near the surface and in the pycnocline. However, seasonal differences are visible between June and August in the submesoscale range $\mathcal{O}10\,\mathrm{km})$ and below, where the MSM40 spectra is by one order
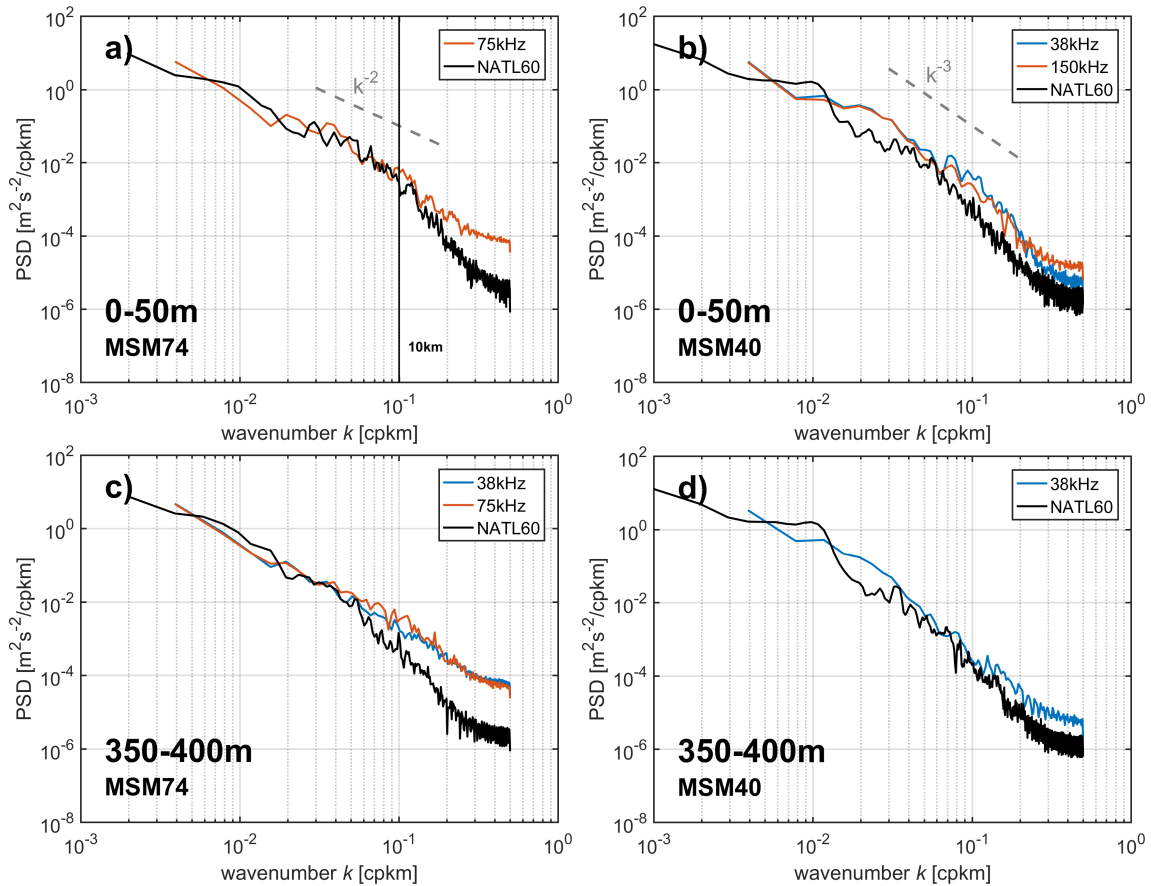

Figure 23: Power spectral density as a function of wavenumber k of horizontal velocity $(u^2 + v^2)^{1/2}$ as measured by the a,c) 38 kHz and 75 kHz ADCP instruments during MSM74 in June 2018 and b,d) 38 kHz and 150 kHz instruments during MSM40 in August 2014 for the near surface 0–50 m (upper panels) and pycnocline 350–400 m (lower panels). The power spectral density obtained from a random, simulated cruise track in NATL60 in the central Labrador Sea in the respective months of MSM74 and MSM40 is also shown. The wavenumber k is given in cycles per kilometre (cpkm). The vertical black line represents the 10 km horizontal length scale threshold. The spectral slopes k^{-2} and k^{-3} are also shown

of magnitude lower than in MSM74. This is true for both depth regimes even though the differences particularly stand out in 350–400 m depth. The model predictions within the mixed layer as well as in the pycnocline match the ship data from MSM74 and MSM40 in the mesoscale range as expected. There is slight discrepancy in the MSM40 data in the range 80–100 km, in which the observation-based velocity spectra are roughly 10 times higher than the model. In the submesoscale regime the velocity spectra start to differ from each other below 10 km in the mixed layer in June (**Figure 23a**). During MSM40, the observations and model already seem to differ below 40 km (**Figure 23b**). The representation of submesoscale dynamics may rapidly decline with increasing depth as shown in **Figure 23c**, where observational and model velocity spectra diverge at spatial scales of 50 km. Better agreement is found for the velocity spectra in **Figure 23d**.

Some of the above findings were reported by a study from Shcherbina et al. (2013) that investigated the submesoscale turbulence field for the upper ocean in the Gulf stream region and compared the observations to a high-resolution numerical model with a grid spacing of 0.5 km embedded in a large-scale domain with 5–7 km resolution. Their model spectra agreed well for the mixed layer. In the upper pycnocline, however, model spectra were up to one order of magnitude lower at scales <20 km. They attribute the discrepancy to the lacking representation of high-frequency wind stress variations and tides in the upper ocean which in turn are the major drivers for internal gravity waves, i.e. submesocale turbulence. Small-scale turbulence through buoyancy loss is also considered an important energy source (Sasaki et al., 2014). A study focusing on the wavenumber spectra from ADCP measurements, altimeter data, and a high-resolution model in the Drake passage also implied internal gravity waves to be the main component of ageostrophic motion. It was found that internal gravity waves represent almost half of the kinetic energy near the surface (Rocha et al., 2016) at scales between 10 km and 40 km.

Atmospheric forcing applied to NATL60 has a temporal and spatial resolution of 3 hours and 0.7° which might not be sufficient for producing high-frequency air-sea interactions and resolving small-scale turbulence. The available NATL60 simulation did not account for internal tides. However, tides have recently been introduced to the eNATL60 simulation which is consequently not only submesoscale permitting but also tide-resolving. It is undisputed that the submesoscale flow regime peaks in winter when mixed layer depths and the associated mixed layer instabilites, transforming potential to kinetic energy, are at their maximum. (Mensa et al., 2013; Sasaki et al., 2014). The spectral slopes for the submesoscale regime were added to the surface/mixed layer power spectral density in **Figure 23a,b**. In June, the spectrum follows approximately a k^{-2} power law at scales in the order of $\mathcal{O}(10\,\text{km})$ with possible contributions from mixed layer instabilities and the mesoscale-driven frontogenesis mechanism. Mixed layer instabilities during spring time may not be as high than in winter months but

still seem to energise submesoscale turbulence. In summertime (August), the spectral slope transitions from k^{-2} to k^{-3}, most likely, due to a further reduction of mixed layer instabilities which decrease with shallowing mixed layer depths. The slight seasonal transition of submesoscale turbulence near the surface is also seen in the reduction of frontal strength in **Figure 6**. Since surface frontogenesis does not vary on seasonal scales Callies et al. (2015), one could expect that the large-scale velocity field, while enhancing the submesoscale flow, produces a slope similar to the k^{-2} spectra even in summertime. Instead, the summertime velocity field is rather characterised by a k^{-3} spectra slope which is commonly known as the Phillips regime. According to Phillips (1954), the k^{-3} spectra is related to quasi-geostrophic turbulence, i.e. baroclinic instability, which barely tranforms energy to submesoscales. As a consequence, surface-frontogenesis may not be present during summer months. Sasaki et al. (2014) noted that the governing dynamics that shape the velocity spectra may regionally vary. Considering the Labrador Sea, the mixed layer instabilities are concluded to dominate the enhancement of the submesoscale flow regime due to large seasonal variations of the mixed layer depth.

4 Summary and Conclusion

High-resolution ADCP measurements from two research expeditions in June 2018 and August 2014 provided valuable data of the eddy field and the associated horizontal velocity field in the central Labrador Sea. The eddy field was analysed in the framework of a cylindrical coordinate system by applying a nonlinear, damping least-squares Gauss-Newton optimisation algorithm that aims to provide an accurate eddy centre estimate. Several eddy defining parameters (radius, azimuthal velocity, relative vorticity, etc.) were derived from the optimisation and used for the characterisation of the eddy field in both observations and model. Further, the representation of the mesoscale and submesoscale flow field in the NATL60 was investigated taking the observations as a reference dataset.

A qualitative comparison between the ADCP measurements and altimetry-derived horizontal velocity field reveals significant discrepancies in the mesoscale eddy field reconstruction. The sea level anomaly data and the derived eddy field are assumed to underly aliasing of the unresolved scales of motion, i.e. smaller-scale vortices are interpreted as larger ones. It is concluded that the distortion of the eddy characteristics is the result of the spatially coarse coverage of satellite tracks and the across-track distance between satellite tracks which is larger than the local Rossby radius of deformation. Further, smaller-scale features might be removed through smoothing or coarse spatial and temporal correlation scales applied during the AVISO+/CMEMS mapping methodology.

Making use of the Gauss-Newton algorithm, a quantitative analysis of eddy characteristics was performed. A total of 14 eddies were detected in the ADCP measurements along the analysed ship tracks in MSM74 and MSM40. They are characterised by radii and azimuthal velocities in the range 7–35 km and 20–60 cm s^{-1} with a mean of 20 km and 35 cm s^{-1}, respectively. The modelled eddies are on average 25 % smaller in radius (15 km) and 20 % higher in azimuthal velocity (42 cm s^{-1}) and, hence, on average more nonlinear. The inner core velocity structure is found to be in solid body rotation for at least 1/2 to 2/3 of the radius before following a more Gaussian-like shape near the velocity maximum beyond. At the maximum radius, the azimuthal velocity may deviate from solid-body rotation by more than 30 % for the observations and 50 % for the model. Two different Gaussian functions were used and evaluated to describe the radial velocity structure. The outer ring velocity structure was in most cases best described by a $\exp(-r^2)$ dependency. On some occasions, though, the radial velocity was approached by a $\exp(-r^2/4)$ dependency characterised by less precipitously decreasing velocities in the outer ring.

A small number of CTD profiles indicated the survey of two different IR types that are characterised by a warm, salty core either surface trapped or overlaid by a cold, fresh

cap near the surface. The vertical structure of simulated IR in NATL60 were found to largely correspond with the observations.

Power spectral analysis applied to the horizontal velocitiy field in the observations and model suggest the sufficient representation of the mesoscale flow regime in NATL60 near the surface (mixed layer) and in deeper layers (pycnocline). In comparison to the ADCP observations, the submesoscale regime appears underrepresented. This is especially true for the pycnocline, where observation and model spectra diverge at spatial scales below 50 km. For both observations and model, the submesoscale power spectra are reduced from June to August supported by the transition of spectra slopes from k^{-2} to k^{-3}. The seasonal signal of the submesoscale flow field is suggested to be driven by mixed layer dpeth variations and the associated arising mixed layer instabilites.

Overall, the Gauss-Newton method applied to the observation based velocity data provides an alternative view to the sea level anomaly derived horizontal surface velocity field. The uncertainties involved in the optimisation were intensively discussed. Even though, the derived eddy characteristics depend on the location of the ship track with respect to the real eddy centre and some other factors, the computed eddy properties such as radius and azimuthal velocities are not expected to deviate by more than 10 % in most cases. Further improvements could be involved in the Gauss-Newton algorithm in future studies. Apart from the eddy centre optimisation, the eddy translation speed could be optimised as well to isolate the real rotational part of the eddy. Other adaptions include the implementation of the Levenberg-Marquardt method which is in theory more robust since it is less dependent on the appropriate choice of starting values.

The objective of this study was to characterise the eddy field in the central Labrador Sea and to investigate its representation in the submesoscale permitting NATL60 model. In respect of the Labrador Sea, the correct characterisation of the eddy field is of vital importance, since erroneous eddy properties would possibly have direct consequences in studies that simulate the role of mesoscale and submesoscale flow variability on physical processes such as the deep convection. The SWOT mission planned for launch in 2021 is expected to measure the surface ocean with high spatial resolution. It aims to resolve the submesoscal flow regime on global scales and then potentially serves as an additional tool for the validation of eddy field characteristics in observations and numerical models.

5 References

Ajayi, A., Le Sommer, J., Chassignet, E., Molines, J.-M., Xu, X., Albert, A., and Cosme, E. (2019). Spatial and temporal variability of north atlantic eddy field at scale less than 100km. *Journal of Geophysical Research: Oceans*, submitted for review.

Amores, A., Jordà, G., Arsouze, T., and Le Sommer, J. (2018). Up to what extent can we characterize ocean eddies using present-day gridded altimetric products? *Journal of Geophysical Research: Oceans*, 123(10), 7220–7236.

Beckers, M. and Van Heijst, G. (1998). The observation of a triangular vortex in a rotating fluid. *Fluid dynamics research*, 22(5), 265.

Boccaletti, G., Ferrari, R., and Fox-Kemper, B. (2007). Mixed layer instabilities and restratification. *Journal of Physical Oceanography*, 37(9), 2228–2250.

Brandt, P., Schott, F. A., Funk, A., and Martins, C. S. (2004). Seasonal to interannual variability of the eddy field in the labrador sea from satellite altimetry. *Journal of Geophysical Research: Oceans*, 109(C2).

Callies, J., Ferrari, R., Klymak, J. M., and Gula, J. (2015). Seasonality in submesoscale turbulence. *Nature communications*, 6, 6862.

Capet, X., McWilliams, J. C., Molemaker, M. J., and Shchepetkin, A. (2008). Mesoscale to submesoscale transition in the california current system. part i: Flow structure, eddy flux, and observational tests. *Journal of physical oceanography*, 38(1), 29–43.

Carnevale, G. and Kloosterziel, R. (1994). Emergence and evolution of triangular vortices. *Journal of fluid mechanics*, 259, 305–331.

Castelão, G. and Johns, W. E. (2011). Sea surface structure of north brazil current rings derived from shipboard and moored acoustic doppler current profiler observations. *Journal of Geophysical Research: Oceans*, 116(C1).

Castelão, G. P., Irber Jr, L. C., and Boas, A. B. V. (2013). An objective reference system for studying rings in the ocean. *Computers & geosciences*, 61, 43–49.

Chanut, J., Barnier, B., Large, W., Debreu, L., Penduff, T., Molines, J. M., and Mathiot, P. (2008). Mesoscale eddies in the labrador sea and their contribution to convection and restratification. *Journal of Physical Oceanography*, 38(8), 1617–1643.

Charney, J. G. (1971). Geostrophic turbulence. *Journal of the Atmospheric Sciences*, 28(6), 1087–1095.

Chelton, D. B., DeSzoeke, R. A., Schlax, M. G., El Naggar, K., and Siwertz, N. (1998). Geographical variability of the first baroclinic rossby radius of deformation. *Journal of Physical Oceanography*, 28(3), 433–460.

Chelton, D. B. and Schlax, M. G. (1996). Global observations of oceanic rossby waves. *Science*, 272(5259), 234–238.

Chelton, D. B., Schlax, M. G., and Samelson, R. M. (2011). Global observations of nonlinear mesoscale eddies. *Progress in Oceanography*, 91(2), 167–216.

Chelton, D. B., Schlax, M. G., Samelson, R. M., and de Szoeke, R. A. (2007). Global observations of large oceanic eddies. *Geophysical Research Letters*, 34(15).

Chigier, N. A. (1979). Pollution formation and destruction in flames—introduction. In *Energy and Combustion Science* (pp. 3–15). Elsevier.

Clarke, R. A. and Gascard, J.-C. (1983). The formation of labrador sea water. part i: Large-scale processes. *Journal of Physical Oceanography*, 13(10), 1764–1778.

de Jong, M. F., Bower, A. S., and Furey, H. H. (2014). Two years of observations of warm-core anticyclones in the labrador sea and their seasonal cycle in heat and salt stratification. *Journal of Physical Oceanography*, 44(2), 427–444.

Ducet, N., Le Traon, P.-Y., and Reverdin, G. (2000). Global high-resolution mapping of ocean circulation from topex/poseidon and ers-1 and-2. *Journal of Geophysical Research: Oceans*, 105(C8), 19477–19498.

Early, J. J., Samelson, R., and Chelton, D. B. (2011). The evolution and propagation of quasigeostrophic ocean eddies. *Journal of Physical Oceanography*, 41(8), 1535–1555.

Eden, C. and Böning, C. (2002). Sources of eddy kinetic energy in the labrador sea. *Journal of Physical Oceanography*, 32(12), 3346–3363.

Faghmous, J. H., Frenger, I., Yao, Y., Warmka, R., Lindell, A., and Kumar, V. (2015). A daily global mesoscale ocean eddy dataset from satellite altimetry. *Scientific data*, 2(1), 1–16.

Fu, L., Rodriguez, E., Alsdorf, D., and Morrow, R. (2012). The swot mission science document. *California, CA: JPL Publication.*

Fu, L.-L. and Ferrari, R. (2008). Observing oceanic submesoscale processes from space. *Eos, Transactions American Geophysical Union*, 89(48), 488–488.

Fu, L.-L. and Ubelmann, C. (2014). On the transition from profile altimeter to swath altimeter for observing global ocean surface topography. *Journal of Atmospheric and Oceanic Technology*, 31(2), 560–568.

Gascard, J.-C. and Clarke, R. A. (1983). The formation of labrador sea water. part ii. mesoscale and smaller-scale processes. *Journal of Physical Oceanography*, 13(10), 1779–1797.

Gelderloos, R., Katsman, C. A., and Drijfhout, S. S. (2011). Assessing the roles of three eddy types in restratifying the labrador sea after deep convection. *Journal of physical oceanography*, 41(11), 2102–2119.

Gill, A. E. (1982). *Atmosphere-Ocean dynamics (International Geophysics Series).* academic press.

Greatbatch, R. J. and Goulding, A. (1989). Seasonal variations in a linear barotropic model of the north atlantic driven by the hellerman and rosenstein wind stress field. *Journal of Physical Oceanography*, 19(5), 572–595.

Haine, T. W. and Marshall, J. (1998). Gravitational, symmetric, and baroclinic instability of the ocean mixed layer. *Journal of physical oceanography*, 28(4), 634–658.

Hátún, H., Eriksen, C. C., and Rhines, P. B. (2007). Buoyant eddies entering the labrador sea observed with gliders and altimetry. *Journal of Physical Oceanography*, 37(12), 2838–2854.

Higgins, K., Ooi, A., and Chong, M. (2002). The structure of an unstable circular vortex in a background straining flow. *Journal of Fluid Mechanics*, 462, 31–42.

Isern-Fontanet, J., García-Ladona, E., and Font, J. (2003). Identification of marine eddies from altimetric maps. *Journal of Atmospheric and Oceanic Technology*, 20(5), 772–778.

Jones, H. and Marshall, J. (1993). Convection with rotation in a neutral ocean: A study of open-ocean deep convection. *Journal of Physical Oceanography*, 23(6), 1009–1039.

Jones, H. and Marshall, J. (1997). Restratification after deep convection. *Journal of Physical Oceanography*, 27(10), 2276–2287.

Kanak, K. M. (2005). Numerical simulation of dust devil-scale vortices. *Quarterly Journal of the Royal Meteorological Society: A journal of the atmospheric sciences, applied meteorology and physical oceanography*, 131(607), 1271–1292.

Katsman, C. A., Spall, M. A., and Pickart, R. S. (2004). Boundary current eddies and their role in the restratification of the labrador sea. *Journal of Physical Oceanography*, 34(9), 1967–1983.

Klein, P. and Lapeyre, G. (2009). The oceanic vertical pump induced by mesoscale and submesoscale turbulence. *Annual review of marine science*, 1, 351–375.

Klocker, A., Marshall, D. P., Keating, S. R., and Read, P. L. (2016). A regime diagram for ocean geostrophic turbulence. *Quarterly Journal of the Royal Meteorological Society*, 142(699), 2411–2417.

Kloosterziel, R. and Van Heijst, G. (1991). An experimental study of unstable barotropic vortices in a rotating fluid. *Journal of fluid mechanics*, 223, 1–24.

Lapeyre, G. and Klein, P. (2006a). Dynamics of the upper oceanic layers in terms of surface quasi-geostrophy theory. *Journal of physical oceanography*, 36(2), 165–176.

Lapeyre, G. and Klein, P. (2006b). Impact of the small-scale elongated filaments on the oceanic vertical pump. *Journal of Marine Research*, 64(6), 835–851.

Lapeyre, G., Klein, P., and Hua, B. L. (2006). Oceanic restratification forced by surface frontogenesis. *Journal of Physical Oceanography*, 36(8), 1577–1590.

Lazier, J. R. (1973). The renewal of labrador sea water. *Deep Sea Research and Oceanographic Abstracts*, 20(4), 341–353.

Lazier, J. R. (1980). Oceanographic conditions at ocean weather ship bravo, 1964–1974. *Atmosphere-ocean*, 18(3), 227–238.

Le Traon, P., Faugère, Y., Hernandez, F., Dorandeu, J., Mertz, F., and Ablain, M. (2003). Can we merge geosat follow-on with topex/poseidon and ers-2 for an improved description of the ocean circulation? *Journal of Atmospheric and Oceanic Technology*, 20(6), 889–895.

Legras, B. and Dritschel, D. (1993). Vortex stripping and the generation of high vorticity gradients in two-dimensional flows. In *Advances in Turbulence IV* (pp. 445–455). Springer.

Lévy, M., Ferrari, R., Franks, P. J., Martin, A. P., and Rivière, P. (2012). Bringing physics to life at the submesoscale. *Geophysical Research Letters*, 39(14).

Lilly, J. M., Rhines, P. B., Schott, F., Lavender, K., Lazier, J., Send, U., and D'Asaro, E. (2003). Observations of the labrador sea eddy field. *Progress in Oceanography*, 59(1), 75–176.

Lilly, J. M., Rhines, P. B., Visbeck, M., Davis, R., Lazier, J. R., Schott, F., and Farmer, D. (1999). Observing deep convection in the labrador sea during winter 1994/95. *Journal of Physical Oceanography*, 29(8), 2065–2098.

Liu, X. and Levine, N. M. (2016). Enhancement of phytoplankton chlorophyll by submesoscale frontal dynamics in the north pacific subtropical gyre. *Geophysical research letters*, 43(4), 1651–1659.

Marshall, J. and Schott, F. (1999). Open-ocean convection: Observations, theory, and models. *Reviews of Geophysics*, 37(1), 1–64.

McWilliams, J. C. (1985). Submesoscale, coherent vortices in the ocean. *Reviews of Geophysics*, 23(2), 165–182.

McWilliams, J. C. (2016). Submesoscale currents in the ocean. *Proceedings of the Royal Society A: Mathematical, Physical and Engineering Sciences*, 472(2189), 20160117.

Mensa, J. A., Garraffo, Z., Griffa, A., Özgökmen, T. M., Haza, A., and Veneziani, M. (2013). Seasonality of the submesoscale dynamics in the gulf stream region. *Ocean Dynamics*, 63(8), 923–941.

Meuel, T., Xiong, Y. L., Fischer, P., Bruneau, C.-H., Bessafi, M., and Kellay, H. (2013). Intensity of vortices: from soap bubbles to hurricanes. *Scientific reports*, 3, 3455.

Morrow, R., Fu, L.-L., Ardhuin, F., Benkiran, M., Chapron, B., Cosme, E., d'Ovidio, F., Farrar, J. T., Gille, S. T., Lapeyre, G., et al. (2019). Global observations of fine-scale ocean surface topography with the surface water and ocean topography (swot) mission. *Frontiers in Marine Science*, 6, 232.

Nurser, A. and Bacon, S. (2014). The rossby radius in the arctic ocean. *Ocean Science*, 10(6), 967–975.

Okubo, A. (1970). Horizontal dispersion of floatable particles in the vicinity of velocity singularities such as convergences. In *Deep sea research and oceanographic abstracts*, volume 17 (pp. 445–454).: Elsevier.

Olson, D. B. (1980). The physical oceanography of two rings observed by the cyclonic ring experiment. part ii: Dynamics. *Journal of Physical Oceanography*, 10(4), 514–528.

Phillips, N. A. (1954). Energy transformations and meridional circulations associated with simple baroclinic waves in a two-level, quasi-geostrophic model. *Tellus*, 6(3), 274–286.

Pickart, R. S., Torres, D. J., and Clarke, R. A. (2002). Hydrography of the labrador sea during active convection. *Journal of Physical Oceanography*, 32(2), 428–457.

Pujol, M.-I., Faugère, Y., Taburet, G., Dupuy, S., Pelloquin, C., Ablain, M., and Picot, N. (2016). Duacs dt2014: the new multi-mission altimeter data set reprocessed over 20 years. *Ocean Sci*, 12(5), 1067–1090.

Rieck, J. K., Böning, C. W., and Getzlaff, K. (2019). The nature of eddy kinetic energy in the labrador sea: Different types of mesoscale eddies, their temporal variability, and impact on deep convection. *Journal of Physical Oceanography*, 49(8), 2075–2094.

Robinson, A. R. (1983). Overview and summary of eddy science. In *Eddies in marine science* (pp. 3–15). Springer.

Rocha, C. B., Chereskin, T. K., Gille, S. T., and Menemenlis, D. (2016). Mesoscale to submesoscale wavenumber spectra in drake passage. *Journal of Physical Oceanography*, 46(2), 601–620.

Sasaki, H., Klein, P., Qiu, B., and Sasai, Y. (2014). Impact of oceanic-scale interactions on the seasonal modulation of ocean dynamics by the atmosphere. *Nature communications*, 5(1), 1–8.

Scott, R. B. and Arbic, B. K. (2007). Spectral energy fluxes in geostrophic turbulence: Implications for ocean energetics. *Journal of physical oceanography*, 37(3), 673–688.

Shcherbina, A. Y., D'Asaro, E. A., Lee, C. M., Klymak, J. M., Molemaker, M. J., and McWilliams, J. C. (2013). Statistics of vertical vorticity, divergence, and strain in a developed submesoscale turbulence field. *Geophysical Research Letters*, 40(17), 4706–4711.

Stammer, D. (1997). Global characteristics of ocean variability estimated from regional topex/poseidon altimeter measurements. *Journal of Physical Oceanography*, 27(8), 1743–1769.

Thomas, L. N., Tandon, A., and Mahadevan, A. (2008). Submesoscale processes and dynamics. *Ocean modeling in an Eddying Regime*, 177, 17–38.

Van Heijst, G. and Kloosterziel, R. (1989). Tripolar vortices in a rotating fluid. *Nature*, 338(6216), 569–571.

Van Heijst, G., Kloosterziel, R., and Williams, C. (1991). Laboratory experiments on the tripolar vortex in a rotating fluid. *Journal of fluid mechanics*, 225, 301–331.

Visbeck, M. (2002). Deep velocity profiling using lowered acoustic doppler current profilers: Bottom track and inverse solutions. *Journal of atmospheric and oceanic technology*, 19(5), 794–807.

Wang, Z., Li, Q., Sun, L., Li, S., Yang, Y., and Liu, S. (2015). The most typical shape of oceanic mesoscale eddies from global satellite sea level observations. *Frontiers of Earth Science*, 9(2), 202–208.

Weiss, J. (1991). The dynamics of enstrophy transfer in two-dimensional hydrodynamics. *Physica D: Nonlinear Phenomena*, 48(2-3), 273–294.

Wunsch, C. and Ferrari, R. (2004). Vertical mixing, energy, and the general circulation of the oceans. *Annu. Rev. Fluid Mech.*, 36, 281–314.

Wyrtki, K., Magaard, L., and Hager, J. (1976). Eddy energy in the oceans. *Journal of Geophysical Research*, 81(15), 2641–2646.

Yang, Z., Wang, G., and Chen, C. (2019). Horizontal velocity structure of mesoscale eddies in the south china sea. *Deep Sea Research Part I: Oceanographic Research Papers*, 149, 103055.

Yule, A. (1978). Large-scale structure in the mixing layer of a round jet. *Journal of Fluid Mechanics*, 89(3), 413–432.

Zhang, Z. and Qiu, B. (2018). Evolution of submesoscale ageostrophic motions through the life cycle of oceanic mesoscale eddies. *Geophysical Research Letters*, 45(21), 11–847.

Zhang, Z., Zhang, Y., Wang, W., and Huang, R. X. (2013). Universal structure of mesoscale eddies in the ocean. *Geophysical Research Letters*, 40(14), 3677–3681.

Appendices

A Mesoscale and submesoscale velocity components

Figure A1: Mesoscale component of the zonal (upper panel) and meridional (lower panel) current velocity for the 38 kHz instrument during MSM74.

Figure A2: Submesoscale component of the zonal (upper panel) and meridional (lower panel) current velocity for the 38 kHz instrument during MSM74.
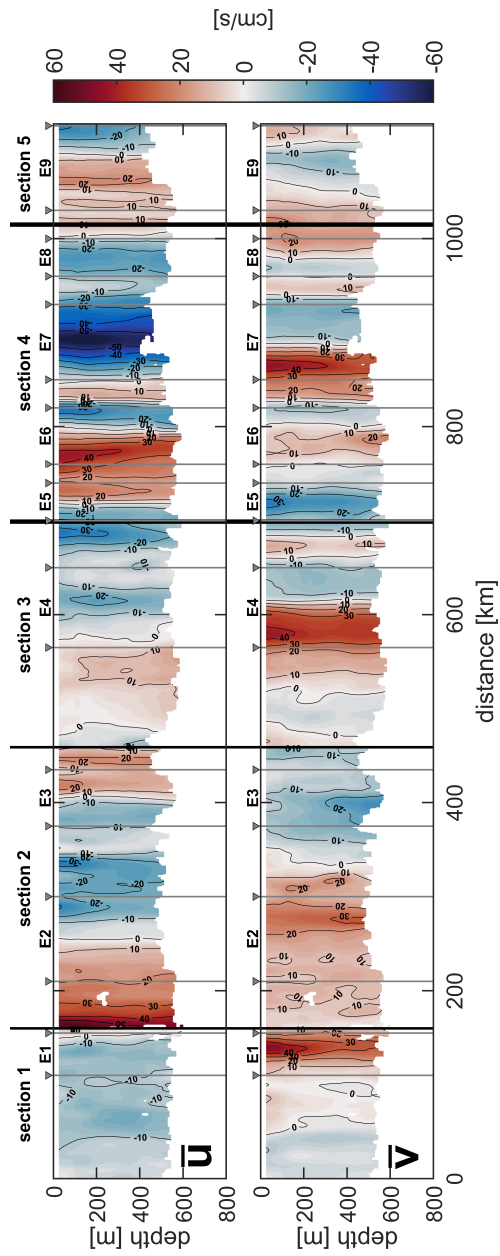
Figure A3: Mesoscale component of the zonal (upper panel) and meridional (lower panel) current velocity for the 75 kHz instrument during MSM74.
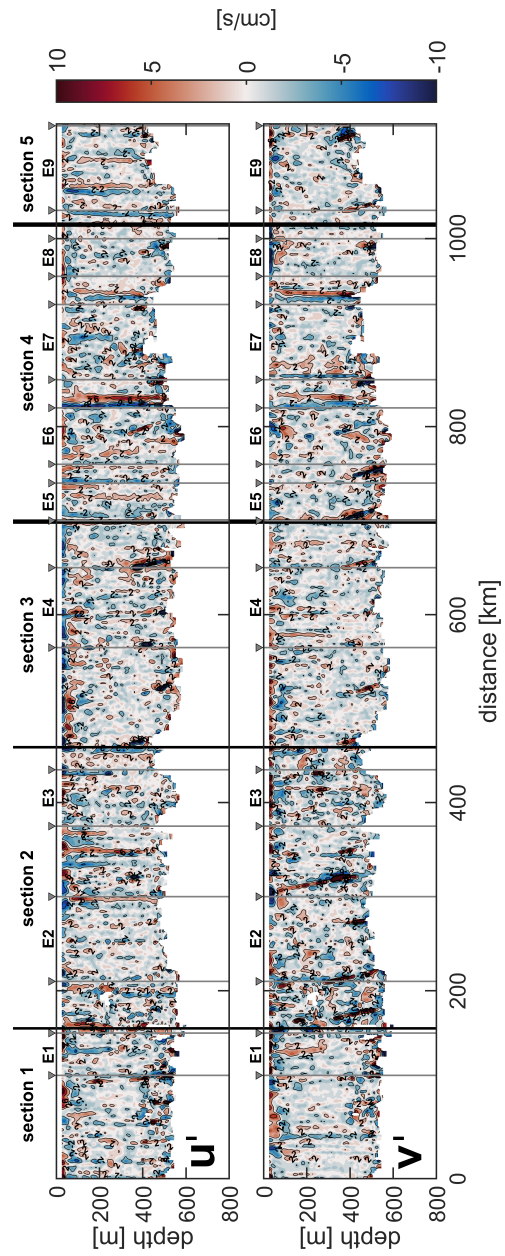
Figure A4: Submesoscale component of the zonal (upper panel) and meridional (lower panel) current velocity for the 75 kHz instrument during MSM74.
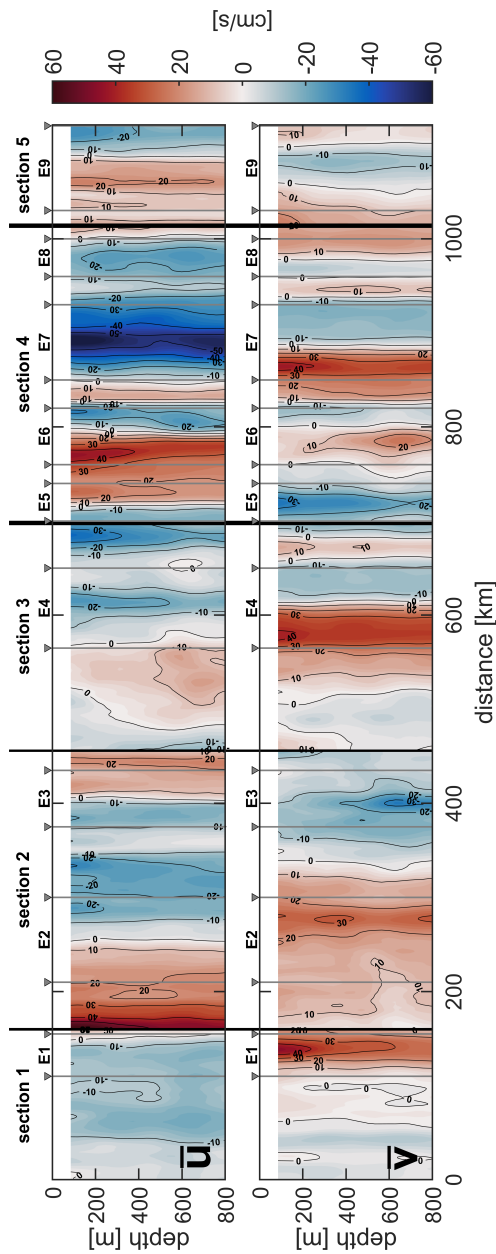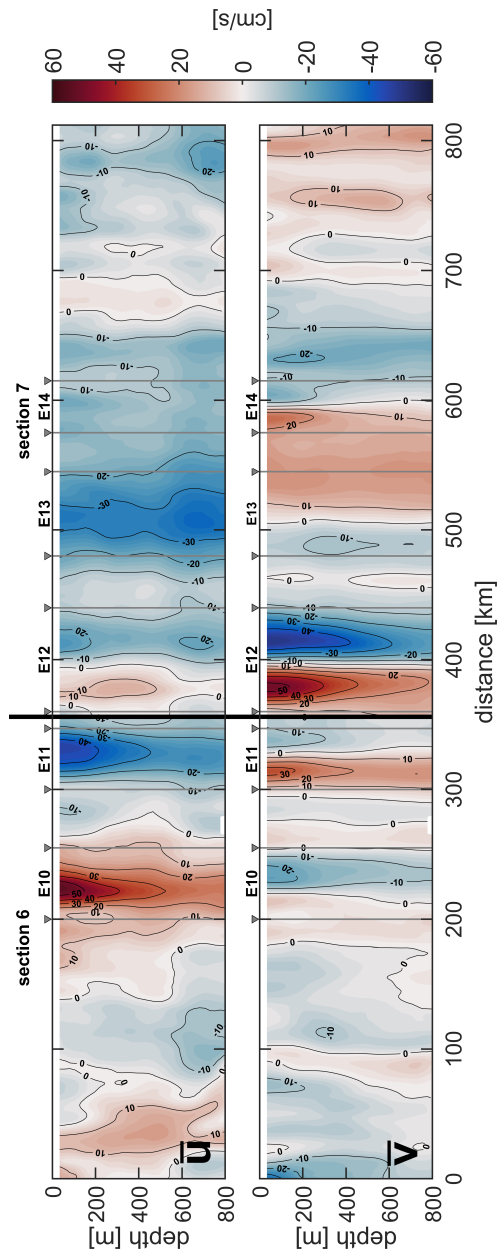
Figure A5: Mesoscale component of the zonal (upper panel) and meridional (lower panel) current velocity for the 38 kHz instrument during MSM40.
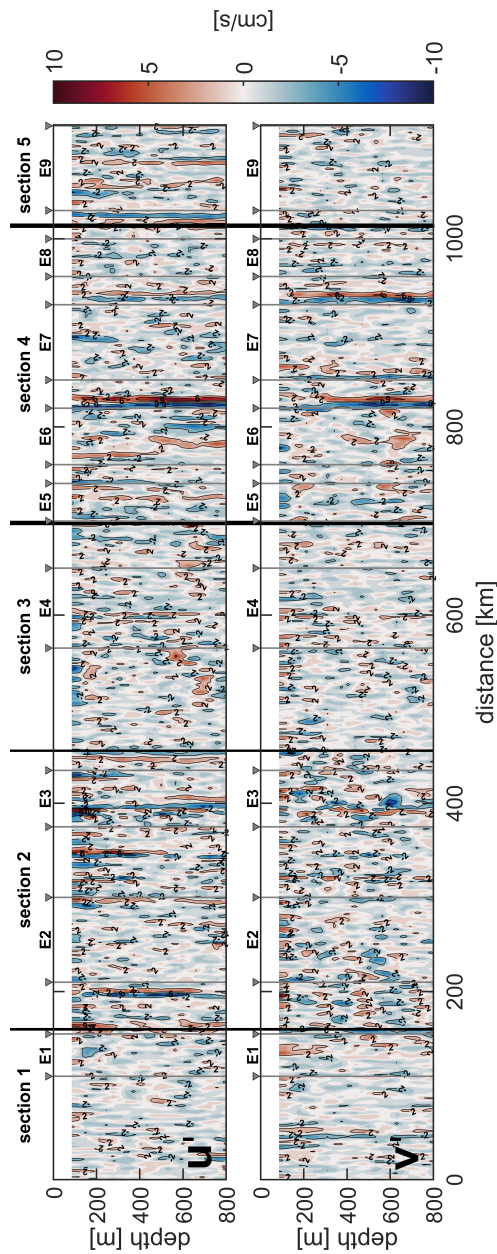

Figure A6: Submesoscale component of the zonal (upper panel) and meridional (lower panel) current velocity for the 38 kHz instrument during MSM40.

Figure A7: Mesoscale component of the zonal (upper panel) and meridional (lower panel) current velocity for the 150 kHz instrument during MSM40.

Figure A8: Submesoscale component of the zonal (upper panel) and meridional (lower panel) current velocity for the 150 kHz instrument during MSM40.
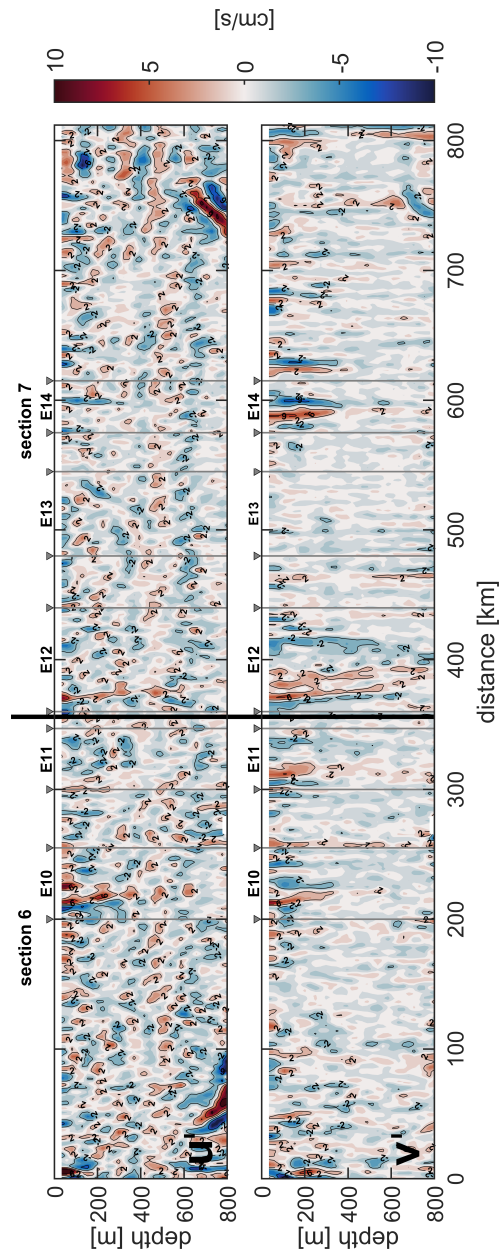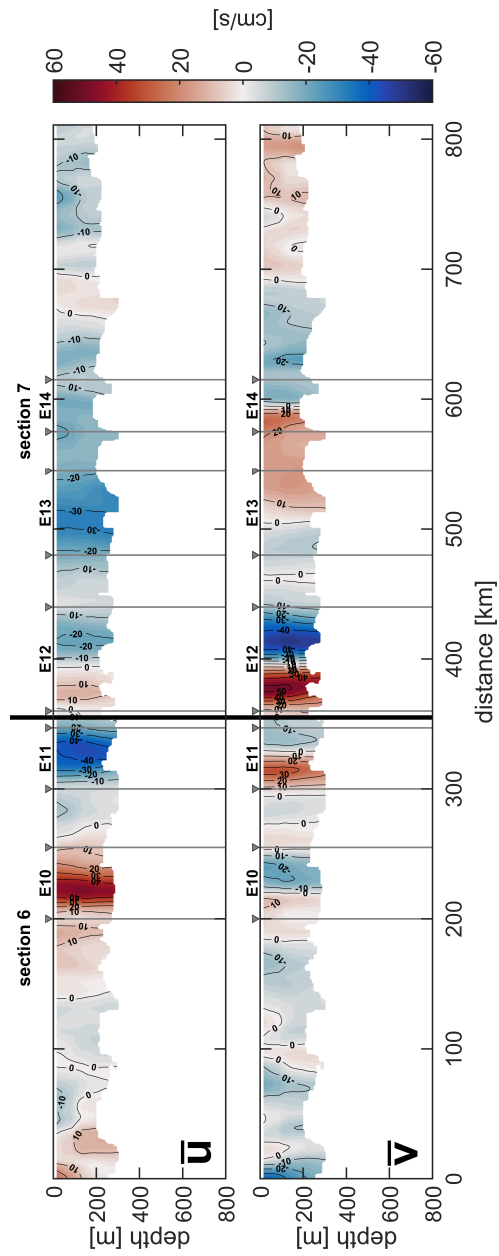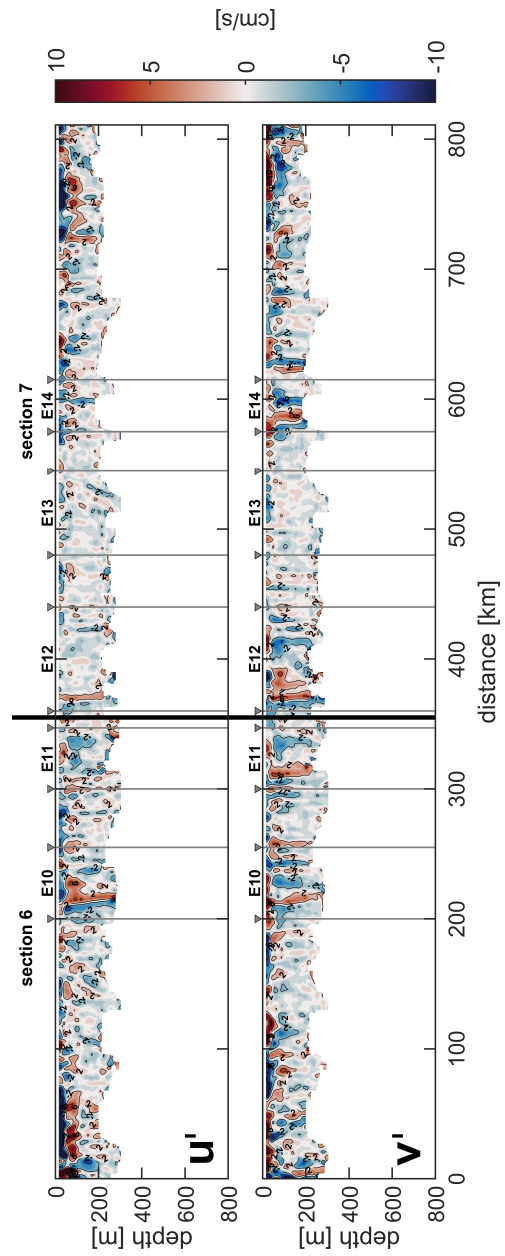
B Gauss-Newton derived model eddy characteristics

Table B1: Gauss-Newton derived eddy characteristics: maximum radius R_{max}, maximum azimuthal velocity V_{max}, outer ring decay scale λ, maximum sea surface height η_0, inner core relative vorticity ζ_{in}, Rossby number Ro of the gradient flow, theoretical maximum azimuthal velocity V_{sb} for solid-body rotation, and eddy type if applicable. Positive values for azimuthal velocity, relative vorticity, and Rossby number denote anti-clockwise rotation (cyclone), negative values denote clockwise clockwise rotation (anticyclone). Values are to be understood as the mean of both radial sections with given standard deviation for each eddy. The abbreviations IR1 and IR2 denote the two Irminger ring eddy types. The mean was calculated using the variable's magnitude.

Eddy Nr #	R_{max} [km]	V_{max} [cm s^{-1}]	λ [km]	η_0 [cm]	ζ_{in} 10^{-5} [s^{-1}]	Ro	V_{sb} [cm s^{-1}]	type
NATL60 June 15th								
E1	21.6 ± 2.6	$-68.5 \pm 6.$	14.5 ± 2.0	24.1	-6.3 ± 0.2	-0.26	-100.0 ± 9.8	IR1
E2	20.5 ± 1.0	-77.1 ± 2.9	27.0 ± 5.8	40.0	-7.5 ± 0.1	-0.30	-97.4 ± 4.6	IR2
E3	17.8 ± 0.2	-88.5 ± 0.6	12.7 ± 3.4	28.7	-10.0 ± 0.0	-0.40	-105.5 ± 9.0	
E4	18.6 ± 1.0	-70.5 ± 1.3	13.6 ± 1.3	23.0	-7.6 ± 0.6	-0.3	-90.4 ± 1.2	IR2
E5	15.0 ± 1.3	-51.7 ± 3.0	18.1 ± 6.2	18.1	-6.9 ± 0.2	-0.28	-70.9 ± 5.0	IR1
E6	13.2 ± 2.1	19.2 ± 1.6	62.7 ± 65.7	-16.8	2.9 ± 0.2	0.12	36.7 ± 8.5	-
E7	11.8 ± 4.0	-42.0 ± 12.9	10.1 ± 3.2	9.2	-7.2 ± 0.2	-0.29	-54.5 ± 15.6	IR1
E8	21.5 ± 1.0	-39.8 ± 0.5	29.0 ± 2.4	20.3	-3.7 ± 0.1	-0.15	-78.1 ± 5.5	IR2
E9	8.8 ± 5.5	24.3 ± 20.8	20.5 ± 19.1	-7.8	5.0 ± 1.6	0.23	34.5 ± 31.5	-
E10	11.6 ± 2.4	-40.4 ± 5.4	32.4 ± 22.7	20.3	-7.0 ± 0.5	-0.28	-48.6 ± 8.5	-
E11	12.3 ± 2.9	30.9 ± 8.7	38.1 ± 20.5	-17.8	5.0 ± 0.2	0.20	49.2 ± 13.0	-
E12	5.8 ± 2.1	-16.3 ± 5.7	6.3 ± 0.0	2.0	-5.6 ± 0.0	-0.23	-22.3 ± 11.6	IR1
E13	19.3 ± 0.4	-43.4 ± 7.1	9.6 ± 1.3	11.2	-4.5 ± 0.7	-0.19	-49.3 ± 8.8	IR1
E14	11.1 ± 2.6	-18.4 ± 2.1	18.2 ± 13.7	5.8	-3.3 ± 0.4	-0.13	-24.4 ± 3.2	IR1
E15	9.2 ± 0.4	-15.6 ± 0.2	11.5 ± 1.9	3.3	-3.4 ± 0.2	-0.14	-19.4 ± 0.9	-
NATL60 August 15th								
E16	25.7 ± 1.7	-62.2 ± 1.7	22.2 ± 0.7	29.5	-4.9 ± 0.2	-0.2	-78.3 ± 5.5	IR2
E17	20.5 ± 0.3	-66.9 ± 2.4	19.4 ± 1.1	27.0	-6.5 ± 0.3	-0.27	-85.5 ± 8.2	IR1
E18	18.3 ± 0.8	-57.1 ± 2.1	17.8 ± 6.1	21.4	-6.2 ± 0.5	-0.25	-78.7 ± 2.8	IR1
E19	17.0 ± 0.4	-61.2 ± 0.0	14.6 ± 0.1	19.6	-7.2 ± 0.4	-0.29	-79.4 ± 1.6	IR1
E20	12.6 ± 2.7	-38.9 ± 10.5	11.3 ± 2.7	9.3	-6.2 ± 0.3	-0.25	-55.7 ± 16.2	IR1
E21	19.7 ± 2.0	-63.0 ± 0.8	15.7 ± 5.3	22.8	-6.4 ± 0.7	-0.25	-79.4 ± 0.2	IR2
E22	17.1 ± 0.8	-64.4 ± 5.6	13.7 ± 0.9	20.5	-7.5 ± 1.0	-0.30	-77.3 ± 9.1	IR2
E23	14.1 ± 0.1	-50.0 ± 0.4	20.8 ± 5.5	18.9	-7.1 ± 0.1	-0.29	-73.6 ± 0.5	IR1
E24	14.6 ± 0.9	-38.7 ± 3.6	16.5 ± 4.6	12.5	-5.3 ± 0.2	-0.21	-52.9 ± 10.8	IR1
E25	7.6 ± 2.3	-29.7 ± 7.8	9.8 ± 2.2	5.6	-7.9 ± 0.3	-0.31	-41.2 ± 12.6	IR2
E26	12.0 ± 2.8	17.3 ± 2.7	14.8 ± 3.7	-4.6	2.9 ± 0.2	0.12	20.6 ± 3.4	-
E27	8.7 ± 0.2	20.8 ± 1.9	25.7 ± 2.6	-7.9	4.8 ± 0.3	0.20	32.9 ± 4.7	-
E28	25.1 ± 2.3	-31.4 ± 2.7	41.1 ± 18.4	21.3	-2.5 ± 0.0	-0.1	-53.1 ± 10.2	IR2
E29	16.7 ± 3.0	-39.7 ± 6.8	14.8 ± 2.1	12.2	-4.8 ± 0.0	-0.20	-46.2 ± 9.8	IR2
E30	21.8 ± 0.4	-37.2 ± 2.6	13.3 ± 3.1	11.7	-3.4 ± 0.3	-0.14	-63.1 ± 3.7	-
E31	7.9 ± 0.8	17.0 ± 1.8	24.9 ± 11.2	-6.3	4.3 ± 0.0	0.18	27.4 ± 4.1	-
E32	7.2 ± 2.7	-18.7 ± 5.4	11.2 ± 9.1	3.6	-5.3 ± 0.5	-0.21	-24.4 ± 7.1	IR2
E33	9.1 ± 5.6	16.7 ± 15.2	49.8 ± 39.2	-11.6	3.3 ± 1.3	0.15	21.6 ± 20.9	-
Mean	15.0 ± 5.5	41.7 ± 20.7	20.7 ± 12.3	15.6 ± 9.0	5.5 ± 1.8	0.22 ± 0.07	56.7 ± 25.8	-

6   Acknowledgements

First of all, I would like to thank Johannes Karstensen for the great supervision, his passion and commitment for the topic as well as the support and nice discussions throughout my Master thesis.
Second, I thank Julien Le Sommer and Aurélie Albert who kindly provided me with the NATL60 model data and who always were available for any questions and demands. Additionally, I highly appreciate Arne Biastoch's role as the second assessor and for the extra input he has given me for the thesis. Finally, many thanks are dedicated to the people that supported me during the last couple of months and to those that have committed themselves to proofreading.

7 Erklärung

Hiermit erkläre ich, Arne Bendinger, dass ich die vorliegende Arbeit selbständig und ohne fremde Hilfe angefertigt und keine anderen als die angegebenen Quellen und Hilfsmittel verwendet habe.
Die eingereichte schriftliche Fassung der Arbeit stimmt mit der auf dem elektronischen Speichermedium überein (Bendinger_1012126.pdf). Weiterhin versichere ich, dass diese Arbeit noch nicht als Abschlussarbeit an anderer Stelle vorgelegen hat.

———————————————————   ———————————————————
Kiel, den 13. März 2020   Arne Bendinger